Nano Today 40 (2021) 101286

Contents lists available at ScienceDirect

Nano Today

journal homepage: www.elsevier.com/locate/nanotoday

Review

Multifunctional quantum dot materials for perovskite solar cells: Charge transport, efficiency and stability

Meidan Ye[a,b,*], Gill M. Biesold[b], Meng Zhang[b], Weiguo Wang[a], Tian Bai[a], Zhiqun Lin[b,**]

[a] Research Institute for Biomimetics and Soft Matter, Fujian Provincial Key Laboratory for Soft Functional Materials Research, Department of Physics, College of Physical Science and Technology, Xiamen University, Xiamen 361005, China
[b] School of Materials Science and Engineering, Georgia Institute of Technology, Atlanta, GA 30332, USA

ARTICLE INFO

Article history:
Received 22 June 2021
Received in revised form 24 August 2021
Accepted 29 August 2021
Available online 13 September 2021

Keywords:
Quantum dots
Perovskite solar cells
Light harvesting
Charge transport
Stability

ABSTRACT

Perovskite solar cells (PSCs) have recently emerged as an ideal candidate for next-generation photovoltaic applications. While promising, many challenges stand between PSCs and widespread application, including moisture, thermal and UV stability, photocurrent hysteresis behavior, flexibility, and large-scale productions. Meanwhile, quantum dot materials have attracted intensive research interest within past decades owing to their fantastic optical, electrical and optoelectrical properties, such as size-dependent energy band gaps derived from quantum confinement, high photon absorption coefficient, and multiple exciton generation. Their facile solution synthesis, tunable energy-level structures, and variable surface chemistry via ligand engineering make quantum dots (QDs) attractive for a variety of significant functions in PSCs. In this review, we summarize how a variety of QD materials (e.g., carbon, graphene, metal oxides, metal sulfides, metal selenides, metal tellurides, black phosphorus, organic/inorganic halide perovskites, etc.) can be applied in PSCs. We detail that QDs can play diverse roles in PSCs, including light harvesters, electron and hole transporters, additives into perovskite and charge transport layers, and interfacial modifiers. Particularly, the introduction of QD materials into PSCs enables the growth of high-quality perovskite films with larger grain sizes and reduced trap-state density due to the strong chemical interaction between QDs and perovskites, yielding high efficiency of stable PSCs. The size-dependent energy band gaps of QDs enable enhanced energy-level alignment for efficient charge transfer in PSCs. Moreover, the incorporation of QDs capped with highly hydrophobic ligands can enhance the long-term moisture stability of PSCs. Additionally, the photoluminescence property of QDs can be used to convert UV-radiation into harvestable visible light to improve the photocurrent and photostability of PSCs. The different characteristics and functions of QDs in PSCs are then discussed. Finally, insight into the further development of QD materials in PSCs is outlined.

Contents

* Corresponding author at: Research Institute for Biomimetics and Soft Matter, Fujian Provincial Key Laboratory for Soft Functional Materials Research, Department of Physics, College of Physical Science and Technology, Xiamen University, Xiamen 361005, China.
** Corresponding author.
E-mail addresses: mdye@xmu.edu.cn (M. Ye), zhiqun.lin@mse.gatech.edu (Z. Lin).

https://doi.org/10.1016/j.nantod.2021.101286
1748-0132/

Introduction

Over the past decade, perovskite solar cells (PSCs) have attracted significant research interest due to their fantastic optoelectronic characteristics and low manufacturing cost. The core of PSCs is halide perovskite, which has the chemical formula ABX_3 (Fig. 1a, A: $CH_3NH_3^+$ (MA), $CH_2(NH_2)_2^+$ (FA), or Cs^+; B: Pb^{2+} or Sn^{2+}; X: Cl^-, Br^- or I^-). Many outstanding optical and electrical properties have been reported for halide perovskites, for example, wide absorption spectrum (e.g., E_g = 1.5–1.6 eV for $MAPbI_3$), high molar extinction coefficient (e.g., ~ 5.7 × 10^4 cm^{-1} at 600 nm for $MAPbI_3$), low exciton binding energy (e.g., ~ 30 meV in $MAPbI_3$), ambipolar carrier transport characteristics (e.g., carrier mobility: electrons > 7.5 cm^2 V^{-1} s^{-1} and hole > 12.5 cm^2 V^{-1} s^{-1} in $MAPbI_3$), long carrier diffusion length (e.g., ~ 1 μm for polycrystalline $MAPbI_3$ and > 175 μm for $MAPbI_3$ single crystals), and high defects tolerance [1–3]. The facile solution processability of perovskites is also crucial for the rapid development of PSCs. With careful optimization in all aspects (Fig. 1b) [4–12], the maximum certified power conversion efficiency (PCE) of PSCs has reached 25.2% (Fig. 1c) [13].

PSCs generally consist of perovskite layers sandwiched between electron transport layers (ETLs) and hole transport layers (HTLs). The three most commonly used device architectures for PSCs are schematically illustrated in Fig. 2a–c. They are: (a) mesoporous n-i-p, (b) planar n-i-p, and (c) planar p-i-n structures, with the n, i, and p relating to the ETL, perovskite, and HTL, respectively. In general, the mesoporous n-i-p structure is constructed with fluorine-doped tin oxide (FTO) glass/compact ETL (e.g., TiO_2, SnO_2, and ZnO)/mesoporous ETL (e.g., TiO_2 nanoparticles (NPs), and Al_2O_3 NPs)/perovskite/HTL (e.g., Spiro-OMeTAD (2,2′,7,7′-tetrakis-(N,N-di-4-methoxyphenylamino)-9,9′-spirobifluorene))/top electrode (e.g., Ag, Au, and Al; Fig. 2a and d). The planar n-i-p structure is assembled with FTO or indium tin oxide (ITO) glass/compact ETL (e.g., TiO_2, SnO_2, ZnO, and PCBM (phenyl-C61-butyric acid methyl ester))/perovskite/HTL (e.g., Spiro-OMeTAD, and PTAA (polytriarylamine))/top electrode (e.g., Ag, Au, and Al; Fig. 2b and d). And the planar p-i-n structure is composed of FTO or ITO glass/HTL (e.g., NiO, and PEDOT:PSS (poly(4-butylphenyldiphenylamine), poly(3,4-ethylenedioxythiophene) polystyrene sulfonate))/perovskite/compact ETL (e.g., PCBM, C_{60} (buckminsterfullerene), and BCP (bathocuproine))/top electrode (e.g., Ag, Al and Au; Fig. 2c and d) [14,15].

During the last decade, intensive effort has been devoted to optimizing many aspects of PSC devices [16–19]. As highlighted in Figs. 1b and 2, recent studies on PSCs mostly focus on the improvement of perovskite films and optimization of ETLs and HTLs via various methods [20–24]. The integration of additives into perovskite and charge transport layers [25,26] and interfacial engineering [27,28] have been shown to boost both cell efficiency and stability of PSCs. To understand the relative mechanisms associated with PSCs, theoretical simulation on some aspects of PSCs (e.g., perovskite crystallization, defect passivation and charge transport) has proven to be essential [29]. The toxicity of perovskite materials can be reduced by substituting Pb^{2+} with Sn^{2+}, with complete Sn substitution being preferred [30]. Flexible PSCs have been developed for applications in wearable electronic devices [31]. PSCs have shown promise for large scale synthesis, which is essential for device

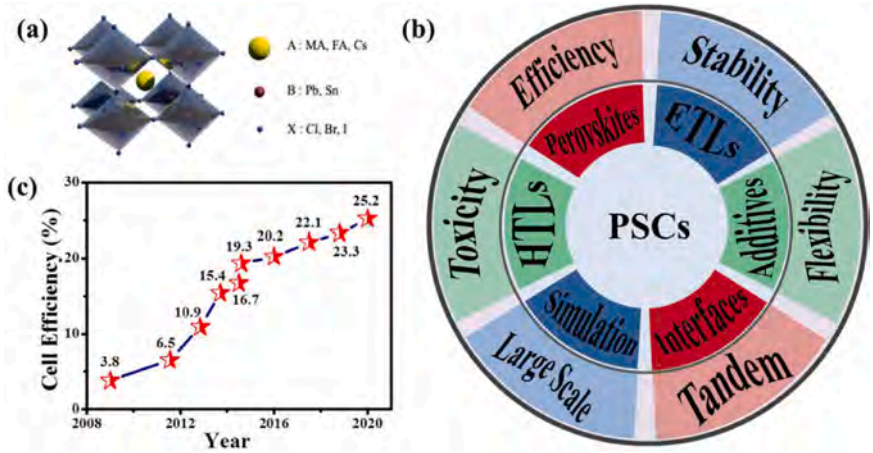

Fig. 1. (a) Crystal structure diagram of a typical perovskite with the chemical formula of ABX_3 (A: $CH_3NH_3^+$ (MA), $CH_2(NH_2)_2^+$ (FA), or Cs^+; B: Pb^{2+} or Sn^{2+}; X: Cl^-, Br^- or I^-). (b) Schematic diagram of some keywords for the research aspects on PSCs in recent years (ETLs: electron transport layers; HTLs: hole transport layers). (c) The progress of cell efficiency for perovskite solar cells (PSCs) [4–13].

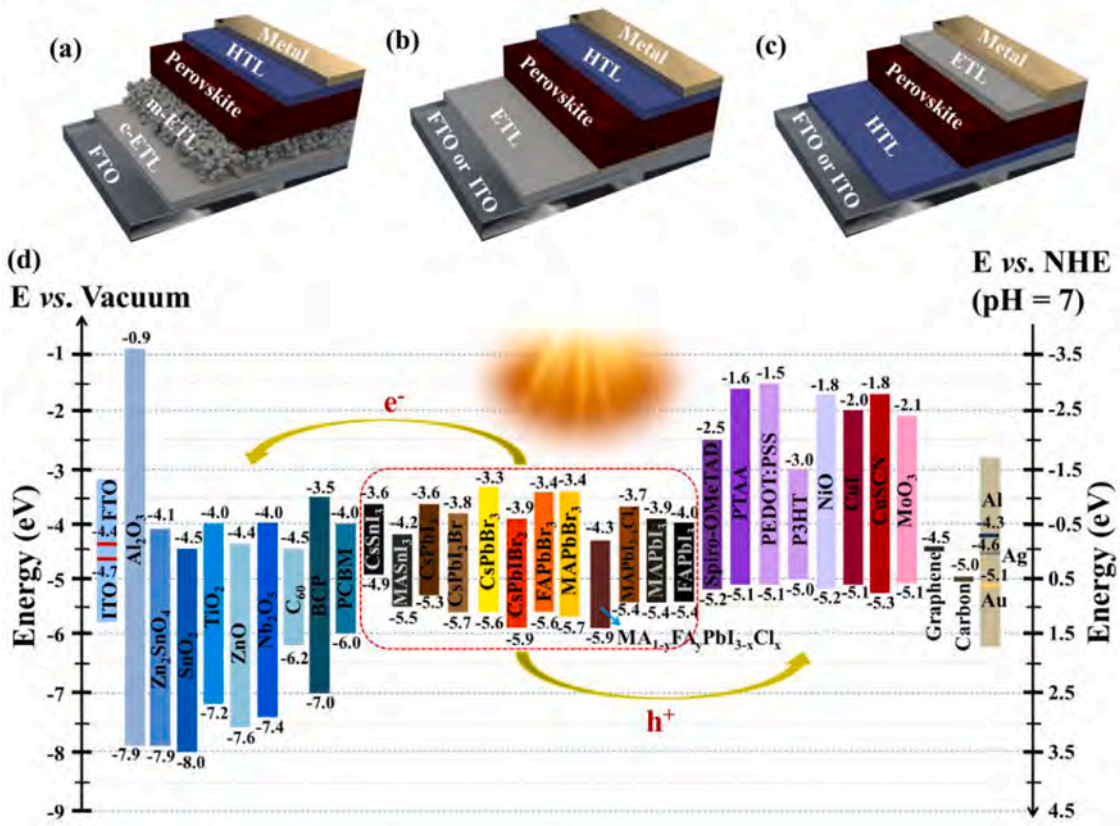

Fig. 2. Schematic diagrams of the typical device structures for PSCs: (a) mesoporous n-i-p, (b) planar n-i-p, and (c) planar p-i-n structures. FTO: fluorine-doped tin oxide; ITO: indium tin oxide; c-ETL: compact electron transport layer; m-ETL: mesoporous electron transport layer; HTL: hole transport layer. (d) The energy levels of some representative materials used in PSCs. PCBM: phenyl-C61-butyric acid methyl ester; Spiro-OMeTAD: 2,2′,7,7′-tetrakis-(N,N-di-4-methoxyphenylamino)-9,9′-spirobifluorene; PTAA: poly-triarylamine; PEDOT:PSS: poly(4-butylphenyldiphenylamine), poly(3,4-ethylenedioxythiophene) polystyrene sulfonate; P3HT: poly(3-hexylthiophene); BCP: bathocuproine; C_{60}: buckminsterfullerene.

commercialization [32]. The suitable/tunable energy band gaps and facile deposition of perovskites have also led to their application in high-performance tandem solar cells [33].

Colloidal semiconductor nanocrystals or quantum dots (QDs) are another type of semiconductor material with great promise in photovoltaic applications. QDs are commonly synthesized via facile chemical solution routes [34–36] and have been widely used in photocatalysis [37–39], photovoltaic [40–44], and other optoelectronic devices (e.g., photodetectors, light emitting diode (LEDs) and displays) [45–50]. Their performance in these applications is driven by their fantastic physical/chemical properties, such as size-dependent optoelectronic characteristics and tunable energy band gaps resulting from quantum confinement, high photon absorption coefficient, and multiple exciton generation. In particular, their facile solution synthesis, controllable energy-level structures, and easily exchanged surface-ligands make QDs attractive candidates for many significant functions in PSCs (Fig. 3). For example, SnO_2 and black phosphorus QDs have been utilized as electron transporters in ETLs [51–53]; various organic/inorganic halide perovskite QDs (e.g., $MAPbI_3$, $FAPbI_3$, $CsPbI_3$, $CsPbBr_3$ and $Cs_{1-x}FA_xPbI_3$) have been used as light absorbers [46,54–59]; and a diversity of metal oxides, sulfides and selenides (e.g., Cu_2O, $CuInS_2$, $CuInSe_2$, MoS_2, PbS and SnS) have been employed as hole transporters in HTLs [60–65]. Additionally, the nano size of QDs allows them to be easily incorporated into modified perovskite films, ETLs and HTLs by simply suspending them in precursor solutions [3,66,67]. The adjustable energy band characteristics of QDs enable them to be good mediators for interfacial engineering in PSCs [68,69]. Carbon-based (e.g., graphene, carbon and graphdiyne) and phosphorus-based (e.g., black phosphorus) QDs are the most commonly used additives and interfacial modifiers in PSCs [70–74]. QDs have been used for a wide spectrum of important functions in PSCs, for example, extending the light absorption from ultraviolet to near infrared light due to their photoluminescence property and low energy band gaps [75,76], improving the quality of perovskite films (spurring larger grain sizes and reducing surface defects) owing to the strong chemical interaction between QDs and perovskites [77–80], alleviating the carrier recombination in the charge transport layers due to the passivation effect of QDs [81,82], facilitating charge extraction via tailored energy-level alignment [83,84], reducing photocurrent hysteresis [71,85], and enhancing the long-term, humidity, thermal and photostability of PSCs owing to the introduction of QDs with several fascinating characteristics (e.g., hydrophobicity and photoluminescence) [86–88]. Impressively, most QD materials are capable of multiple roles in PSCs. They can multifariously act as active materials (i.e., light harvester and carrier transporters) [89], function as dopants in active layers, and operate as interfacial modifiers in PSCs (Fig. 4) [90]. This is principally owing to their fascinating features,

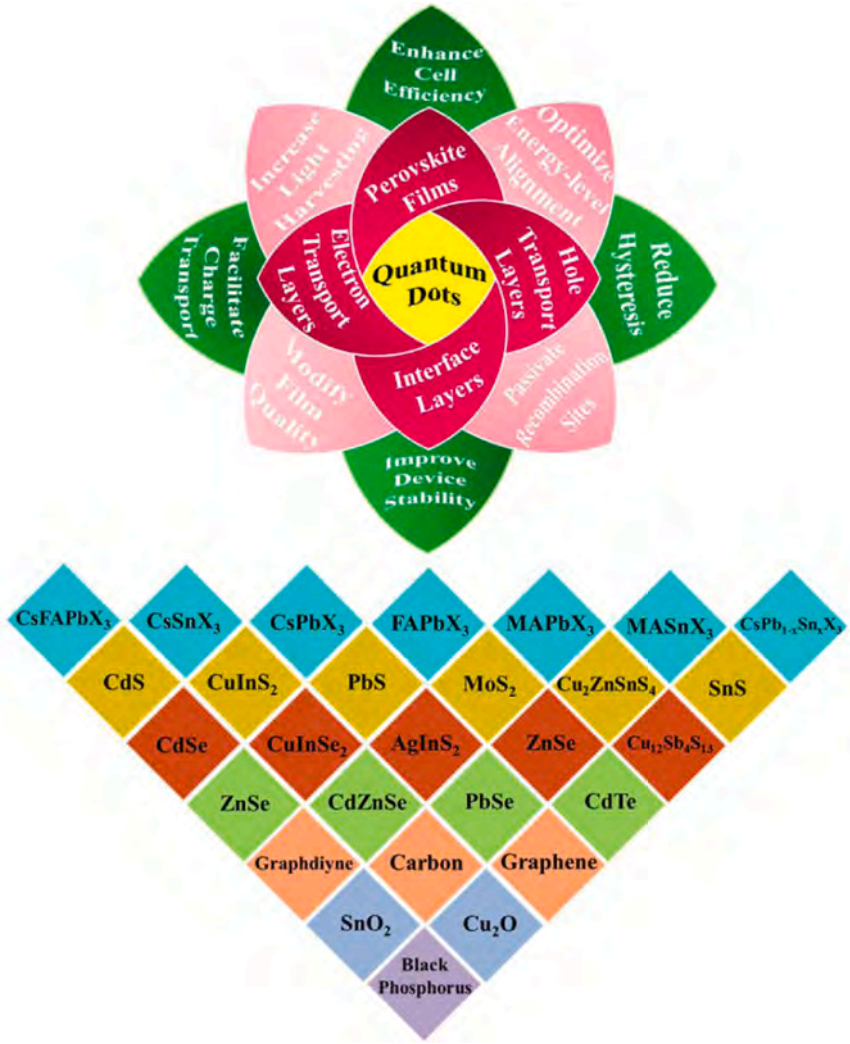

Fig. 3. Schematic diagrams of the applications of QDs in PSCs. Top: The roles (red petals) and functions (pink and green petals) of QD materials in PSCs. Bottom: some representative materials in the form of QDs used in PSCs.

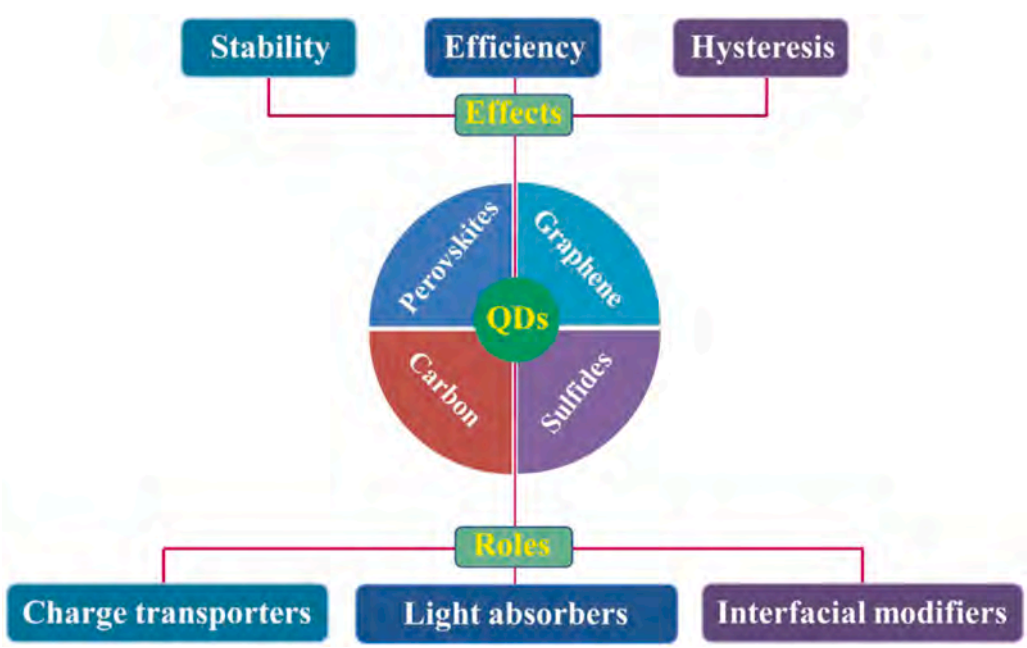

Fig. 4. Schematic diagram of some multifunctional quantum dot materials with their roles and effects in PSCs.

such as tailorable surface chemistry for varying functional ligands, adjustable dispersion ability in polar or non-polar solvents, and tunable energy-level structures [91,92].

In this review, the recent progress on incorporating various QD materials in PSCs is comprehensively summarized. A diverse group of QD materials (e.g., carbon, graphene, black phosphorus, metal sulfides/oxides, and halide perovskites) have been introduced into PSCs for a variety of functions. Since the synthesis of QDs has been carefully summarized in many related reviews [35,93], we primarily emphasize the roles and functions of QDs in PSCs, including their ability to serve as light harvesters (e.g., organic/inorganic halide perovskites) [94–96], charge transporters (e.g., metal sulfides) [61,63,64], film additives (e.g., graphene, carbon and graphdiyne) [67,68,81], and interfacial modifiers (e.g., metal sulfides, selenides and tellurides, black phosphorus, graphene and carbon) [69,85,97,98]. Finally, our concluding remarks and perspectives are outlined.

Quantum dots applied in perovskite solar cells

As mentioned above, QD materials can be utilized in many parts of PSCs. In the following sections we will survey their applications in ETLs, perovskite layers, and HTLs, respectively. Their use at the interfaces between perovskite and charge transport layers (i.e., ETLs and HTLs) will then be examined. Finally, the role of QDs as light down converting materials in PSCs will be highlighted.

Quantum dots used in electron transport layers

Quantum dots as electron transport materials

In PSCs, ideal electron transport materials possess the following basic properties: (1) large optical transmittance to enable adequate light into the perovskites; (2) appropriate energy-level alignment to allow effective electron extraction from perovskite to ETLs and obtain a high open-circuit voltage (V_{OC}); (3) high electron mobility to quickly deliver the photo-generated electrons from ETLs to the external circuit. As shown in Fig. 2d, TiO_2, SnO_2, and PCBM are the most common electron transport materials in PSCs. Among them, TiO_2 is often the preferred choice as compact layers and mesoporous scaffolds for PSCs due to its appropriate energy band structure and suitable physical/chemical properties. TiO_2 is, however, not without drawbacks, which include relatively low electron mobility (~10^{-4} cm^2 V^{-1} s^{-1}), inferior conductivity (~1.1×10^{-5} S cm^{-1}), strong photocatalytic activity under UV light, and prolonged high temperature (>450 °C) to calcine [3,82]. In recent years, SnO_2 has attracted significant attention as ETLs in PSCs due primarily to its compelling properties, including a favorable conduction band energy level across the ETL/perovskite interface, a wider band gap for improved stability under UV light exposure, and higher electron mobility (~10^{-3} cm^2 V^{-1} s^{-1}) than TiO_2 [81]. Moreover, SnO_2 nanocrystals can be easily fabricated via low temperature processes in large scale, which is necessary for the fabrication of flexible PSCs [99].

As summarized in Table 1 [36,51–53,100–105], SnO_2 QDs have been extensively applied in PSCs owing to their facile, large-scale, stable, efficient and repeatable synthesis processes. For example, thiourea-stabilized SnO_2 QDs with the diameters of 3–5 nm can be obtained by hydrolyzing, dehydrating, and oxidizing $SnCl_2{\cdot}2H_2O$ in water at room temperature (Fig. 5a and b) [52,100,101]. Rigid, flexible, and large area (1.0 cm^2) PSCs were then crafted using these SnO_2 QDs, and they displayed impressive power conversion efficiencies (PCEs) of 20%, 16.97%, and 19.05%, respectively (Table 1) [52]. Similarly, SnO_2 QDs synthesized by dissolving $SnCl_2{\cdot}2H_2O$ in anhydrous ethanol can be deposited into homogeneous ETLs [51]. These SnO_2 QD-based films show higher conductivity and photovoltaic performance than that of films prepared by spin-coating the $SnCl_2{\cdot}2H_2O$ solution onto substrates (Fig. 5c and d). The PCE of PSCs based on such SnO_2 QD films can reach 20% (vs. 17.50% for bulk SnO_2-

Table 1
Summary of some representative QDs as ETLs in PSCs.

QDs (diameter)	Synthesis method	Cell structure	Device performance				Ref.
			η (%)	V_{OC} (V)	J_{SC} (mA cm^{-2})	*FF*	
TiO_2 (~3.6 nm)	Solvothermal reaction	FTO/TiO_2 QDs/m-TiO_2 $MAPbI_3$/Spiro-OMeTAD/Au	16.97	1.06	22.48	0.71	[103]
ZnO (~)	Reflexed solution process	ITO-PET/Graphene/ZnO QDs/$MAPbI_3$/Spiro-OMeTAD/Ag	9.73	0.94	16.80	0.62	[104]
Black phosphorus (4.7 ± 1.6 nm)	Liquid exfoliation process	ITO-PEN/Black phosphorus QDs/ $FA_{0.85}MA_{0.15}PbI_{0.25}Br_{0.5}$/Spiro-OMeTAD/Au	11.26	1.03	16.77	0.65	[53]
Graphene (~4 nm)	Solvothermal reaction	FTO/Graphene QDs/ $CsPbBr_3$/$CsPbBrI_2$ QDs /Carbon	4.10	1.21	5.08	0.67	[105]
SnO_2 (3–5 nm)	Room temperature solution process	ITO/SnO_2 QDs/ $Cs_{0.05}(MA_{0.17}FA_{0.83})_{0.95}Pb(I_{0.83}Br_{0.17})_3$/Spiro-OMeTAD/Au	20.78	1.13	23.05	0.80	[52]
SnO_2 (~2.9 nm)	Low temperature water injection process	ITO/SnO_2 QDs/ $MAPbI_3$/Spiro-OMeTAD/Au	18.71	1.12	21.61	0.77	[36]
SnO_2 (2–4 nm)	Room temperature solution process	FTO/SnO_2 QDs/ $MA_{0.7}FA_{0.3}PbI_3$/Spiro-OMeTAD/Au	18.80	1.08	23.40	0.74	[51]
			17.50 (bulk)	1.09	22.60	0.70	
SnO_2 (1.7–3.3 nm)	Room temperature solution process	FTO/Al:SnO_2 QDs/ $MAPbI_3$/Spiro-OMeTAD/Ag	18.20	1.06	22.78	0.75	[101]
SnO_2 (~3 nm)	Room temperature solution process	ITO/SnO_2 QDs/ $Cs_{0.05}FA_{0.81}MA_{0.14}PbI_{2.55}Br_{0.45}$/Carbon	13.64	1.08	22.19	0.57	[100]
SnO_2 (1.7–3.3 nm)	Room temperature solution process	ITO/SnO_2 QDs/ $MAPbI_3$/Spiro-OMeTAD/Ag	16.58	1.06	21.89	0.71	[102]

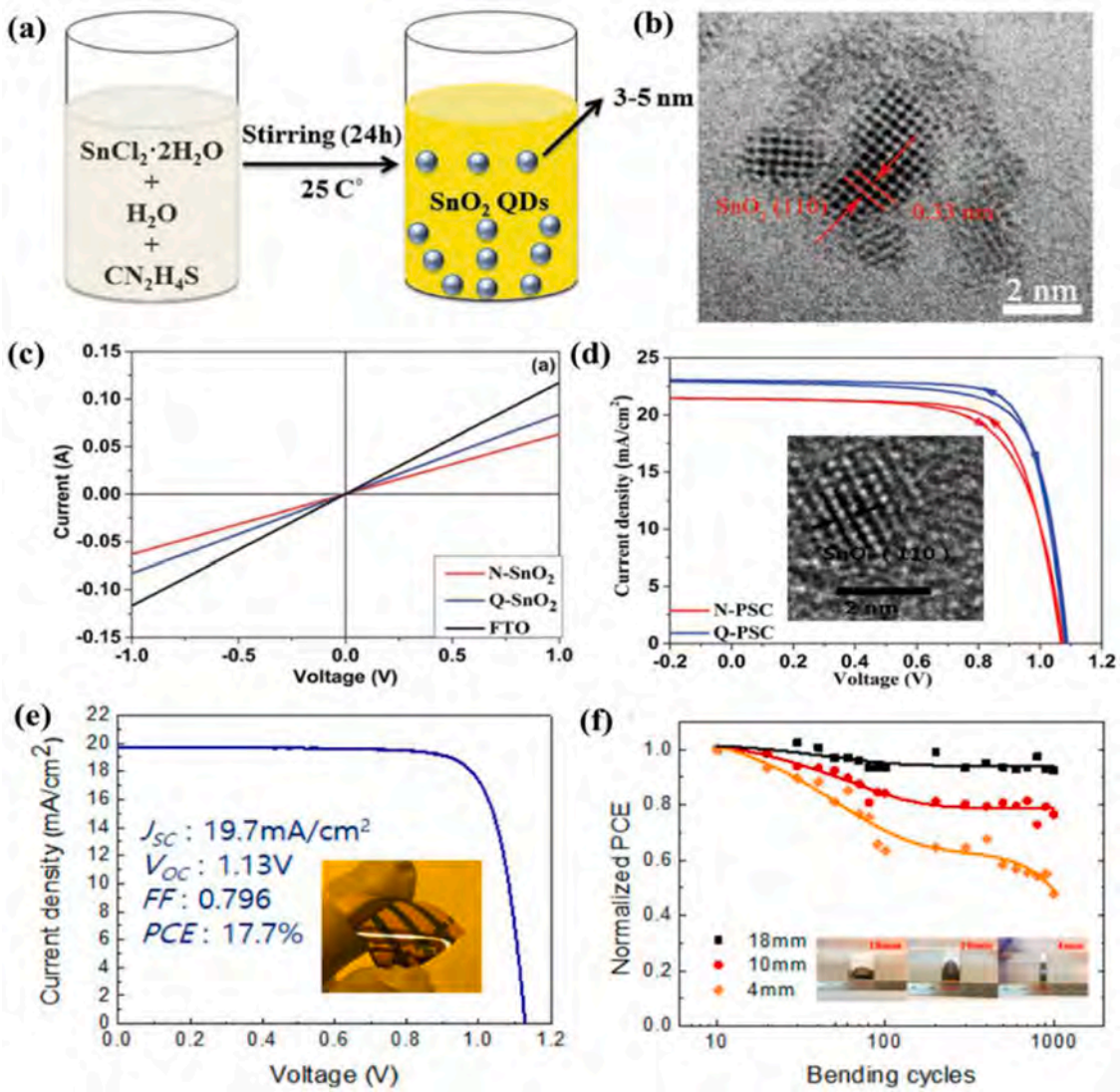

Fig. 5. (a) Schematic diagram of the room temperature solution process for preparing SnO_2 QDs and (b) TEM image of SnO_2 QDs [52]. Printed with permission from Wiley-VCH. (c) I-V curves of SnO_2 QDs (Q-SnO_2), bulk SnO_2 (N-SnO_2) films and FTO/glass. (d) J-V curves of the PSCs based on Q-SnO_2 and N-SnO_2 ETLs, inset is the TEM image of SnO_2 QDs [51]. Printed with permission from The Royal Society of Chemistry. (e) J-V curve of the flexible PSCs based on the SnO_2 QDs and (f) bending tolerance of the flexible PSCs under different bending radii [36]. Printed with permission from American Chemical Society.

based PSCs) [51]. In addition, well-dispersed SnO_2 QDs with uniform sizes can be prepared by dissolving tin acetate ($Sn(CH_3CO_2)_4$) in xylene with oleylamine and oleic acid, and then inducing reverse micellar formation via water injection at low temperature (<100 °C). Flexible PSCs made with these QDs showed a high efficiency of 17.7% and maintained 92% retention after a 1000-cycle bending to a radius of 18 mm (Fig. 5e and f) [36]. Moreover, $AlCl_3$ was mixed into a $SnCl_2{\cdot}2H_2O$ precursor solution to synthesize Al-doped SnO_2 QDs, which exhibited obviously improved conductivity, charge mobility, and energy-level alignment as compared to the pure SnO_2 QDs. Impressively, the doping process also modified the film quality of SnO_2 and perovskite layers. Thus, the resulting PSCs display a PCE over 18.20% [101].

Black phosphorus, an exciting new two-dimensional (2D) material, has recently spurred significant research interest because of its attractive characteristics, including tunable band gap from 0.3 to 2.0 eV and ambipolar conductivity (e.g., carrier mobility in polycrystalline: ~220 $cm^2\ V^{-1}\ s^{-1}$ for electrons and ~350 $cm^2\ V^{-1}\ s^{-1}$ for holes) [106]. When black phosphorus is shrunk into QDs, quantum confinement and edge effects produce more fascinating optoelectronic properties. For instance, black phosphorus QDs can be synthesized via a liquid exfoliation method assisted by bath and probe sonication (Fig. 6a). These black phosphorous QDs can then be used as ETLs in planar n-i-p PSCs and have been found to facilitate crystallization and orientation of perovskite films with reduced surface defects (Fig. 6b and c). Meanwhile, they also generate suitable energy-level alignment to promote electron extraction (Fig. 6d and e), thereby leading to PCEs of 14.6% and 11.26% for the resulting rigid and flexible PSCs (Fig. 6f), respectively [53]. Graphene QDs have also been found to serve as a good charge deliverer, promoting electron extraction from $CsPbBr_3$ films to ETLs [105].

Quantum dots as additives into electron transport layers

As summarized in Table 2, the doping of some QD materials (such as CdSe, $AgInS_2$, carbon and graphene) into TiO_2, SnO_2 and PCBM ETLs has been found to effectively facilitate electron transport and

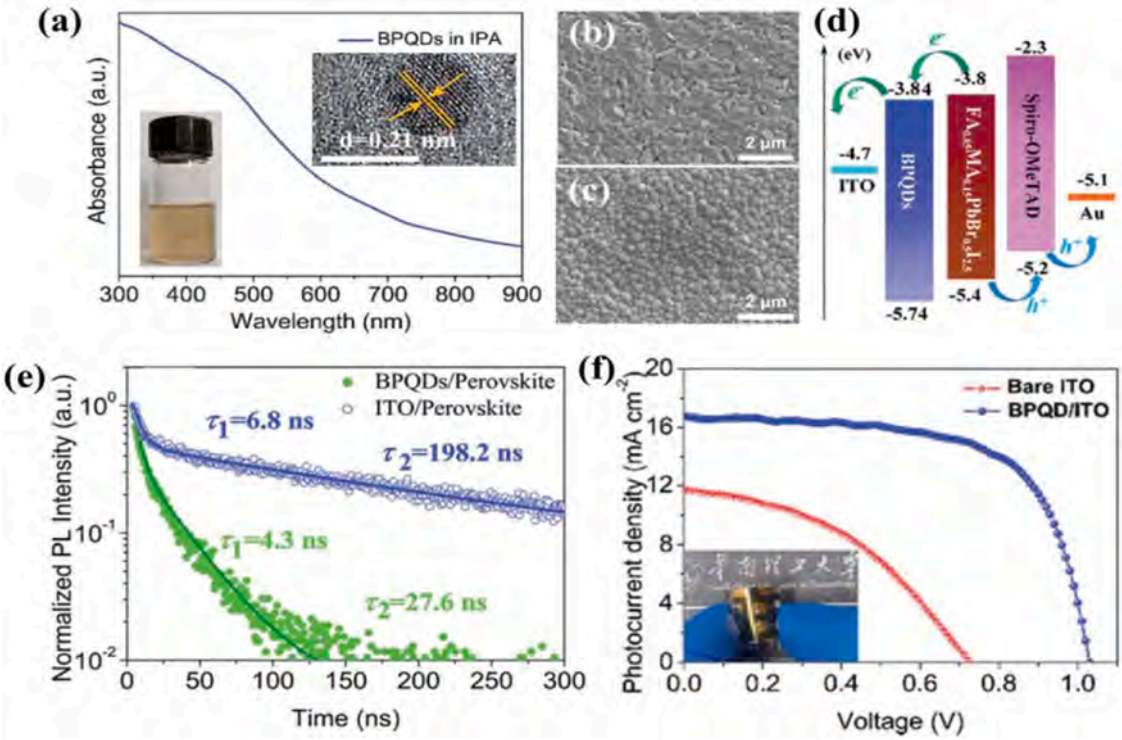

Fig. 6. (a) UV–Vis absorption spectrum of black phosphorous QDs (BPQDs) in isopropanol (IPA) solution, the inset is the TEM image of BPQDs. SEM images of the perovskite films prepared (b) with and (c) without the presence of BPQDs. (d) Schematic diagram of the energy-level structure of the PSCs based on BPQDs. (e) Time-resolved photoluminescence decay plots of the perovskite films with/without BPQDs. (f) J-V curves of the flexible PSCs with/without BPQDs [53]. Printed with permission from The Royal Society of Chemistry.

extraction and improve the long-term humidity stability of PSCs [3,70,81,82,98,107–113]. Carbon-based materials, including carbon nanotubes, graphene, graphite, and fullerene are popular functional materials due to their beneficial optoelectronic properties [40,114–116]. Graphene and carbon QDs in particular have been studied in a variety of applications, including batteries [117], solar cells [118,119], photodetectors [120], and LEDs [50]. In contrast to graphene nanosheets with zero band gap and low light absorption, dispersible graphene QDs with sp^2-sp^2 carbon bonds have non-zero and tunable band gaps, broad optical absorption, and fluorescent properties due to the quantum confinement and edge effects [121]. Carbon QDs are composed of sp^2 hybridized core carbon atoms and surfaces passivated with numerous functional groups (e.g., carbonyl, hydroxyl, and carboxyl). These surface groups enable carbon QDs to have great water solubility and high chemical interaction with other materials for efficient surface passivation [122]. Because of their solubility, abundant surface groups, photoluminescence, high photostability, facile synthesis and low toxicity, graphene and carbon QDs are promising candidates for significant roles in PSCs [122,123].

For example, graphene QDs have been shown to boost the performance of SnO_2 based ETLs. Although SnO_2 has several advantages as above mentioned, thin films prepared via low-temperature solution processes unavoidably contain many electron traps from oxygen vacancies in SnO_2 QDs. These traps result in carrier recombination and deteriorated electron transport in the ETL and ETL-perovskite interfaces. The incorporation of a small amount (e.g., 5 wt%) of graphene QDs (Fig. 7a) into the $SnCl_2$ or SnO_2 solution has been demonstrated to significantly reduce electron trap-state density and improve electron mobility in the modified ETLs. Moreover, the conduction band (E_c) of the graphene QDs is higher than that of SnO_2 (Fig. 7b and d), which facilitates efficient electron transport from the graphene QDs to SnO_2, quickly filling electron traps, increasing the electron density in ETLs, and ultimately enhancing conductivity. The graphene QDs also enhanced energy-level alignment between ETL and perovskite, resulting in superior electron extraction (Fig. 7b and e). Thus, the PSCs based on the SnO_2/graphene QD ETLs show higher PCEs and reduced photocurrent hysteresis (Fig. 7c and f) [70,82,110].

Similarly, graphene QDs can also be applied to compensate for the inherent shortcomings of PCBM, namely inferior electrical conductivity and electron mobility [68,124]. PCBM molecules have also been found to dimerize when exposed to continuous light illumination, a phenomenon which leads to deteriorated PSC performance. The incorporation of graphene QDs into the PCBM films has been found to suppress such dimerization and stabilize PSCs performance [68]. Graphene QD doping can also improve the electronic and electrochemical properties of TiO_2 ETLs. The introduction of graphene QDs into the TiO_2 films has been found to shift the flat-band potential (E_{fb}) of TiO_2 to a more negative position with a higher quasi-Fermi level, which is beneficial for electron transfer and increases the open circuit voltage (V_{OC}) of PSCs. Moreover, TiO_2 is photocatalytically sensitive to the UV-light and can extract electrons from I^- ions of perovskite, induce the formation of I_2 at perovskite-TiO_2 interface, and degrade the PSC. Significantly, the addition of graphene QDs into TiO_2 films has been observed to protect TiO_2 from the UV-light radiation, alleviate the interaction between TiO_2 and perovskites, and reduce the decay of PSCs [111].

In addition, carbon QDs can also be mixed with TiO_2 nanocrystals to prepare a hybrid ETL. A PSC made with this hybrid ETL was found

Table 2
Summary of some representative QDs doped into ETLs for PSCs.

QDs (diameter)	Synthesis method	Cell structure	Cell performance				QD effect	Ref.
			η (%)	V_{OC} (V)	J_{SC} (mA cm^{-2})	*FF*		
CdSe (~10 nm)	Solvothermal reaction	ITO/PEDOT:PSS/ $MAPbI_{3-x}Cl_x$/PCBM:CdSe QDs/LiF/Ag	13.73 11.22 (pure)	0.90 0.91	20.96 19.29	0.73 0.64	Improve film quality of perovskite, and enhance moisture stability of PSCs	[109]
Carbon (~10 nm)	Ultrasonic chemical process	ITO/TiO_2:Carbon QDs/$MAPbI_3Cl_{3-x}$/Spiro-OMeTAD/Au	18.89 15.15 (pure)	1.14 1.04	21.36 19.10	0.78 0.77	Increase electronic coupling and match energy-level alignment between TiO_2 and perovskite	[3]
Carbon (~4 nm)	Hydrothermal reaction	FTO/PEDOT:PSS/ $MAPbI_3$/PCBM:Carbon QDs/BCP/Ag	18.1 16.10 (pure)	0.97 0.96	22.30 21.90	0.80 0.77	Improve electron mobility of ETLs, modify energy-level alignment between PCBM and perovskite, and enhance long-term stability of PSCs	[112]
Red carbon (–)	Solvothermal reaction	ITO/SnO_2:Red carbon QDs/ $Cs_{0.05}(MA_{0.17}FA_{0.83})_{0.95}Pb(I_{0.83}Br_{0.17})_3$/Spiro-OMeTAD/$MoO_3$/Au	22.77 19.15 (pure)	1.14 1.07	24.1 23.10	0.83 0.78	Increase electron mobility of ETLs, promote crystallization of perovskites, and enhance long-term stability of PSCs	[81]
Graphene (5–10 nm)	–	ITO/SnO_2:Graphene QDs/$MAPbI_3$/Spiro-OMeTAD/Au	20.31 17.91 (pure)	1.13 1.10	23.05 22.10	0.78 0.74	Improve conductivity and reduce electron traps of ETLs, and alleviate photocurrent hysteresis of PSCs	[70]
Graphene (~5 nm)	–	ITO/PCBM: Graphene QDs/ $MAPbI_3$/Spiro-OMeTAD/Au	17.56 14.68 (pure)	1.09 1.06	22.03 20.57	0.73 0.68	Improve electron mobility and conductivity of ETLs, and enhance long-term light stability of PSCs	[68]
Graphene (5.4–10.9 nm)	Hydrothermal reaction	FTO/SnO_2:Graphene QDs/$MA_{0.17}FA_{0.83}Pb(I_{0.83}Br_{0.17})_3$/Spiro-OMeTAD/Au	19.6 16.7 (pure)	1.08 1.04	23.5 21.7	0.77 0.74	Improve conductivity and film coverage uniformity of ETLs, and modify energy-level alignment between SnO_2 and perovskite	[82]
Graphene (–)	–	ITO/SnO_2:Graphene QDs/$MAFAPbI_xCl_{3-x}$/Spiro-OMeTAD/Ag	21.10 18.60 (pure)	1.11 1.07	24.40 22.60	0.78 0.77	Increase electronic coupling and match the energy-level alignment between perovskite and SnO_2, and enhance long-term stability of PSCs	[110]
Graphene (~6 nm)	Hydrothermal reaction	ITO/c-TiO_2/m-TiO_2:Graphene QDs/ $Cs_{0.05}(MA_{0.17}FA_{0.83})_{0.95}Pb(I_{0.83}Br_{0.17})_3$/Spiro-OMeTAD/Au	14.36 12.87 (pure)	0.97 1.00	21.92 19.76	0.67 0.65	Improve film quality of perovskite, reduce electron traps of ETLs, and enhance long-term stability of PSCs	[111]

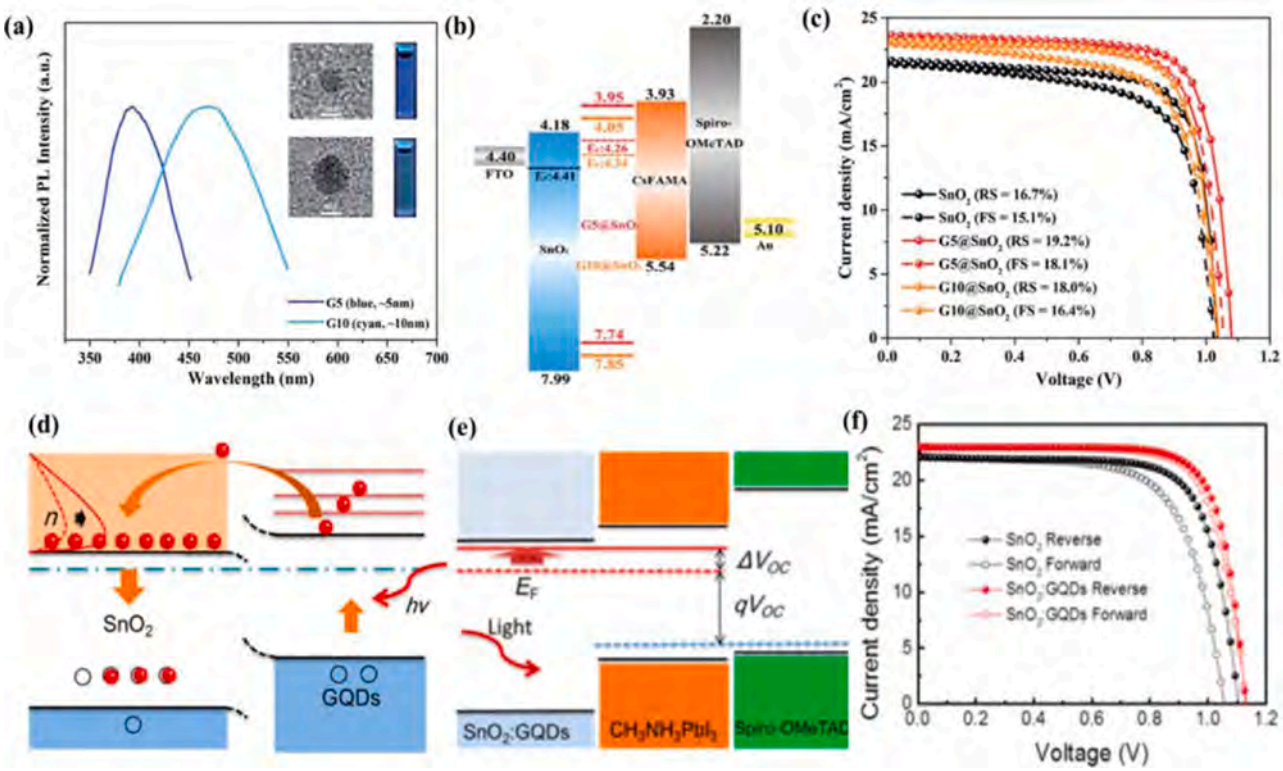

Fig. 7. (a) Steady-state PL spectra of the GQDs with diameters of 5 nm (G5) and 10 nm (G10), respectively. (b) Schematic diagram of the energy-level alignment and (c) J-V curves of PSCs using different SnO_2 ETLs [82]. Printed with permission from The Royal Society of Chemistry. Schematic diagrams of (d) the energy bands between SnO_2 and graphene QDs (GQDs) and (e) energy-level alignment of PSCs based on the SnO_2:GQD ETL. (f) J-V curves of the PSCs based on the SnO_2 and SnO_2:GQD ETLs, respectively [70]. Printed with permission from American Chemical Society.

to have a superior PCE and reduced hysteresis, which were attributed to the well-matched energy-band structure, improved charge extraction, and stronger electronic coupling between the perovskite and ETL [3]. Moreover, red carbon QDs with rich −SH and −OH groups have been doped into the SnO_2 solution to prepare ETLs with increased electron mobility of 1.73×10^{-2} cm^2 V^{-1} s^{-1} [81]. The SnO_2/red carbon QD ETLs were smoother and more hydrophilic, which promoted heterogeneous nucleation of perovskite films with larger grain sizes and a higher degree of crystallization. PSCs made with such high-quality perovskite films reached a PEC of 22.77% (vs. 19.15% for unmodified PSCs), due to increased light absorption, reduced charge traps, and decreased carrier recombination [81].

Quantum dots used in perovskite absorbers

Perovskite quantum dots for light harvesting

Perovskite QDs have recently emerged as promising candidates for use in high-performance PSCs due to their unique properties, such as low-temperature synthesis, tunable band gaps, high photoluminescence, multiple exciton generation, large absorption coefficient, high carrier mobility, long charge diffusion length, and low exciton binding energy [49]. It is important to note that because of their higher surface energy, perovskite QDs possess superior stability to their bulk counterparts, which are often thermodynamically unstable at low (room) temperature [66,125,126]. Thus, as indicated in Table 3 [5,54–57,94,96,127–143], a series of perovskite QDs have been rationally designed and used as light harvesters in PSCs, and resulted in increased PCE from 6.54% to 16.60% and considerably enhanced stability [5,56,144,145].

In general, perovskite QDs are necessarily passivated by surface ligands (e.g., oleic acid (OA) and oleylamine (OLA)) to avoid particle aggregation and achieve dispersion in various solvents [54,146]. Unfortunately, the insulating nature of these long ligands (e.g., OA and OLA both have 18 carbon atoms) can create a high potential barrier for effective electrical coupling among perovskite QDs which can lead to poor charge transport and low PCEs. Therefore, it is essential to replace the long-chain ligands with short-chain ones. However, this ligand exchange process has been found to induce surface defects in perovskite QDs, which are detrimental to carrier transfer and stability [134,143]. Simply stated, it is complicated yet necessary to carefully address the surface ligands of perovskite QDs to assemble efficient PSCs.

Initially, perovskite QDs (e.g., $MAPbI_3$ and $MAPbBr_3$) were fabricated via in-situ spin-coating perovskite precursor on substrates [5,127], with particle sizes (3–10 nm) readily controlled by adjusting the spin-coating speed. A maximum PCE of 11.40% was obtained for the PSCs based on $MAPbBr_3$ QDs created with this method [127]. In 2016, Luther et al. synthesized $CsPbI_3$ QDs via the hot injection method by introducing Cs-oleate into a flask containing PbI_2 with OA and OLA surface ligands [96]. Due to the ionic nature of $CsPbI_3$ QDs and the bonding between the ligands and QDs, the presence of polar solvents will result in the desorption of ligands and transformation from the desired cubic phase to the thermodynamically preferred orthorhombic phase of $CsPbI_3$. Thus, to successfully obtain cubic phase $CsPbI_3$ QDs without particle aggregation, the use of low polarity solvents (e.g., methyl acetate) is required to remove unreacted precursors and surface species [54]. By tuning the reaction temperatures from 60 °C to 185 °C (Fig. 8a), the particles sizes of $CsPbI_3$

Table 3
Summary of some representative perovskite QDs as light harvesters in PSCs.

QDs (diameter)	Synthesis method	Ligands	Cell structure	Cell performance				Device stability	Ref.
				η (%)	V_{OC} (V)	J_{SC} (mA cm^{-2})	FF		
$MAPbI_3$ (2–3 nm)	Spin-coating process	\	FTO/c-TiO_2/m-TiO_2/$MAPbI_3$ QDs/Iodine redox electrolyte/Pt	6.54	0.71	15.82	0.59	Maintain 80% decay for 10 min under continued irradiation	[5]
$MAPbBr_3$ (~2 nm)	Spin-coating process	\	FTO/c-TiO_2/m-TiO_2/ $MAPbBr_3$ QDs/ PTAA/Au	11.40	1.11	14.07	0.73	Keep stable for more than four months	[127]
$FAPbI_3$ (17.7 ± 2.5 nm)	Hot-injection process	Oleic acid, oleylamine	ITO/SnO_2/$FAPbI_3$ QDs/Spiro-OMeTAD/Au	8.38	1.10	11.83	0.64	Show no degradation for 60 days under ambient conditions	[55]
$FAPbI_3$ (7–12 nm)	Hot-injection process	Oleic acid, oleylamine	ITO/c-TiO_2/$FAPbI_3$ QDs/ Spiro-OMeTAD/Au	9.40	1.05	13.3	0.67	–	[142]
$Cs_{0.75}FA_{0.25}PbI_3$ (~10 nm)	Hot-injection + cation exchange process	Oleic acid, oleylamine	ITO/c-TiO_2/$Cs_{0.75}FA_{0.25}PbI_3$ QDs/Spiro- OMeTAD/ MoO_x/Al	11.14 8.52 ($FAPbI_3$ QDs) 13.47 ($CsPbI_3$ QDs)	1.15 1.12 1.18	14.36 11.81 15.50	0.68 0.64 0.73	–	[57]
$Cs_{0.5}FA_{0.5}PbI_3$ (12 ± 2 nm)	Hot-injection + cation exchange process	Oleic acid, oleylamine	ITO/SnO_2/$Cs_{0.5}FA_{0.5}PbI_3$ QDs/Spiro-OMeTAD/ Au	16.60 9.60 ($CsPbI_3$ QDs)	1.17 1.16	18.30 15.40	0.78 0.54	Keep 94% of the original PCE without encapsulation after 600 h	[56]
$CsPbI_3$ (3–12.5 nm)	Hot-injection process	Oleic acid, oleylamine	ITO/c-TiO_2/$CsPbI_3$ QDs/ Spiro-OMeTAD/MoO_x/Al	10.77	1.23	13.47	0.65	Keep stable for 60 days in dry but ambient conditions	[96]
$CsPbI_3$ (~10 nm)	Hot-injection process	Oleic acid, oleylamine	FTO/c-TiO_2/$CsPbI_3$ QDs/ Spiro-OMeTAD/MoO_x/Al	13.40	1.20	14.37	0.78	–	[129]
$CsPbI_3$ (~8 nm)	Hot-injection process	Oleic acid, oleylamine	FTO/c-TiO_2/$CsPbI_3$ QDs/ PTB7/MoO_3/Ag	12.55	1.27	12.39	0.80	–	[132]
$CsPbI_3$ (~10 nm)	Hot-injection process	Oleic acid, oleylamine, octanoic acid, octylamine	FTO/c-TiO_2/$CsPbI_3$ QDs/ Spiro-OMeTAD/Au	11.87	1.04	16.98	0.67	The PL intensity of $CsPbI_3$ QDs maintains ~ 80% after 180 days	[134]
Yb-doped $CsPbI_3$ (~12 nm)	Hot-injection process	Oleic acid, oleylamine	FTO/c-TiO_2/Yb-doped $CsPbI_3$ QDs/ PTB7/MoO_3/Ag	13.12 12.06 (without doping)	1.25 1.25	14.18 12.86	0.74 0.75	Keep 68% of the original PCE after one week in a dry ambient environment without encapsulation	[137]
$CsPbI_3$ (~12 nm)	Hot-injection process	Oleic acid, oleylamine	FTO/c-TiO_2/$CsPbI_3$ QDs/ Spiro-OMeTAD/Au	12.15	1.11	14.80	0.74	Retain 85% of its initial performance in dry air for 90 days	[136]
$CsPbI_3$	Hot-injection process	Oleic acid, oleylamine	FTO/c-TiO_2/$CsPbI_3$ QDs/ PTAA/MoO_3/Ag	14.10	1.25	14.96	0.76	Keep 70% of the initial PCE in air with humidity of 40% for 54 h	[135]
$CsPbI_3$ (~9.1 nm)	Hot-injection process	Oleic acid, oleylamine	FTO/c-TiO_2/m-TiO_2/$CsPbI_3$ QDs/ Spiro-OMeTAD/Au	14.32	1.06	17.77	0.76	–	[141]
$CsPbI_3$ (~30 nm)	Spin-coating process	1-Adamantanemethylamine	FTO/c-TiO_2/$CsPbI_3$ QDs/ Spiro-OMeTAD/Au	13.38 10.10 (bulk)	1.06 1.01	16.87 16.03	0.75 0.63	Keep 90% of its initial performance in ambient air for 30 days or at 85 °C for 336 h	[143]
$CsPbBr_3$ (7.2 ± 1.5 nm)	Hot-injection process	Oleic acid, oleylamine	FTO/c-TiO_2/m-TiO_2/$CsPbBr_3$ QDs/ Spiro-OMeTAD/Au	4.21	0.86	8.55	0.57	–	[94]
$CsPbBr_3$ (15–20 nm)	Hot-injection process	Oleic acid, oleylamine	FTO/ZnO/$CsPbBr_3$ QDs/ Spiro-OMeTAD/Au	6.81	1.43	6.17	0.77	Show no decay for 100 days under dark storage or operating conditions (25 °C, humidity of 45%)	[133]
$CsPbX_3$ (~10 nm)	Hot-injection process	Oleic acid, oleylamine	FTO/c-TiO_2/$CsPbBr_3$ QDs/ Spiro-OMeTAD/MoO_3/Ag	2.65 ($CsPbBr_3$) 5.27 ($CsPbBr_2I$) 7.94 ($CsPbBr_{1.5}I_{1.5}$) 7.04 ($CsPbBrI_2$) 9.47 ($CsPbI_3$)	0.90 0.96 1.00 0.97 1.06	7.38 9.31 11.35 11.72 12.24	0.40 0.59 0.70 0.62 0.73	Maintain 88% of the initial efficiency for the $CsPbBr_{1.5}I_{1.5}$ based PSCs in air for 35 h	[130]
$CsSn_{0.6}Pb_{0.4}I_3$ (11–14 nm)	Hot-injection process	Oleic acid, oleylamine	FTO/c-TiO_2/m-TiO_2/ $CsSn_{0.6}Pb_{0.4}I_3$ QDs/Spiro-OMeTAD/Au	0.1	0.26	0.90	0.42	The $CsSn_{0.6}Pb_{0.4}I_3$ QDs keep stable for months in solution and ambient air	[128]
$CsSnI_3$ (~30 nm)	Low-temperature solution process	Triphenyl phosphite	FTO/PEDOT:PSS/$CsSnI_3$ QDs/ PCBM /Ag	4.13	0.42	23.79	0.41	Have little changes of the initial efficiency in a N_2 glove box without encapsulation for 30 days	[139]

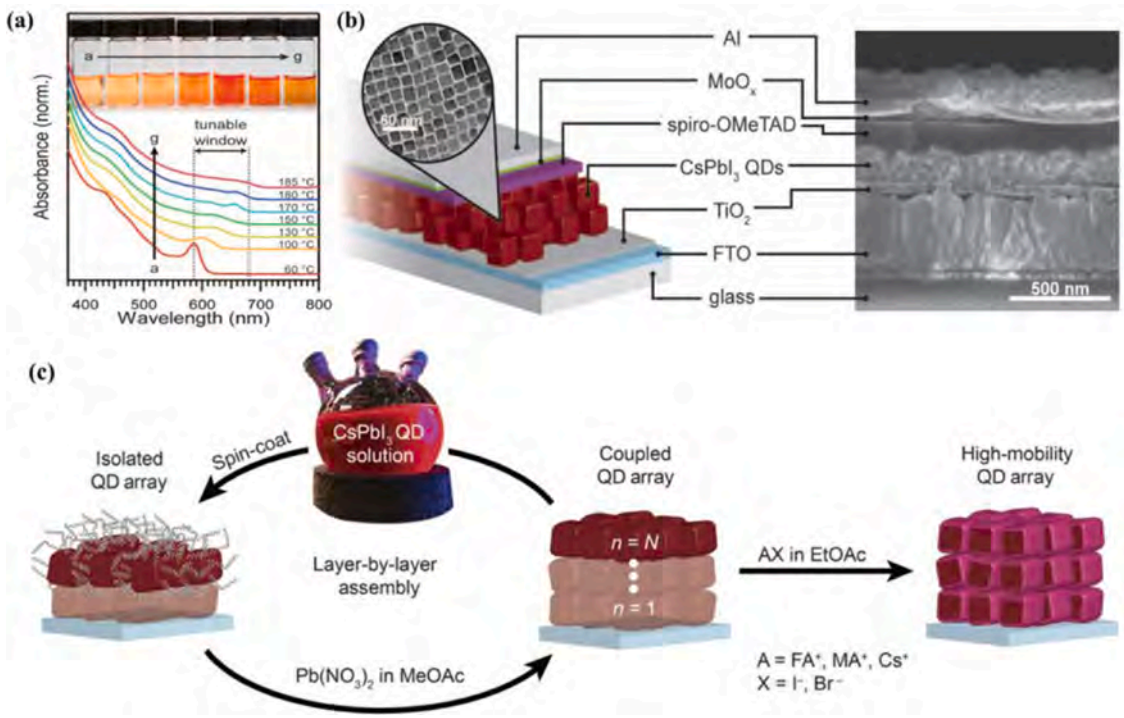

Fig. 8. (a) UV–Vis absorption spectra and photographs of the $CsPbI_3$ QDs fabricated at different temperatures. (b) Schematic diagram and SEM image of the PSC based on the $CsPbI_3$ QDs [96]. Printed with permission from Science Publishing Group. (c) Schematic diagram of the spin-coating process of $CsPbI_3$ films with the post-treatment of different salts [95]. Printed with permission from Science Publishing Group.

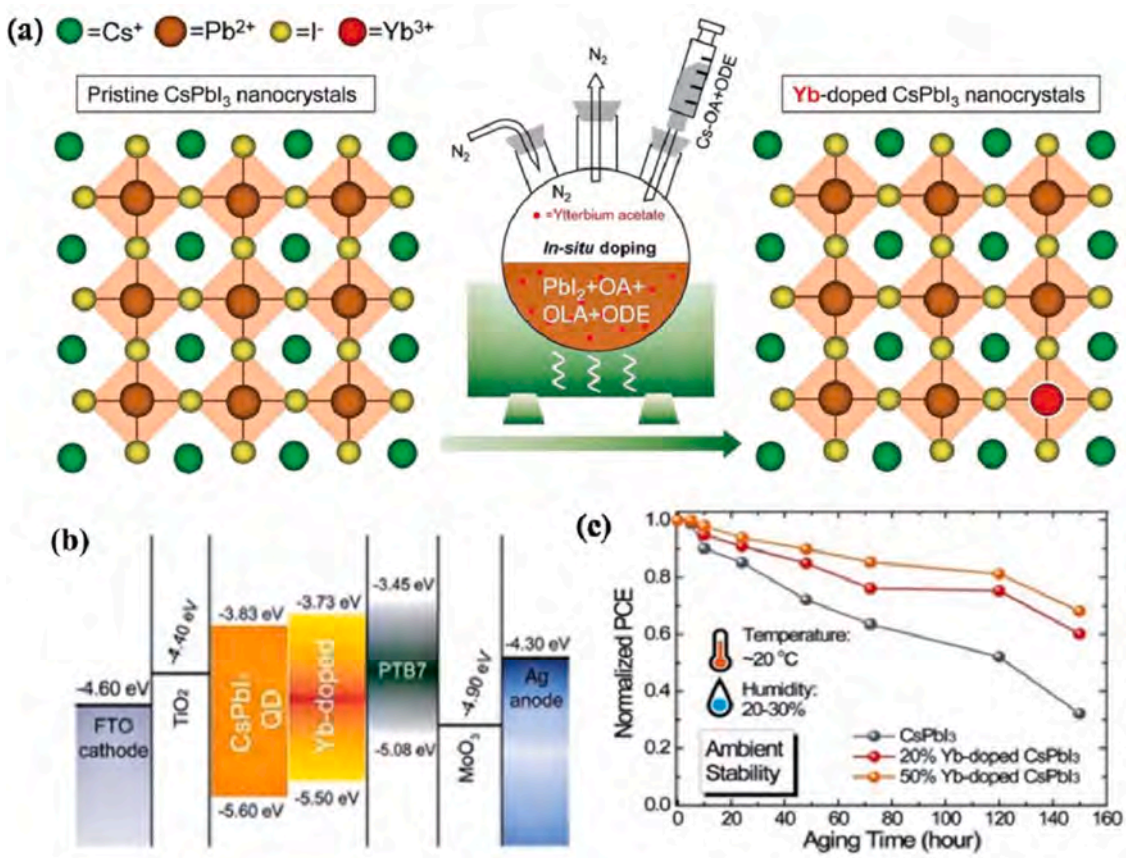

Fig. 9. Schematic illustration of the synthesis process of the Yb-doped $CsPbI_3$ QDs, (b) schematic diagram of the energy band alignment and (c) stability of the PSCs based on Yb-doped $CsPbI_3$ QDs [137]. Printed with permission from The Royal Society of Chemistry.

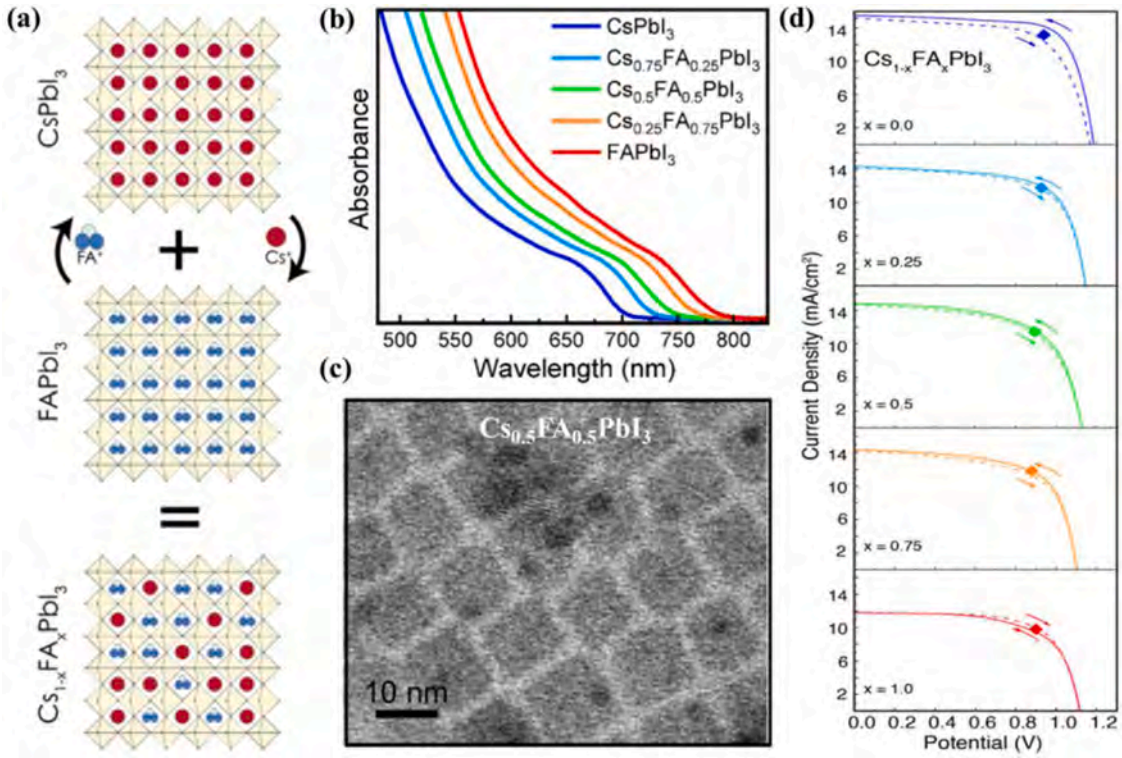

Fig. 10. (a) Schematic diagram of the synthesis of $Cs_{1-x}FA_xPbI_3$ QDs by cation exchange between $CsPbI_3$ and $FAPbI_3$ QDs. (b) UV–Vis absorption spectra of the $Cs_{1-x}FA_xPbI_3$ QDs and (c) SEM image of the $Cs_{0.5}FA_{0.5}PbI_3$ QDs. (d) J-V curves of the PSCs based on the $Cs_{1-x}FA_xPbI_3$ QDs [57]. Printed with permission from American Chemical Society.

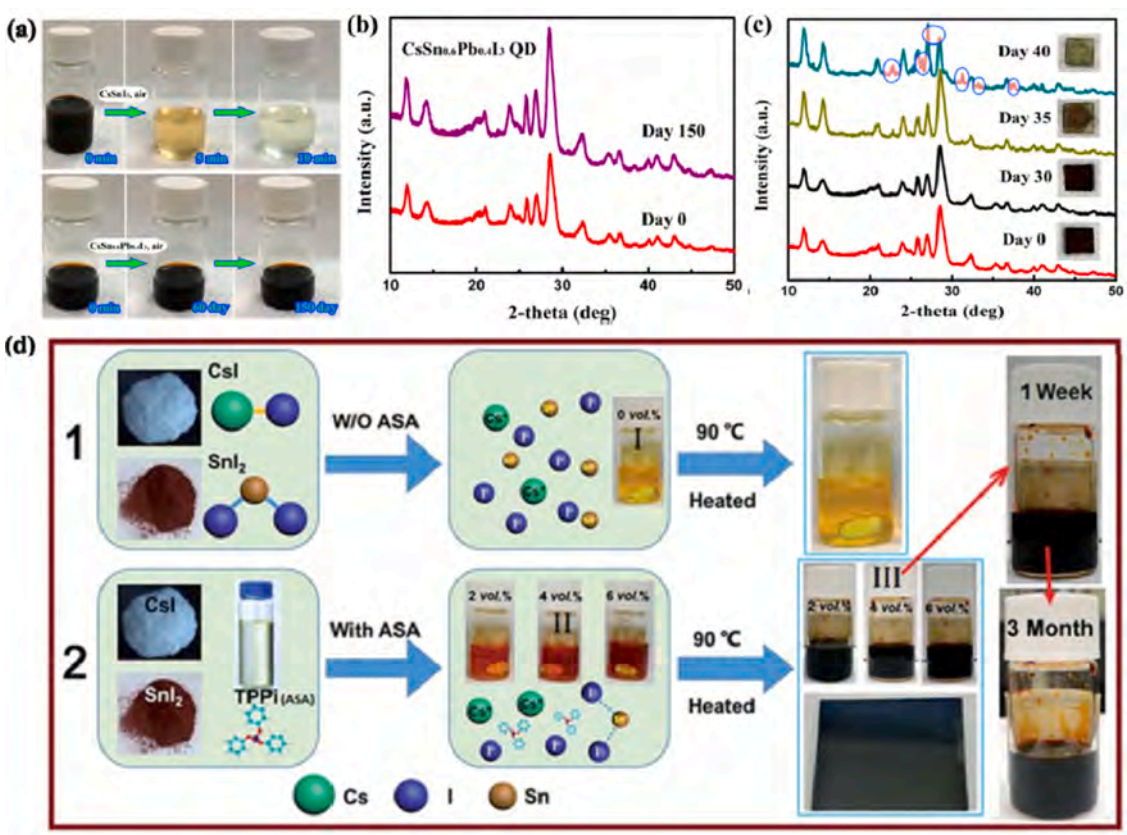

Fig. 11. (a) Photographs of the $CsSnI_3$ and $CsSn_{0.6}Pb_{0.4}I_3$ QDs stored in the air, (b) XRD patterns of $CsSn_{0.6}Pb_{0.4}I_3$ QDs (b) stored in solution and (c) deposited on substrates under ambient conditions [128]. Printed with permission from American Chemical Society. (d) Synthesis process of the $CsSnI_3$ QDs with/without the assistance of anti-oxidant solvent additive (ASA) [139]. Printed with permission from The Royal Society of Chemistry.

Table 4
Summary of some representative QDs embedded into perovskite films for PSCs.

QDs (diameter)	Synthesis method	Cell structure	Cell performance				QD effect	Ref.
			η (%)	V_{OC} (V)	J_{SC} (mA cm^{-2})	*FF*		
PbS (~4 nm)	Hot-injection process	ITO/c-TiO_2/m-TiO_2/$MAPbI_3$:PbS QDs/Spiro-OMeTAD/Au	18.60 16.30 (pure)	1.03 1.02	23.50 21.90	0.77 0.73	Improve crystallinity and enhance carrier mobility of perovskite films	[152]
PbS (~3.5 nm)	Hot-injection process	ITO/c-TiO_2/m-TiO_2/$MAPbI_3$:PbS QDs/Spiro-OMeTAD/Au	18.22 15.20 (pure)	1.08 1.03	22.50 19.20	0.75 0.76	Improve morphological, crystalline and optical properties of perovskites	[151]
PbS (4.7 ± 1.5 nm)	Hot-injection process	FTO/SnO_2/$FAPbI_3$:PbS QDs /Spiro-OMeTAD/Au	18.00 16.15 (pure)	1.06 1.02	21.80 22.30	0.75 0.71	Promote perovskite growth at low temperature, and enhance long-term stability of PSCs	[150]
SnS (3–4 nm)	Hot-injection process	ITO/c-TiO_2/$MAPbI_3$:SnS QDs/Spiro-OMeTAD/Au	16.80 13.4 (pure)	1.04 1.01	22.70 20.80	0.72 0.64	Improve crystallinity, carrier transport and light absorption of perovskites	[153]
FeOOH (~3 nm)	Room temperature chemical reaction	ITO/c-TiO_2/m-TiO_2/$Cs_{0.05}FA_{0.81}MA_{0.0.14}PbBr_{0.45}I_{2.55}$/Spiro-OMeTAD/Au	21.00 19.10 (pure)	1.17 1.08	23.12 22.84	0.78 0.78	Improve crystallization and reduce trap state of perovskites, and enhance long-term, light and thermal stability of PSCs	[77]
Black phosphorus (22.4 ± 2.4 nm)	Ultrasonic liquid exfoliation	ITO/PTAA/ $MAPbI_3$/PCBM/BCP/Ag	20.00 17.70 (pure)	1.10 1.08	21.90 21.20	0.83 0.78	Improve crystallinity and passivate surface defects of perovskites, and enhance thermal stability of PSCs	[154]
Black phosphorus (3–5 nm)	Ultrasonic liquid exfoliation	ITO/SnO_2/ $CsPbI_2Br$:Black phosphorus QDs/Spiro-OMeTAD/Au	15.47 9.26 (pure)	1.25 1.07	15.86 13.23	0.78 0.64	Promote crystalline growth and increase carrier transport of perovskites, and enhance moisture stability of PSCs	[74]
Graphene (<20 nm)	Hydrothermal reaction	FTO/c-TiO_2/$MAPbI_3$:Graphene QDs/ Spiro-OMeTAD/Au	18.34 16.83 (pure)	1.04 1.02	22.58 21.81	0.75 0.75	Passivate grain boundaries and improve electron extraction of perovskites	[157]
Graphene (<3 nm)	Chemical bath reaction	FTO/c-TiO_2/$MAPbI_3$:Graphene QDs/ Spiro-OMeTAD/Au	19.70 17.90 (pure)	1.14 1.09	24.17 23.47	0.72 0.70	Improve crystallization, reduce surface defects, and enhance electron transport of perovskites	[78]
Graphite N-doped graphene (1.5–5.5 nm)	Hydrothermal reaction	FTO/NiO/$MAPbI_3$:Graphite N-doped Graphene QDs/ PCBM/ BCP/Ag	19.80 17.1 (pure)	1.06 1.01	23.40 22.70	0.80 0.75	Passivate trap states and match energy band structure of perovskites, and enhance moisture stability of PSCs	[156]
F-doped graphene (2–8 nm)	Ultrasonic liquid exfoliation	PEN/ITO/SnO_2/$Rb_{0.05}Cs_{0.05}(FA_{0.83}MA_{0.17})_{0.90}Pb(I_{0.95}Br_{0.05})_3$:F-doped Graphene QDs/Spiro-OMeTAD/Ag	20.40 18.83 (pure)	1.11 1.07	22.87 23.03	0.81 0.76	Passivate grain boundaries and improve carrier mobility of perovskites, and enhance thermal stability of PSCs	[155]
Carbon (3–5 nm)	Solvothermal reaction	ITO/c-TiO_2/m-TiO_2/ $MAPbI_3$:Carbon QDs/Spiro-OMeTAD/Ag	18.81 16.31 (pure)	1.13 1.08	22.19 22.00	0.75 0.69	Passivate grain boundaries and improve carrier mobility of perovskites, and enhance moisture stability of PSCs	[162]
Carbon (1.62–7.36 nm)	Chemical bath reaction	ITO/NiO/$MAPbI_3$:carbon QDs/PCBM/ BCP/Ag	18.24 15.67 (pure)	1.07 1.04	21.68 19.71	0.78 0.77	Passivate grain boundaries and improve carrier mobility of perovskites, and enhance moisture stability of PSCs	[161]

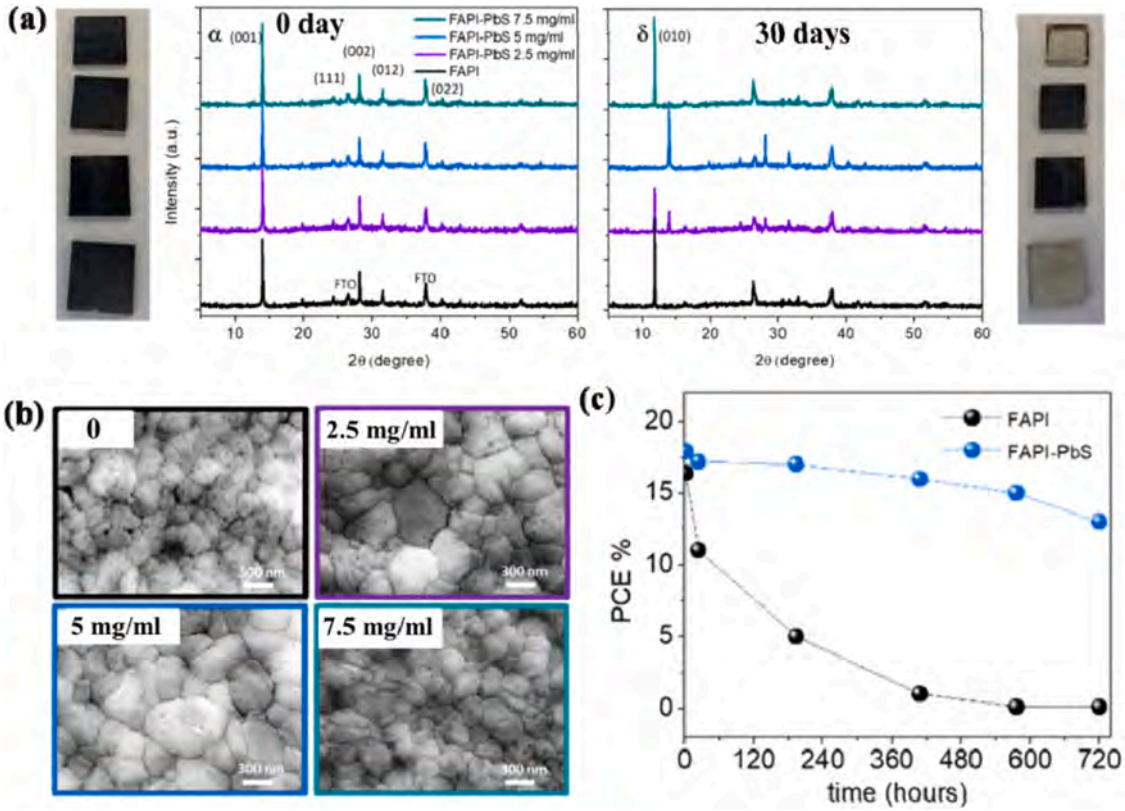

Fig. 12. (a) Photographs and XRD patterns, and (b) SEM images of perovskite films prepared with/without PbS QDs. (c) Stability of the PSCs with/without PbS QDs [150]. Printed with permission from American Chemical Society.

QDs can be tuned from 3.4 nm to 12.5 nm. Notably, the cubic phase is stable at ambient conditions for months after the ligand exchange treatment with methyl acetate. To prepare absorbers for PSCs, the pristine cubic $CsPbI_3$ QDs can be dissolved in octane and then spin-coated onto TiO_2-based FTO substrates. The samples are then post-treated by immersion into saturated methyl acetate-containing lead salts (e.g., lead acetate or lead nitrate) which have been shown to preserve the structural integrity of QDs. This post-treatment has been found to improve surface passivation and reduce dissolution of Pb atoms from $CsPbI_3$ during the subsequent rinse with methyl acetate to remove the long-chain ligands [56,132]. The resulting PSCs exhibited a champion PCE of 10.77% (Fig. 8b), which was found to be stable over 60 days in ambient atmosphere (relative humidity: 15–25%) [96]. The PCE of this device was improved to 13.43% by additionally post-treating the perovskite QD films in an ethyl acetate solution containing different salts (e.g., FAI, FABr, MAI, MABr, and CsI, Fig. 8c). The FAI-coated $CsPbI_3$ QDs display the best electronic coupling properties with increased carrier mobility from 0.23 $cm^2\ V^{-1}\ s^{-1}$ to 0.5 $cm^2\ V^{-1}\ s^{-1}$. It is proposed that the existence of FAI may bind with the $CsPbI_3$ QDs, fill the surface void sites, form $FAPbI_3$ shells and even emerge alloyed $Cs_xFA_{1-x}PbI_3$ QDs [129]. Saturated ethyl acetate solutions without FAI but containing different inorganic cesium salts (i.e., CsAc (cesium acetate), CsI, $CsCO_3$ and $CsNO_3$) were then used to passivate the surface of $CsPbI_3$ QDs (which were synthesized via a similar method to that described above). The cesium salts were observed to fill surface vacancies and reduce charge traps, thereby enhancing electronic coupling among $CsPbI_3$ QDs and increasing carrier mobility. A maximum PCE of 14.10% was obtained for the CsAc-passivated $CsPbI_3$ PSCs [135]. A mixture of OA/OLA (18 carbon atoms) and octanoic acid/octylamine (8 carbon atoms) was employed as capping ligands to fabricate cubic $CsPbI_3$ QDs [134]. It was found that a mixture of short and long chain ligands can strengthen the adsorption energy between ligands and QDs, reducing surface defects and increasing the stability of $CsPbI_3$ QDs. PSCs based on these mixed ligand $CsPbI_3$ QDs showed a PCE of 11.87% [134]. In another study, micrometer-sized graphene nanosheets were employed to crosslink and stabilize $CsPbI_3$ QDs by their surface groups (e.g., hydroxyl, carbonyl and carboxyl). The crosslinked structures also facilitated carrier transport, which resulted in PSCs with enhanced efficiency and moisture stability [66]. In addition, $CsPbI_3$ QDs were doped with ytterbium by adding ytterbium acetate during the hot-injection process (Fig. 9a). The Yb dopant was found to occupy surface defects (e.g., Pb^{2+}, Cs^+ and I^- vacancies) and enhance crystallinity, charge transport, and thermal stability of $CsPbI_3$ QDs (Fig. 9b and c). An optimized cell efficiency of 13.12% (vs. 12.06% for unmodified PSCs) was achieved for a device based on 20 mol% Yb-doped $CsPbI_3$ QDs [137]. Furthermore, GeI_2 was introduced into the hot-injection precursor to adjust the crystallization of $CsPbI_3$ QDs [136]. The addition of GeI_2 resulted in the formation of high-quality $CsPbI_3$ QDs by supplying extra I^- ions. Note that the Ge^{2+} ions were not inserted into the crystal lattice of $CsPbI_3$ QDs. These modified QDs exhibited a near-unity photoluminescence quantum yield (PLQY) of about 100%, which maintained 99% even after a month of storage. PSCs made with these QDs showed a PCE over 12% and considerable stability with 85% of the initial performance after 3 months in dry air.

Other organic/inorganic halide perovskite QDs, including $CsSn_{1-x}Pb_xI_3$ [128], $CsPbBr_3$ [94,133],$CsPbBr_{3-x}I_x$ [130], $Cs_{1-x}FA_xPbI_3$ [56,57], $MASnBr_{3-x}I_x$ [131], $FAPbI_3$ [55], and $FA_{1-x}Cs_xPb(I_{1-x}Br_x)_3$ [138], have been fabricated through similar hot injection methods for applications in PSCs. $CsPbI_3$ and $FAPbI_3$ QDs have both been reported to be sensitive to humidity and polar solvents. Conversely, mixed-cation $Cs_{1-x}FA_xPbI_3$ QDs have been demonstrated to be more stable in ambient air due to entropic stabilization from the combination of Cs and FA cations [56,57]. $Cs_{1-x}FA_xPbI_3$ QDs were prepared by a facile cation exchange process (Fig. 10a) in which hot-injection

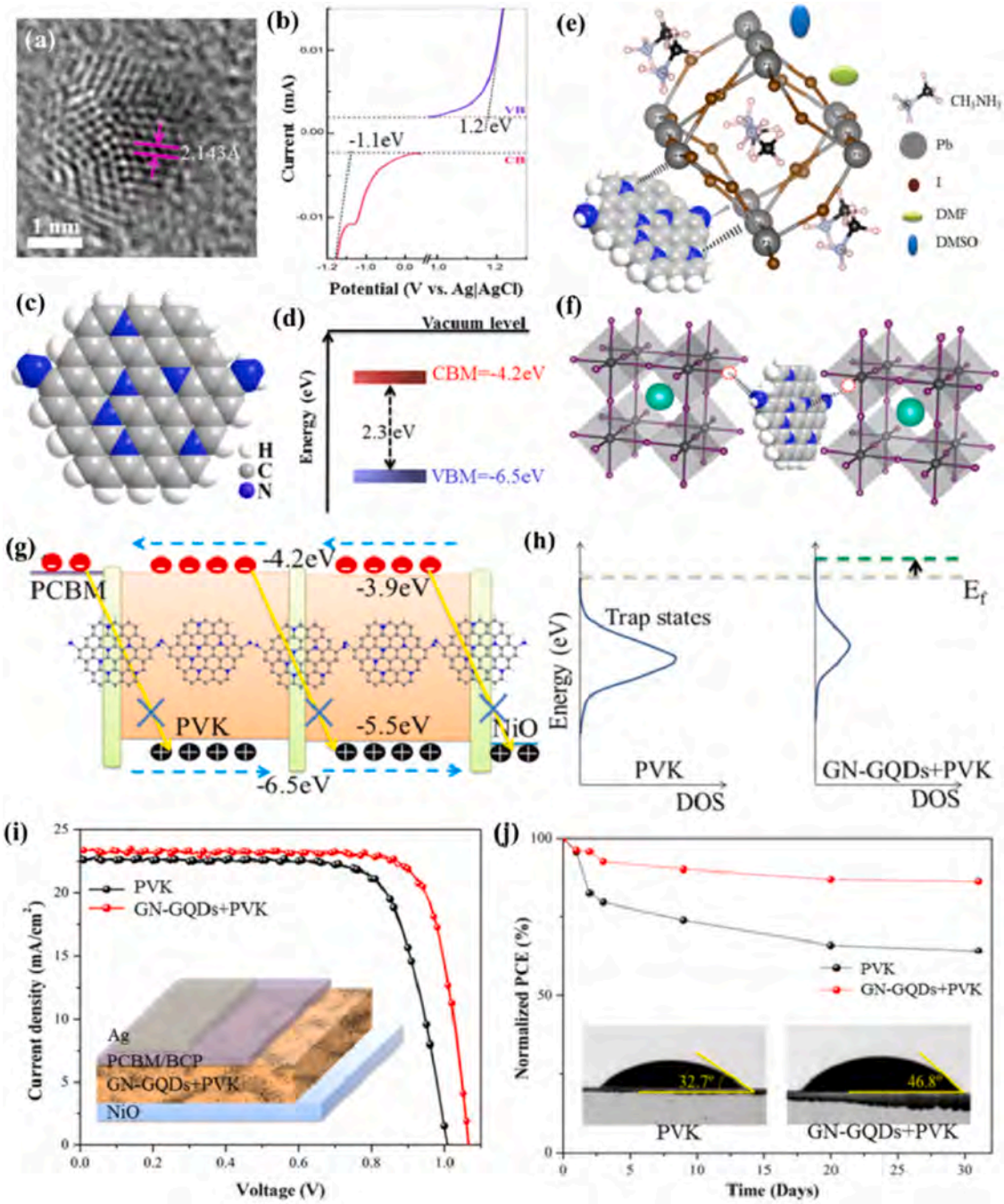

Fig. 13. (a) TEM image, (b) linear potential scans for the valance band (VB) and conduction band (CB) position, (c) structure model, and (d) energy level structure of the graphite N-doped graphene QDs (GN-GQDs). Schematic diagrams of (e) the interaction between GN-GQDs and Pb ions in perovskites, (f) the passivation of vacant I sites in perovskites by the GN-GQDs, (g) charge transport and (h) energy level structure of the PSCs modified with the GN-GQDs. (i) J-V curves and stability of the PSCs with/without the GN-GQDs [156]. Printed with permission from American Chemical Society.

synthesized $CsPbI_3$ and $FAPbI_3$ QDs were mixed in different molar ratios and heated to different temperatures (<90 °C). A variety of compositions of stable $Cs_{1-x}FA_xPbI_3$ QDs were achieved (Fig. 10b and c), and it was found that PSCs based on the $Cs_{0.75}FA_{0.25}PbI_3$ QDs exhibited the best PCE of 11.14%. This sample displayed reduced photocurrent hysteresis and lower PCE than PSCs based on $CsPbI_3$ QDs (13.47%) (Fig. 10d) [57]. $Cs_{1-x}FA_xPbI_3$ QDs were also synthesized via a similar method and the OA ligand environment was carefully optimized for high-quality perovskite QDs [56]. A certified record PCE of 16.60% was achieved for the $Cs_{0.5}FA_{0.5}PbI_3$ QD-based PSCs with negligible hysteresis, considerable photostability and long-term stability [56].

In an effort to reduce the toxicity of perovskite materials, research interest into lead-free perovskites has recently garnered significant attention. Specifically, the partial or complete replacement of Pb with Sn in perovskites has been extensively investigated

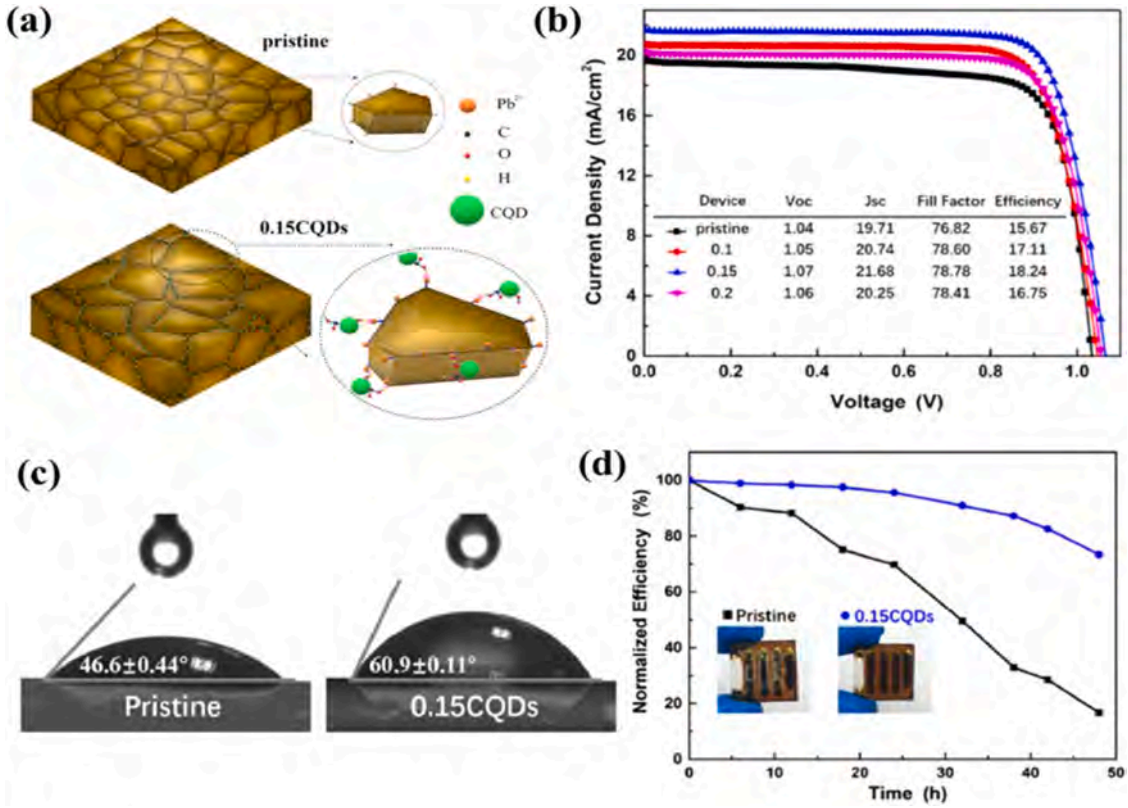

Fig. 14. (a) Schematic diagram of the passivation effect of carbon QDs in perovskite films. (b) J-V curves of the PSCs with/without carbon QDs. (c) Contact angle of water for perovskite films with/without carbon QDs, and (d) stability of the PSCs with/without carbon QDs [161]. Printed with permission from American Chemical Society.

[147]. Unfortunately, at ambient conditions Sn^{2+} ions are easily oxidized into Sn^{4+} which has been found to lead to irreversible conversion of the desired black perovskite phase (e.g., cubic or tetragonal phase) into the undesired yellow phase (e.g., orthorhombic phase) [30,33]. Thus, alloyed $CsSn_{1-x}Pb_xI_3$ QDs were prepared by the hot-injection method with different SnI_2/PbI_2 ratios. It was found that the $CsSn_{1-x}Pb_xI_3$ QDs were stable for months when stored in inert gas or ambient air (Fig. 11a–c). This finding suggests that the alloying strategy can effectively enhance the oxidation stability of Sn^{2+} ions in perovskites, which is probably due to the higher binding energy for Sn^{2+} in the alloyed perovskite as compared to that in the $CsSnI_3$ QDs. However, the corresponding PSCs demonstrated poor charge transport and low PCE (0.1%), which were attributed to the long-chain ligands on the QD surface [128]. $CsSnI_3$ QDs were crafted via a low-temperature solution process by employing triphenyl phosphite as an anti-oxidant agent in the perovskite precursor (Fig. 11d). It was proposed that the formation of $CsSnI_3$ QDs could be divided into two steps: first, the formation of SnI_2 QDs in the presence of triphenyl phosphite; and second, the formation of $CsSnI_3$ QDs via the reaction between SnI_2 QDs and Cs^+/I^- ions. Since triphenyl phosphite effectively captured oxygen and then hindered the conversion of Sn^{2+} to Sn^{4+}, the $CsSnI_3$ QDs exhibited considerable stability for months. PSCs based on these $CsSnI_3$ QDs possessed a best PCE of 5.03% and an average PCE of 4.13% and displayed long-term stability [139].

Quantum dots as additives in perovskite films

Generally, perovskite films composed of polycrystalline grains are fabricated by solution processes (e.g., one- and two-step spin coating methods) and then annealed at a relatively low temperature (~100 °C) [148]. While simple and effective, this technique also results in unavoidable surface defects and grain boundary trap states in the perovskite films, which consequently result in significant carrier recombination in the PSCs [148]. Moreover, these surface defects and trap states have also been found to cause infiltration of moisture and oxygen into films, which decompose the perovskite crystals and eventually lead to poor stability of the PSCs. In addition, unsaturated or un-coordinated Pb ions from incomplete crystallization usually exist in the perovskite films, which have been shown to produce ionic migration and photocurrent hysteresis of PSCs [77]. Long-term, high-temperature, and continuous illumination have also been found to cause decomposition, loss of FA or MA cations, and migration of halide ions which result in the generation of vacancies and interstitial ions that act as carrier trap sites in PSCs [15,149]. Hence, the fabrication of high-quality perovskite films with reduced surface defects and grain boundary trap states is highly imperative for high-performance PSCs. In this regard, as indicated in Table 4, a variety of QD materials, such as PbS [150–152], SnS [153], FeOOH [77], black phosphorous [74,154], graphene [78,155–157], and carbon QDs [158–162], have been employed as multifunctional additives to promote perovskite films with improved morphological, optical and electronic properties for high efficiency and stable PSCs.

Metal sulfide QDs have been extensively applied in many photoelectric fields, due primarily to their size-dependent tunable band gaps, facile synthesis, large dipole moment, high extinction coefficient, and ability to generate multiple excitons [163,164]. Among them, PbS QDs, which absorb light in the infrared range and possess a large exciton Bohr radius of 18 nm, have received significant

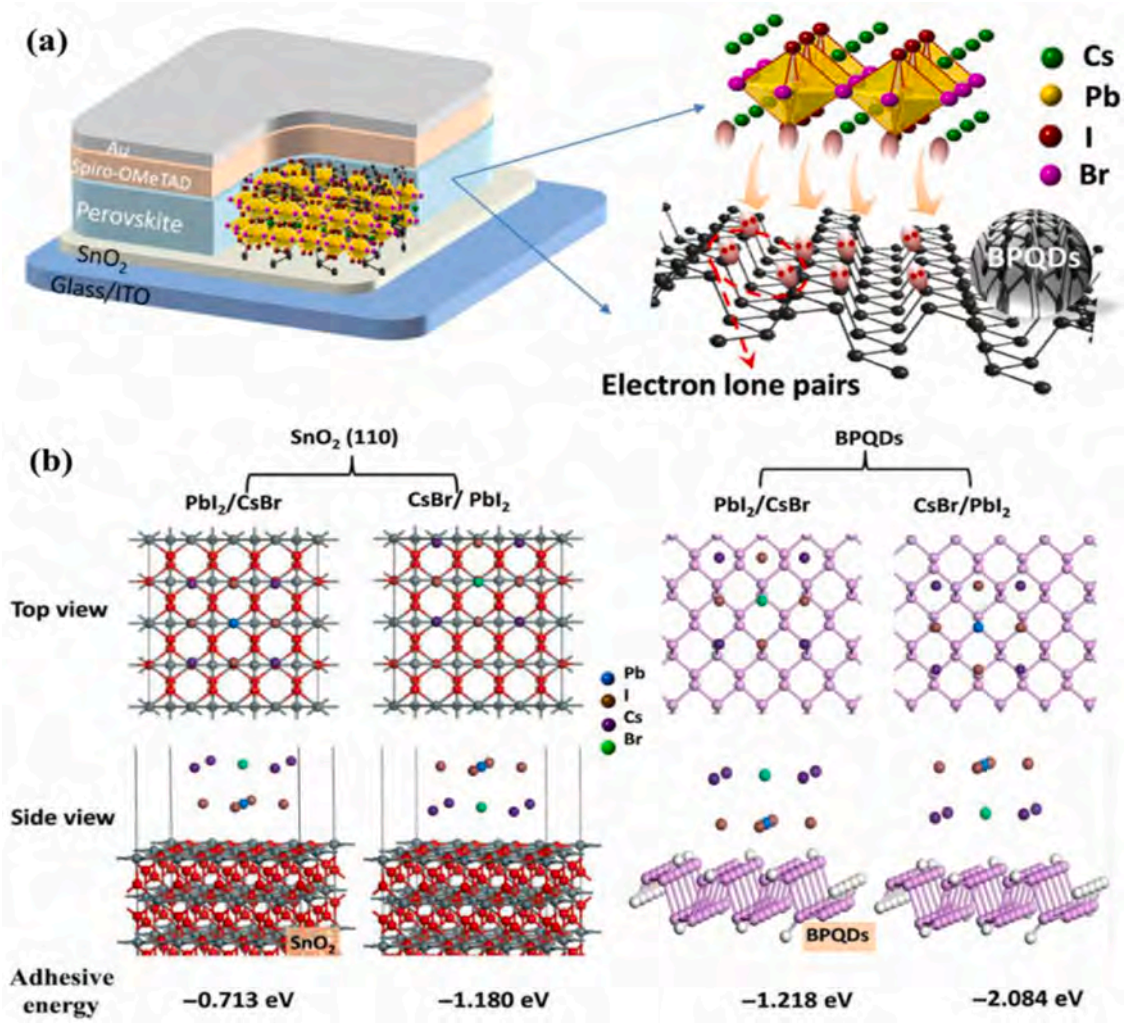

Fig. 15. (a) Schematic diagram of the PSCs based on the black phosphorous QDs (BPQDs) modified $CsPbI_2Br$ film. (b) Adhesive energy values of the perovskite precursor on SnO_2 and BPQDs calculated by the density functional theory method [74]. Printed with permission from Science Publishing Group.

attention and achieved PCEs over 10% when used as light harvesters in QD solar cells [163,165]. Notably, the crystal lattice of PbS QDs matches well with that of perovskite QDs, both including a six-coordinated Pb atom and similar Pb-Pb distances (e.g., PbS = 5.97 Å vs. $MAPbI_3$ = 6.26 Å) [152]. Initially, halide perovskites were rationally coated on the surface of PbS QDs to modify the morphology and charge transport dynamics of PbS QDs and thus improve the device efficiency and stability of PbS QD-based solar cells [42,163,166,167]. When added into perovskite precursor solution, PbS QDs have been found to act as nucleation centers which yield larger perovskite grains and reduced trap states (Fig. 12a and b), which result in high-performance and stable PSCs (Fig. 12c) [150–152]. Similarly, SnS QDs were embedded into $MAPbI_3$ layers to improve their crystallinity and carrier separation/transfer rate. Furthermore, the addition of low bandgap SnS QDs (~1.3 eV) was found to increase light harvesting of perovskite films in the visible and NIR light range [153].

Graphene and carbon QDs have also played significant roles as functional additives to effectively ameliorate the crystallization of perovskites and passivate surface defects and grain boundary trap states in perovskite films. These improvements have been principally attributed to the substantial chemical bonding between the hydroxyl, carboxyl and carbonyl groups on the surface of graphene/carbon QDs and the un-coordinated Pb ions of perovskites. Moreover, the hydrophobic features of graphene and carbon QDs have been shown to endow perovskite films with superior moisture stability [78,155–157,161,162]. Notably, graphene QDs modified with a doping treatment (e.g., nitrogen, sulfur or fluorine doping) have been demonstrated to possess adjustable energy structures and more active sites [155,156]. Recently, graphene QDs were doped by substituting some C atoms with N atoms (Graphite N-doped graphene QDs, Fig. 13a–d). These doped QDs showed a strong interaction with un-coordinated Pb^{2+} ions and I^- vacancies (Fig. 13e and f), which alleviated electron trap density in perovskites. The Graphite N-doped graphene QDs also demonstrated a high carrier mobility due to the π-conjugated carbon rings and well-matched energy band alignment owing to the slight rise of Fermi energy level for the passivated perovskite (Fig. 13g and h). PSCs made with Graphite N-doped graphene QDs presented superior cell efficiency and long-term stability (Fig. 13i and j) [156]. Additionally, fluorine atoms were also doped into graphene QDs, which converted the hybridization state of the carbon atoms from sp^2 to sp^3. The presence of highly

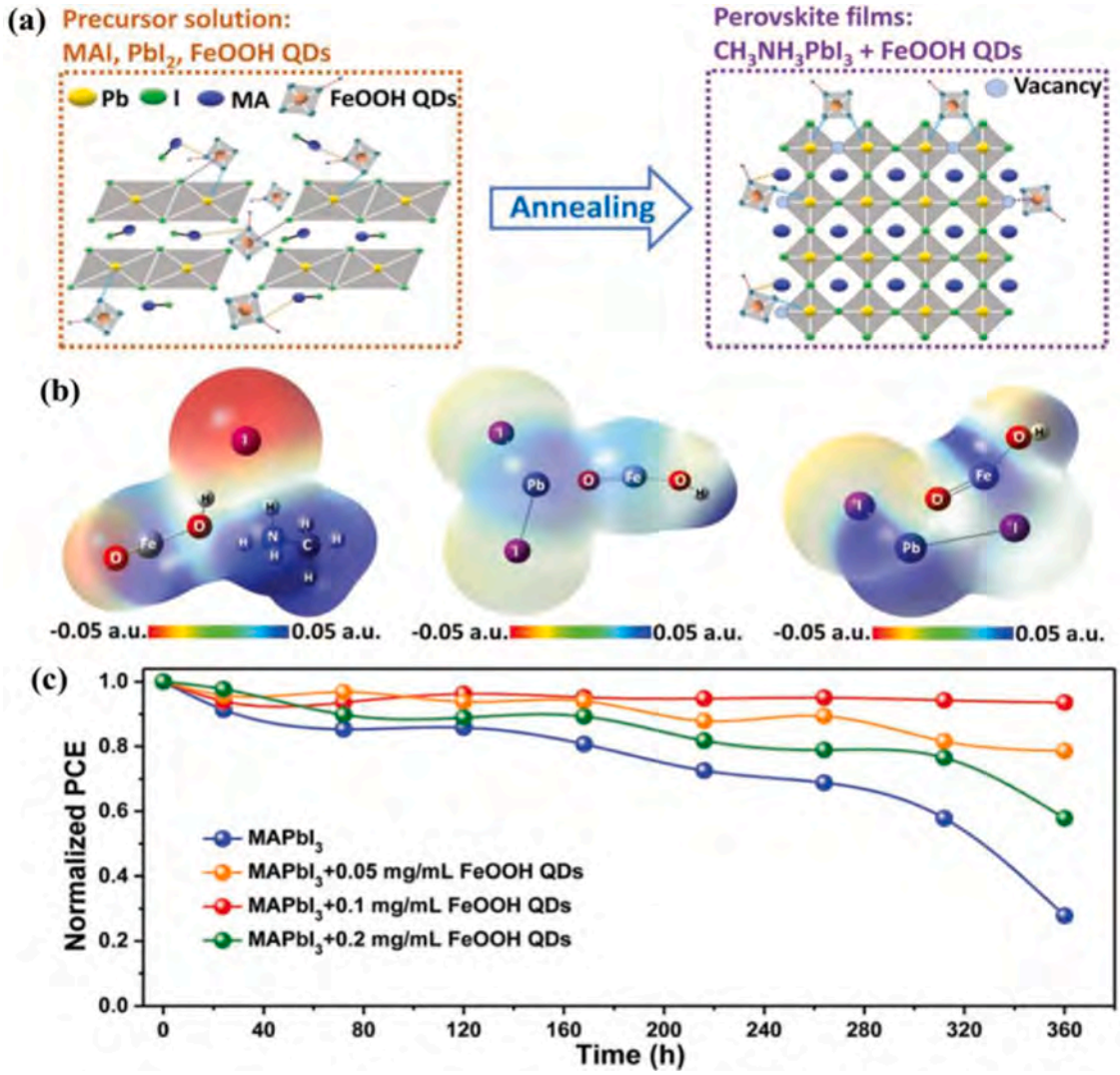

Fig. 16. Schematic illustration of (a) the growth process of perovskites passivated with FeOOH QDs and (b) the electrostatic potential surface of MAI-FeOOH and PbI_2-FeOOH. (c) Thermal stability of the PSCs with/without FeOOH QDs at 85 °C for 360 h [77]. Printed with permission from Wiley-VCH.

electronegative fluorine atoms was found to promote a robust interaction between the graphene QDs and the ions in the perovskites which decreased crystal defects. The strong C—F bonds were found to protect the perovskite films from decomposition due to their inert and hydrophobic nature. Thus, a maximum PCE over 20% (vs. 18.83% for unmodified PSCs) was obtained for the resulting flexible PSCs, with 85% retention after continuous heating conditions (85 °C) in a N_2 atmosphere for 600 h [155]. Similarly, the functional carboxylic, hydroxyl and amino groups on the edge of carbon QDs were found to lower carrier trap density and strengthen the optoelectronic properties of the perovskite films for high-performance PSCs by interacting with un-coordinated Pb^{2+} ions (Fig. 14) [161,162].

Black phosphorus QDs can also be integrated into perovskite films for improved photovoltaic performance [74,154]. For example, the incorporation of black phosphorus QDs into perovskite precursors can facilitate nucleation and crystalline growth of $CsPbI_2Br$ with reduced trap density and enhanced carrier transport dynamics [74]. The improved electrical properties were ascribed to the strong electronic interaction between the lone-pair electrons of black phosphorus and the Cs cations of $CsPbI_2Br$ (Fig. 15a). Density functional theory (DFT) calculations indicated that the adhesive energy of perovskite precursor on black phosphorous QDs was significantly lower than on pure SnO_2 ETL (Fig. 15b). The lower adhesive energy represents a lower energy barrier to the growth of perovskite crystals with better chemical stability. Black phosphorous (0.7 wt %)-doped PSCs displayed a best PCE of 15.47% (vs. 9.26% for unmodified PSCs) and enhanced long-term moisture stability [74].

The iron, oxygen and hydroxyl components of FeOOH QDs have been observed to interact strongly with un-coordinated Pb, FA, MA and halide ions in perovskites (Fig. 16a). These interactions have been found to passivate surface defects and retard the ionic migration in perovskite films. The interaction energies of PbI_2-FeOOH and MAI-FeOOH were evaluated by DFT (Fig. 16b), and the calculations suggested that FeOOH QDs had robust interaction with MA^+ and I^- ions. PSCs made with FeOOH QDs displayed increased carrier mobility and enhanced electron extraction, which contributed to an

Table 5
Summary of some representative QDs as HTLs in PSCs.

QDs (diameter)	Synthesis method	Cell structure	Cell performance				Device stability	Ref.
			η (%)	V_{OC} (V)	J_{SC} (mA cm^{-2})	*FF*		
PbS (~3 nm)	Hot-injection process	ITO/PbS QDs/ $MAPbI_3$/PCBM/Al	7.50	0.86	12.10	0.72	–	[63]
PbS (~3.6 nm)	Hot-injection process	FTO/c-TiO_2/m-TiO_2/$MAPbI_3$/PbS QDs/Au	7.88	0.87	18.69	0.49	Keep 92% of the initial PCE under dry air at 25 °C for 4 days	[171]
$CuInS_2$@ZnS (~4 nm)	Hot-injection process	FTO/c-TiO_2/m-TiO_2/$MAPbI_3$/$CuInS_2$@ZnS QDs/Au	8.38 13.90 (Spiro-OMeTAD)	0.92 1.02	18.60 19.70	0.49 0.69	–	[61]
$CuInSe_2$ (~4 nm)	Hot-injection process	ITO/SnO_2/$FA_{0.8}MA_{0.2}PbI_{0.84}Br_{0.08}Cl_{0.08}$/CuInS2$_2$ QDs/Au	12.80 15.60 (Spiro-OMeTAD)	0.86 1.02	22.50 23.40	0.66 0.65	Retain 78% (vs. 30% for Spiro-OMeTAD) of the original PCE after 96 h in air	[177]
$CuIn_{1.5}Se_3$ (~4 nm)	Hot-injection process	ITO/SnO_2/$MAPbBr_3$/ $CuIn_{1.5}Se_3$ QDs/ Au	13.07	0.97	20.42	0.66	Show PCE retention of 74.9% at humidity of 50% for 30 days	[65]
MoS_2 (4–7 nm)	Ultrasonic liquid exfoliation	FTO/c-TiO_2/m-TiO_2/$CsPbBr_3$/MoS_2 QDs/Carbon	6.80	1.31	6.55	0.79	Remain 97% of the initial PCE in humidity of 80% over 700 h	[176]
Ag-In-Ga-S (3–5 nm)	Hot-injection process	FTO/c-TiO_2/m-TiO_2/$CsPbBr_3$/ Ag-In-Ga-S QDs/Carbon	8.46	1.46	7.43	0.80	Retain 96.1% of the initial PCE over 240 h at ambient air	[172]
SnS (4–7 nm)	Hot-injection process	ITO/c-TiO_2/$(CsPbI_3)_{0.05}(FAPbI_3)_{0.79}(MAPbI_3)_{0.16}$/SnS QDs/Au	13.72	0.94	22.96	0.63	Retain 99% of the initial efficiency in air with humidity of 30–50% for 1000 h	[64]
Cu_2ZnSnS_4 (8 ± 2 nm)	Hot-injection process	FTO/c-TiO_2/m-TiO_2/$CsPbBr_3$/Cu_2ZnSnS_4 QDs/Ag	4.84 5.36 (Spiro-OMeTAD)	0.94 1.12	7.36 7.04	0.70 0.68	Keep stable over 2500 h (vs. ~ 80% for Spiro-OMeTAD for 800 h) in air	[175]
$Cu_{12}Sb_4S_{13}$ (~5.7 nm)	Hot-injection process	FTO/c-TiO_2/$MAPbI_3$/ $Cu_{12}Sb_4S_{13}$ QDs/Au	14.13 15.25 (Spiro-OMeTAD)	1.05 1.12	21.85 20.73	0.62 0.66	Retain 91% (vs. 61% for Spiro-OMeTAD) of the initial PCE after 30 days in ambient air	[174]
$Cu_{12}Sb_4S_{13}$ (5–6 nm)	Hot-injection process	FTO/c-TiO_2/m-TiO_2/$CsPbI_3$ QDs/ $Cu_{12}Sb_4S_{13}$ QDs/Au	10.02 12.14 (Spiro-OMeTAD)	1.04 1.10	18.28 17.66	0.53 0.62	Maintain 94% (vs. 42% for Spiro-OMeTAD) of the initial PCE after 360 h in ambient air	[173]
Cu_2O (8–10 nm)	Chemical bath process	FTO/c-TiO_2/m-TiO_2/$Cs_{0.05}FA_{0.81}MA_{0.14}PbI_{2.55}Br_{0.45}$/$Cu_2O$ QDs/ MoO_3/Ag	18.90 20.60 (Spiro-OMeTAD)	1.15 1.15	22.20 23.54	0.74 0.73	Retain 80% (vs. 50% for Spiro-OMeTAD) of the initial efficiency for 30 days in air (humidity ~ 30%)	[60]

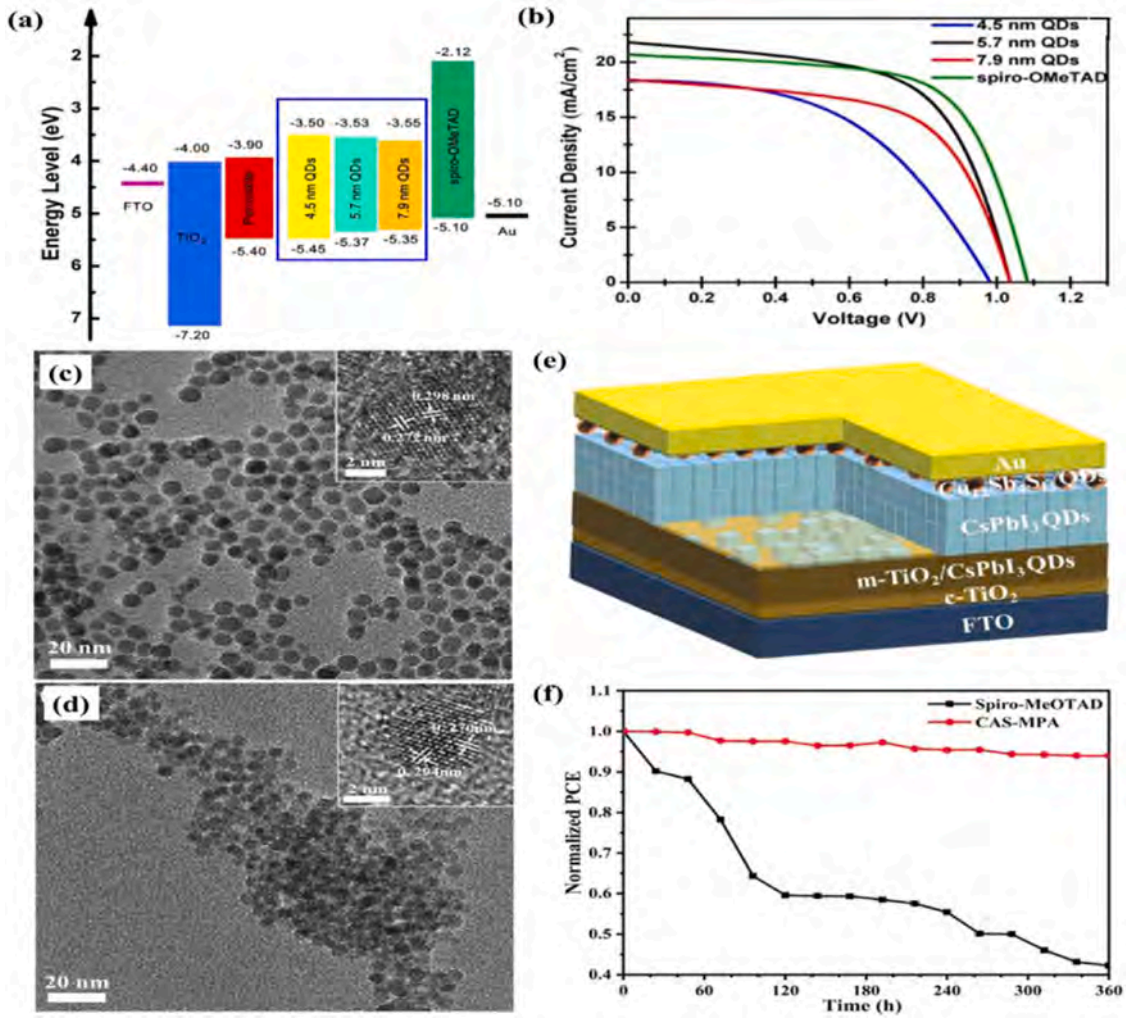

Fig. 17. (a) Schematic diagram of the energy band alignment and (b) J-V curves of PSCs using different $Cu_{12}Sb_4S_{13}$ QDs [174]. Printed with permission from The Royal Society of Chemistry. TEM images of the $Cu_{12}Sb_4S_{13}$ (CAS) QDs capped with (c) OLA and (d) 3-mercaptopropionic acid (MPA), respectively. (e) Schematic diagram of PSCs using the $Cu_{12}Sb_4S_{13}$ (CAS) QDs, and (f) stability of the devices in ambient air [173]. Printed with permission from American Chemical Society.

optimized PCE up to 21.00% (vs. 19.1% for unmodified PSCs) and considerable thermal, light, moisture and long-term stability (Fig. 16c) [77].

Quantum dots in hole transport layers

Quantum dots as hole transport materials

Organic materials including Spiro-OMeTAD, PTAA, P3HT and PEDOT:PSS are commonly used as HTLs for PSCs due to their ability to efficiently extract and transport holes. Organic HTLs do, however, suffer from some challenges, including high cost and poor stability. In this regard, several inorganic materials (e.g., NiO [168], CuSCN [169], and CuI [170]) with superior stability, low cost, and high hole mobility have been developed as HTLs for PSCs. Table 5 shows various inorganic QD materials (e.g., PbS [63,171], SnS [64], Ag-In-Ga-S [172], $CuInS_2$ [61], $Cu_{12}Sb_4S_{13}$ [173,174], Cu_2ZnSnS_4 [175], and Cu_2O [60]) that have also been employed as hole transporters for PSCs, mainly owing to their amazing characteristics, such as facile synthesis, homogeneous dispersion, adjustable energy-level alignment, good stability, and high hydrophobicity [60,61,63–65,171–178].

Because of their p-type nature, suitable valence band energy level, nontoxicity, high hole mobility, and stability, metal sulfide/oxide QDs (especially Cu-based inorganic materials like $CuInS_2$, $CuInSe_2$, $Cu_{12}Sb_4S_{13}$, Cu_2ZnSnS_4 and Cu_2O) have shown particular promise as alternative HTLs for PSCs [60,61,65,173–175,177]. For example, $Cu_{12}Sb_4S_{13}$ QDs with different diameters were synthesized to adjust the energy band structures and applied as hole deliverers in PSCs (Fig. 17a) [174]. It was found that 5.7 nm-sized $Cu_{12}Sb_4S_{13}$ QDs yielded suitable energy-level alignment for the PSCs, resulting in a maximum PCE of 14.13%, which was comparable to that (15.25%) of a Spiro-OMeTAD-based one (Fig. 17b) [174]. In addition, the native OLA ligands on $Cu_{12}Sb_4S_{13}$ QDs were replaced with bi-functional 3-mercaptopropionic acid (with carboxyl and sulfhydryl groups) via a ligand exchange (Fig. 17c and d). This ligand exchange enhanced the electronic coupling among QDs, and increased hole mobility of the $Cu_{12}Sb_4S_{13}$ QDs. However, PSCs based on these $Cu_{12}Sb_4S_{13}$ QDs (Fig. 17e) displayed lower cell efficiency than those based on Spiro-OMeTAD. The inferior performance of the $Cu_{12}Sb_4S_{13}$ HTLs was attributed to significant carrier recombination and the larger resistance. In spite of this, the $Cu_{12}Sb_4S_{13}$-based devices presented

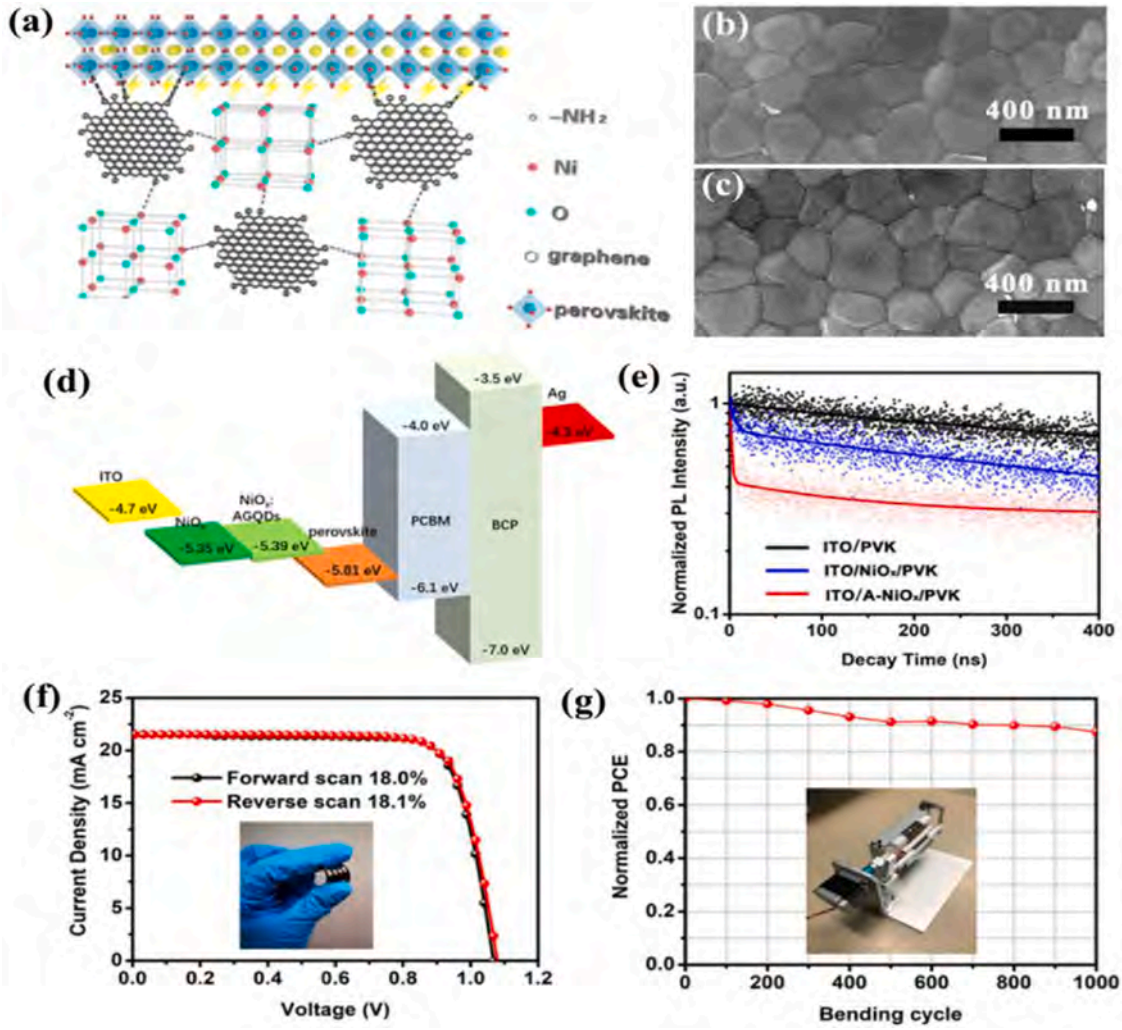

Fig. 18. (a) Schematic diagram of the interaction between perovskite and amino-functionalized graphene QDs. SEM images of perovskite films deposited on the NiO_x HTLs with (b) and without (c) graphene QDs. (d) Schematic diagram of the energy level alignment of the PSCs based on the NiO_x HTLs. (e) Time-resolved photoluminescence spectra of perovskite films deposited on different substrates. (f) J-V curves and (g) bending stability of flexible PSCs based on the modified NiO_x HTLs [73]. Printed with permission from American Chemical Society.

substantially enhanced stability when compared to devices with Spiro-OMeTAD (Fig. 17f) [173].

In another study, hydrophilic hydroxyl functionalized Cu_2O QDs were prepared by a simple low-temperature solution process. The Cu_2O QDs were then further functionalized with different silane coupling agents (i.e., 3-aminopropyltriethoxysilane, octadecyltriethoxysilane, and ethenyltriethyloxysilane) to achieve both solubility in nonpolar solvents and enhanced carrier mobility. Ethenyltriethyloxysilane was found to adequately facilitate particle dispersion in non-polar solvents and retard the decline of charge mobility in Cu_2O QDs. PSCs based on the ethenyltriethyloxysilane modified Cu_2O QDs presented a PCE of 18.90%, which was superior to that of pristine Cu_2O QD-based devices (11.90%), but was slightly lower than that of devices using Spiro-OMeTAD (20.60%). The modified Cu_2O-based device did, however, maintain 90% of its original efficiency after 1 month in ambient air, while the Spiro-OMeTAD device retained only 50% [60].

Quantum dots as additives in hole transport layers

The introduction of QDs into HTLs for PSCs is an area ripe for further investigation, with few current studies reported [67,73,179]. One promising candidate for HTL incorporation is graphdiyne, a π-conjugated carbon material that is rich with sp^2 and sp-hybridized carbons and possesses a 2D structure similar to graphene. Graphdiyne has intrinsic band gaps from 0.46 eV to 1.22 eV, uniformly distributed pores, and adjustable electronic properties, which make it attractive for photovoltaic applications [67,72,180]. Graphdiyne QDs were doped into P3HT films where were then used as HTLs for PSCs [67]. The graphdiyne QDs showed strong π-π stacking interaction with the P3HT molecules and improved their hole transport. Moreover, the porous nature of the graphdiyne QDs enhanced the long wavelength light scattering of the modified HTLs, which led to a beneficial increase in the light absorption efficiency of the PSCs. PSCs based on the planar n-i-p structure of FTO/c-TiO_2/m-TiO_2/$MAPbI_3$/modified P3HT/Au demonstrated a PCE of 14.58%, which was superior to that of a pure P3HT-based one (11.53%). The incorporation of graphdiyne QDs could also further improve the long-term stability of PSCs due to their hydrophobicity [67]. In another study, graphene QDs were functionalized with amino groups, mixed into an aqueous solution of NiO_x nanoparticles, and spin-coated to be HTLs. The presence of amino groups in the HTLs was found to strongly interact with the Pb^{2+} ions in the perovskite precursor and facilitate

Table 6
Summary of some representative QDs as interfacial modifiers between perovskite films and ETLs in PSCs.

QDs (diameter)	Synthesis method	Cell structure	Cell performance				QD effect	Ref.
			η (%)	V_{OC} (V)	J_{SC} (mA cm^{-2})	*FF*		
Graphene (5–10 nm)	Electrolysis	FTO/c-TiO_2/m-TiO_2/Graphene QDs $MAPbI_3$/Spiro-OMeTAD/Au	10.15 8.81 (pure)	0.94 0.94	17.06 15.43	0.64 0.61	Enhance the electronic coupling and electron extraction of ETLs	[182]
Graphene (7–14 nm)	Chemical oxidation reaction	FTO/c-TiO_2/Graphene QDs $MAPbI_3$/ Spiro-OMeTAD/Au	19.11 17.27 (pure)	1.12 1.11	22.47 21.20	0.76 0.73	Improve perovskite quality, facilitate electron transfer, and reduce photocurrent hysteresis of PSCs	[71]
Graphene (~5 nm)	Solvothermal reaction	FTO/c-TiO_2/m-TiO_2/Graphene QDs $CsPbBr_3$/Carbon	9.72 7.54 (pure)	1.46 1.31	8.12 7.46	0.82 0.77	Modify the energy-level alignment, reduce the interfacial energy barrier and enhance electron extraction of PSCs	[97]
Graphene (~3 nm)	Hydrothermal reaction	FTO/c-TiO_2/m-TiO_2/Graphene QDs/ $(FAPbI_3)_{1-x}(MAPbBr_3)_x$/Spiro-OMeTAD/Au	20.45 18.57 (pure)	1.08 1.06	24.92 24.00	0.76 0.73	Reduce interfacial contact resistance, and facilitate electron extraction and transport of PSCs	[190]
Graphene (–)	Hydrothermal reaction	FTO/ SnO_2/ Graphene QDs $MAPbI_3$/Spiro-OMeTAD/Au	16.54 13.61 (pure)	1.03 1.01	23.36 22.32	0.68 0.61	Optimize interfacial energy-level alignment and enhance conductivity for efficient electron transport of PSCs	[191]
Graphene (~3 nm)	Hydrothermal reaction	FTO/α-Fe_2O_3/Graphene QDs/$MAPbI_3$: Graphene QDs/ Graphene QDs/ Spiro-OMeTAD/Au	19.20 14.08 (pure)	1.03 1.00	23.50 22.62	0.79 0.65	Improve perovskite quality, increase charge extraction, optimize interfacial energy-level alignment, reduce hysteresis, and enhance long-term, light, thermal and moisture stability of PSCs	[192]
Carbon	Hydrothermal reaction	FTO/c-TiO_2/m-TiO_2/Carbon QDs/ $MAPbCl_xI_{3-x}$/Spiro-OMeTAD/Au	16.80 14.96 (pure)	1.02 1.02	22.85 21.12	0.72 0.69	Facilitate electron transport, and enhance light stability of PSCs	[98]
Graphdiyne (3–5 nm)	Solvothermal reaction	FTO/c-TiO_2/Graphdiyne QDs/$MAPbI_3$: Graphdiyne QDs/ Graphdiyne QDs/ Spiro-OMeTAD/Graphdiyne QDs/Au	19.89 17.17 (pure)	1.12 1.08	22.48 21.03	0.79 0.75	Improve perovskite quality, increase charge extraction, and enhance long-term, light, thermal and moisture stability of PSCs	[72]
Graphite carbon nitride (10–30 nm)	Solid grinding process	FTO/SnO_2/Graphite carbon nitride QDs/ $Cs_xMA_yFA_{1-x-y}PbI_zBr_{3-z}$/Spiro-OMeTAD/Au	21.23 18.42 (pure)	1.14 1.09	23.39 23.14	0.80 0.75	Improve perovskite quality, optimize interfacial energy-level alignment, and enhance long-term and illumination stability of PSCs	[196]
CdS (4–5 nm)	Successive ionic adsorption and reaction	ITO/m-TiO_2/CdS QDs/$MAPbI_3$/Spiro-OMeTAD/Au	10.51 8.97 (pure)	0.94 0.92	16.86 14.90	0.64 0.63	Improve electron life time and enhance electron extraction of PSCs	[197]
$CuInS_2$ (4–12 nm)	Solvothermal reaction	ITO/TiO_2 nanorod arrays/$CuInS_2$ QDs/$MAPbI_3$/Spiro-OMeTAD/Au	11.70 8.90 (pure)	0.98 0.92	17.60 14.90	0.69 0.65	Increase light absorption and enhance electron extraction of PSCs	[198]
CdSe (2.4–3.5 nm)	Microfluidic assisted chemical reaction	ITO/c-TiO_2/m-TiO_2/CdSe QDs/$MAPbI_3$/ Spiro-OMeTAD/Au	15.68 11.57 (pure)	1.08 1.00	20.57 18.36	0.70 0.63	Improve perovskite quality, optimize interfacial energy-level alignment, and enhance electron transport of PSCs	[194]
CdSe@ZnS (6–7 nm)	Hot-injection process	ITO/PEDOT:PSS/$MAPbI_3$/CdSe@ZnS QDs/C_{60}/BCP/Ag	19.6 16.7 (pure)	1.08 1.04	23.5 21.7	0.77 0.74	Passivate surface traps and grain boundaries of perovskites, suppress hysteresis and enhance long-term thermal stability of PSCs	[85]
$CsPbBrCl_2$ (~7 nm)	Hot-injection process	ITO/PTAA/$MAPbI_3$/$CsPbBrCl_2$ QDs/C_{60}/BCP/Cu	20.90 18.30 (pure)	1.13 1.06	23.00 23.20	0.80 0.74	Improve perovskite quality, and enhance moisture and thermal stability of PSCs	[203]
$CsPbI_3$ (~10 nm)	Hot-injection process	ITO/PTAA/$Cs_{0.05}(FA_{0.83}MA_{0.17})_{0.95}Pb(I_{0.83}Br_{0.17})_3$/$CsPbI_3$ QDs/C_{60}/ BCP/Cu	20.60 19.40 (pure)	1.15 1.10	22.90 19.40	0.78 0.79	Optimize interfacial energy-level alignment and enhance electron transport of PSCs	[83]
$CsPbBr_3$ (~18 nm)	Emulsion synthesis	ITO/PTAA/$Cs_{0.05}(FA_{0.83}MA_{0.17})_{0.95}Pb(I_{0.83}Br_{0.17})_3$/$CsPbBr_3$ QDs/C_{60}/ BCP/Cu	21.03 19.08 (pure)	1.19 1.13	22.95 22.82	0.77 0.74	Improve perovskite quality, optimize interfacial energy-level alignment and enhance electron transport of PSCs	[183]

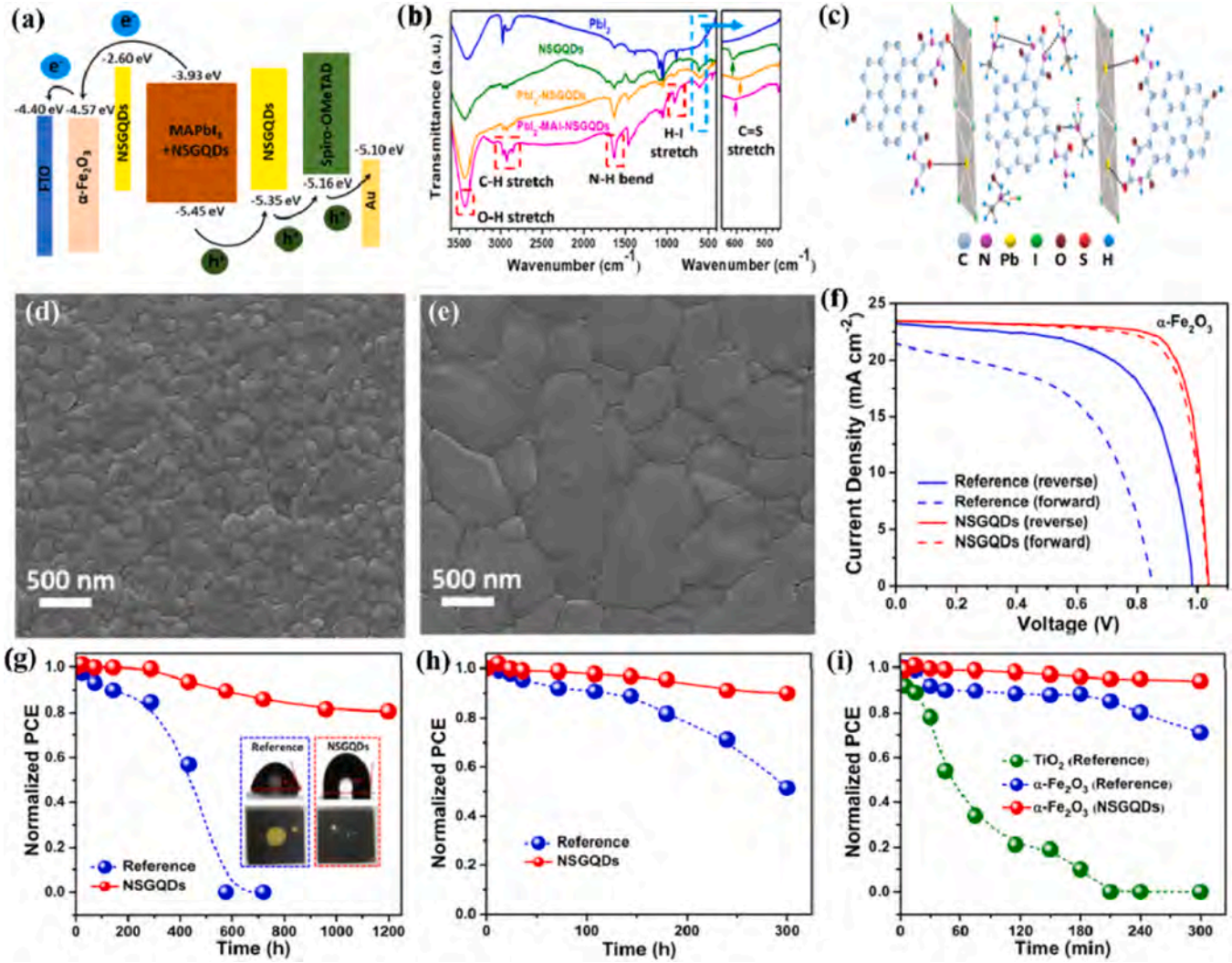

Fig. 19. (a) Schematic diagram of the energy level alignment of the PSCs modified with the N, S co-doped graphene QDs (NSGQDs). (b) Fourier Transform Infrared (FTIR) spectra of different materials. (c) Schematic illustration of the interaction between perovskite and NSGQDs. SEM images of the perovskite films (d) without and (e) with the NSGQDs, respectively. (f) J-V curves of the PSCs modified with NSGQDs under forward/reverse scans. Stability of the PSCs: (g) under air with humidity of 50 ± 10%, (h) at 85 °C with humidity of < 25%, and (i) under UV-light illumination [192]. Printed with permission from American Chemical Society.

crystallization of larger grains (Fig. 18a–c). The presence of amino coated graphene QDs was also found to change the electronic structure of NiO_x films and lead to better energy-level alignment (Fig. 18d) for more efficient hole extraction between HTLs and perovskites, yielding improved charge lifetime (Fig. 18e). PSCs made using the p-i-n device structure of ITO/modified NiO_x/$(FA_{0.83}MA_{0.17})_{0.95}Cs_{0.05}Pb(I_{0.9}Br_{0.1})_3$/PCBM/BCP/Ag showed a PCE of 19.70%, higher than that of the pristine NiO_x (17.70%). When using poly(ethylene naphthalate) (PEN)/ITO substrates to fabricate flexible PSCs based on the modified NiO HTL, it exhibited a peak PCE of 18.10% with negligible photocurrent hysteresis (Fig. 18f), excellent flexibility (Fig. 18g) and considerable long-term stability [73].

Quantum dots used in interfacial layers

Interfacial engineering has recently been developed as an effective strategy to maximize the performance of PSCs. Efficient and immediately transfer of photo-generated charge carriers from perovskite films to ETLs and HTLs is critical for photovoltaic performance. Device performance can be severely deteriorated if the free charge carriers are captured or quenched by defects or traps in the perovskites, ETLs, and HTLs. To promote advantageous charge migration, interfacial layers have been widely introduced into the interfaces between perovskite films and ETLs/HTLs, with the goal of modifying crystallization, retarding carrier recombination, and facilitating charge separation/extraction at the interfaces of PSCs. Interfacial layers can also act as isolating layers to improve the long-term, moisture, photo, and thermal stability of PSCs. Moreover, interfacial engineering can be used to reduce photocurrent hysteresis, which often originates from charge trapping, capacitive and ferroelectric polarization, or ion migration in PSCs [17,181]. Particularly, QD materials have been extensively applied as interfacial modifiers to boost PSC performance by improving perovskite film quality, passivizing surface defects and grain boundary traps, optimizing

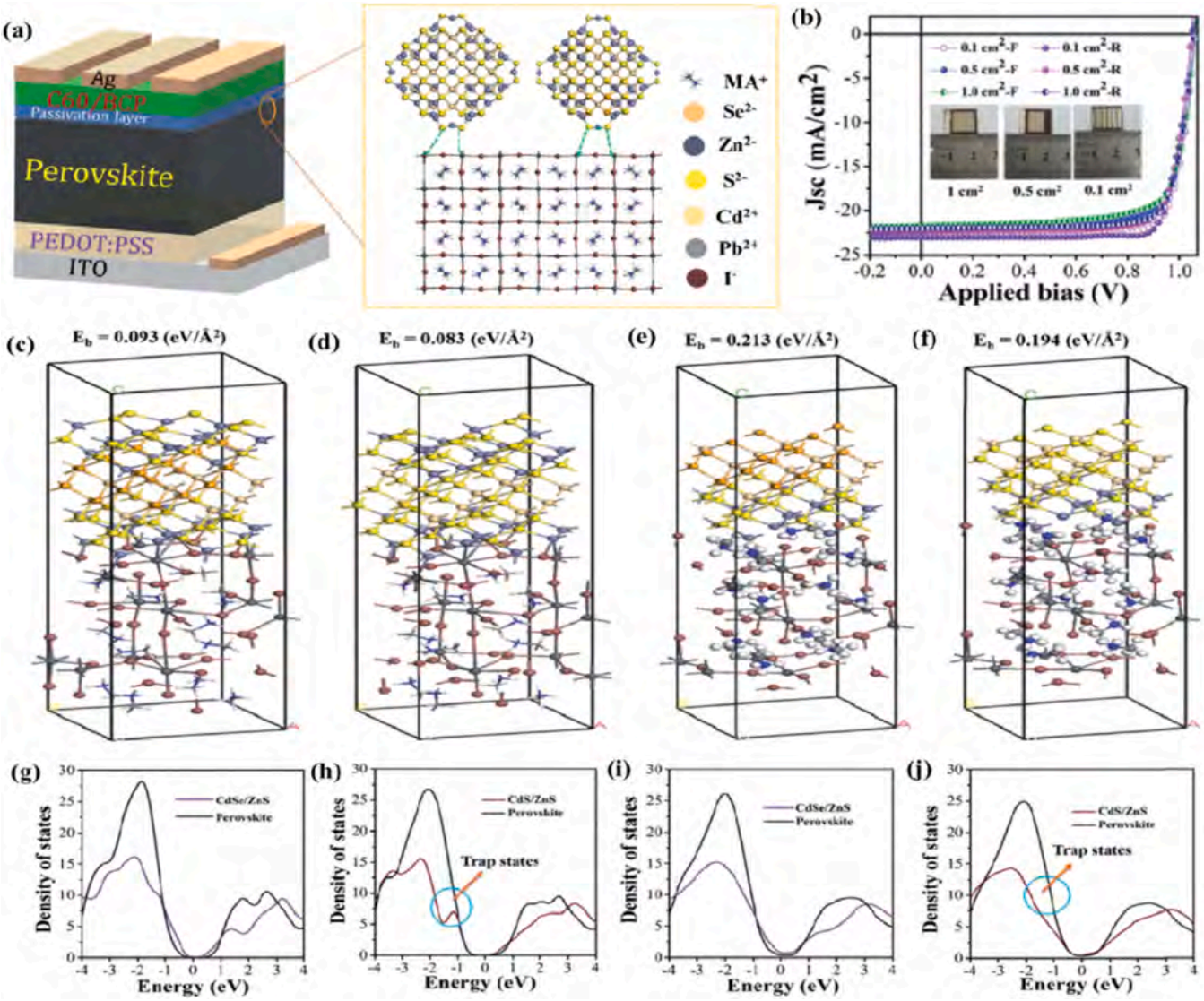

Fig. 20. (a) Schematic diagram of PSCs and the interaction between $MAPbI_3$ and CdSe@ZnS/CdS@ZnS QDs. (b) J-V curves of the PSCs modified by the CdSe@ZnS QDs with different active areas under forward and reverse scans. (c–f) Binding energies and (g–j) density of states calculated via density functional theory: (c, g) PbI_2-CdSe@ZnS, (d, h) PbI_2-CdS@ZnS, (e, i) MAI-CdSe@ZnS and (f, j) MAI-CdS@ZnS [85]. Printed with permission from The Royal Society of Chemistry.

interfacial energy-level alignment, accelerating charge extraction, alleviating photocurrent hysteresis, and strengthening device stability [75,98,165,182–189].

Quantum dots used at interfaces between electron transport layers and perovskite films

As indicated in Table 6, various QD materials have been proven to be effective interfacial modifiers between perovskite absorbers and ETLs, such as graphene [71,97,182, 187,190–192], graphdiyne [72], carbon [98,193–196], metal sulfide/selenide/oxide [85,165,167,194, 197–201], and some special halide perovskite QDs [83,183,202,203]. For example, 7, 10 and 14 nm-sized graphene QDs were applied as interfacial modifiers between TiO_2 ETLs and perovskite films [71]. The interfacial energy-level alignment in the PSCs was then optimized by tuning the bandgap of graphene by altering the size of the particles (taking advantage of quantum confinement). 10 and 14 nm-sized graphene QDs were found to enhance electron extraction because their lowest unoccupied molecular orbital (LUMO) was between that of TiO_2 and perovskite. Notably, the 7 nm-sized graphene QDs had a higher LUMO level and were detrimental to electron transfer. PSCs with 14 nm-sized graphene QDs showed the highest PCE, with reduced hysteresis and improved long-term stability [71]. In another study, N, S co-doped graphene QDs (with many functional groups, e.g., C—N, C═S, —OH, C—O, and C═O) were found to optimize PSC performance in a variety of functions (Fig. 19a and b) [192]. N, S co-doped graphene QDs were found to facilitate efficient charge extraction at the interfaces between perovskite/α-Fe_2O_3 ETLs and perovskite/Spiro-OMeTAD HTLs. Additionally, N, S co-doped graphene QDs were integrated into $MAPbI_3$ films, resulting in high-quality perovskite films with larger grains and reduced trap states (Fig. 19c–e). The resulting PSCs by using graphene interfacial modification displayed remarkably improved PCEs from 14% to 19.2%,

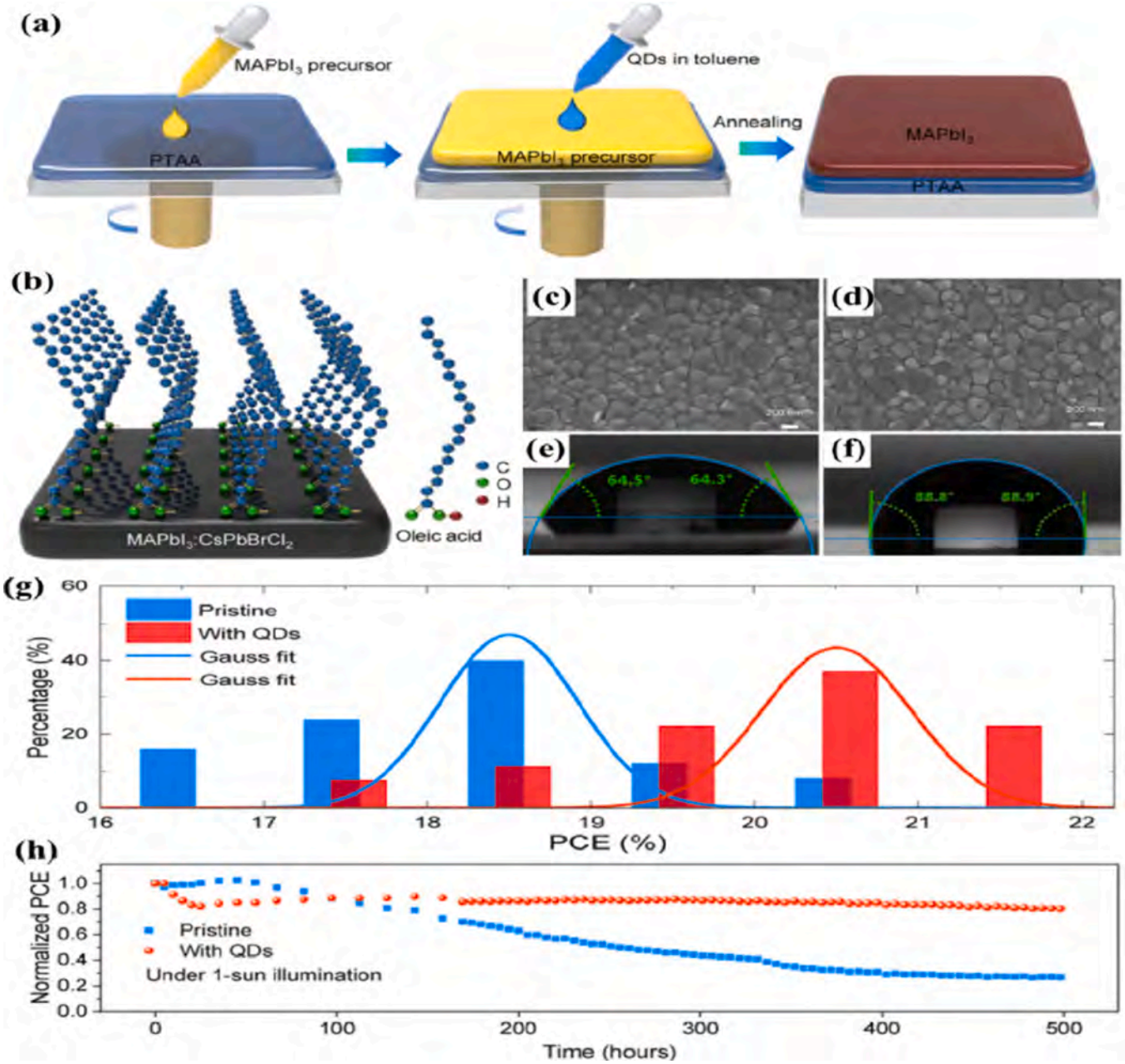

Fig. 21. Schematic diagrams of (a) the deposition of $MAPbI_3$ films via one-step spin coating process using $CsPbBrCl_2$ QDs dispersed in the toluene as anti-solvent and (b) the passivation of the OA ligands from the $CsPbBrCl_2$ QDs on the perovskite surface. (c, d) SEM images and (e, f) water contact angles of the perovskite films (c, e) without and (d, f) with the $CsPbBrCl_2$ QDs, respectively. (g) Cell efficiency distribution and (h) photostability for the PSCs with/without the $CsPbBrCl_2$ QDs [203]. Printed with permission from Elsevier.

obviously reduced hysteresis, and impressively enhanced moisture, thermal and photostability (Fig. 19f–i) [192]. Similarly, graphdiyne QDs with abundant functional groups (e.g., C=C (sp^2), C≡C (sp), C–O and C=O) and uniform pores were simultaneously incorporated into perovskite films and utilized as interfacial modifiers on TiO_2 ETLs, $MAPbI_3$ absorbers and Spiro-OMeTAD HTLs. The graphdiyne QDs provided many benefits in the resulting PSCs, including optimized energy-level alignment, increased perovskite quality, suppressed carrier traps, and enhanced moisture stability. PSCs with the graphdiyne QDs displayed a PCE increasing from 17.17% to 19.89% with negligible hysteresis and enhanced humidity, thermal and UV light stability [72].

CdSe@ZnS and CdS@ZnS QDs with core@shell structures were deposited onto the $MAPbI_3$ films to modify the perovskite layer/C_{60} ETL interface. The CdSe@ZnS and CdS@ZnS QDs were found to produce an electrostatic interaction with the perovskite and

Table 7
Summary of some representative QDs as interfacial modifiers between perovskite films and HTLs in PSCs.

QDs (diameter)	Synthesis method	Cell structure	Cell performance				QD effect	Ref.
			η (%)	V_{OC} (V)	J_{SC} (mA cm^{-2})	FF		
$MAPbBr_{3-x}I_x$ (~5 nm)	Room-temperature chemical reaction	FTO/c-TiO_2/$MAPbI_3$/$MAPbBr_{3-x}I_x$/Spiro-OMeTAD/Cr/Au	13.32 10.34 (pure)	0.95 0.94	19.51 18.09	0.72 0.61	Optimize interfacial energy-level alignment and improve hole extraction of PSCs	[184]
Mn-doped $CsPbI_3$ (15–20 nm)	Hot-injection process	FTO/c-TiO_2/$CsPbI_2Br$/Mn-doped $CsPbI_3$ QDs/PTAA /Au	14.45 13.45 (pure)	1.20 1.18	14.45 14.25	0.79 0.80	Improve light harvesting, optimize interfacial energy-level alignment and improve hole extraction of PSCs	[186]
$CsPbI_3$ (9–13 nm)	Hot-injection process	FTO/c-TiO_2/m-TiO_2/$FAMAPbI_3$/$CsPbI_3$ QDs/Spiro-OMeTAD/Au	18.56 15.17 (pure)	1.09 1.05	24.42 20.94	0.70 0.69	Optimize interfacial energy-level alignment, improve hole extraction and enhance long-term and moisture stability of PSCs	[87]
$CsSnBr_{3-x}I_x$ (1.7–3.8 nm)	Hot-injection process	FTO/c-TiO_2/m-TiO_2/$CsPbBr_3$/$CsSnBr_2I$ QDs/Carbon	9.13 5.49 (pure)	1.39 1.25	8.70 6.90	0.76 0.64	Optimize interfacial energy-level alignment, improve hole extraction and enhance long-term, thermal and moisture stability of PSCs	[206]
$CsPbI_2Br$ (10–15 nm)	Hot-injection process	FTO/c-TiO_2/$CsPbI_2Br$/$CsPbI_2Br$ QDs/PTAA /Au	14.12 13.23 (pure)	1.22 1.20	14.51 14.48	0.80 0.76	Optimize interfacial energy-level alignment and improve hole extraction of PSCs	[189]
$CsPbBr_{1.85}I_{1.15}$ (~10 nm)	Hot-injection process	FTO/c-TiO_2/m-TiO_2/$Cs_{0.05}(FA_{0.85}MA_{0.15})_{0.95}Pb(I_{0.85}Br_{0.15})_3$/ $CsPbBr_{1.85}I_{1.15}$QDs/Spiro-OMeTAD/Au	21.14 19.51 (pure)	1.14 1.09	23.42 23.37	0.79 0.76	Optimize interfacial energy-level alignment, improve hole extraction and enhance long-term, moisture and light stability of PSCs	[205]
$Cs_{0.57}FA_{0.43}PbI_3$ (10.7 ± 2.3 nm)	Hot-injection process + cation exchange reaction	FTO/SnO_2/$FAPbI_3$/$Cs_{0.57}FA_{0.43}PbI_3$ QDs/Spiro-OMeTAD/Au	20.82 19.95 (pure)	1.12 1.12	24.44 24.20	0.76 0.74	Optimize interfacial energy-level alignment, improve hole extraction and enhance long-term and moisture stability of PSCs	[86]
$CsPbBr_3$ (~7.5 nm)	Hot-injection process	ITO/SnO_2/$MAPbI_3$/$CsPbBr_3$ QDs/Spiro-OMeTAD/Au	20.17 18.20 (pure)	1.11 1.08	23.57 23.01	0.77 0.73	Improve perovskite quality, and enhance carrier transport	[204]
$CuInS_2$@ZnS (5.6–6.4 nm)	Hot-injection process	FTO/c-TiO_2/m-TiO_2/$CsPbBr_3$/$CuInS_2$@ZnS QDs/Carbon	8.42 6.01 (pure)	1.45 1.34	7.47 6.13	0.78 0.73	Optimize interfacial energy-level alignment, improve hole extraction and enhance moisture stability of PSCs	[207]
CdZnSe@ZnSe (~6 nm)	Hot-injection process	FTO/c-TiO_2/m-TiO_2/$CsPbBr_3$/CdZnSe@ZnSe QDs/Carbon	7.53 8.65 (pure)	1.41 1.50	6.88 7.25	0.78 0.80	Optimize interfacial energy-level alignment, improve hole extraction and moisture stability of PSCs	[84]
MoS_2 (~2.6 nm)	solvothermal reaction	FTO/c-TiO_2/m-TiO_2/$MAPbI_3$/MoS_2 QDs:Reduced graphene oxide/Spiro-OMeTAD/Au	20.12 17.53 (pure)	1.11 1.06	22.81 21.49	0.80 0.78	Optimize interfacial energy-level alignment, improve hole extraction and enhance long-term stability of PSCs	[62]
CdTe (10–20 nm)	Hot-injection process	ITO/SnO_2/$FA_{0.57}MA_{0.43}PbI_xBr_yCl_{3-x-y}$/CdTe QDs/Spiro-OMeTAD/Au	17.87 16.83 (pure)	1.05 1.06	23.46 22.38	0.72 0.71	Optimize interfacial energy-level alignment, enhance hole transport and reduce hysteresis	[188]
PbS (~3.4 nm)	Hot-injection process	FTO/c-TiO_2/$MAPbI_3$/PbS QDs/ Spiro-OMeTAD/Au	19.24 17.46 (pure)	1.14 1.08	23.17 22.71	0.73 0.71	Improve perovskite quality, optimize interfacial energy-level alignment and enhance hole transport of PSCs	[209]
CdSe (~3 nm):$CsPbI_3$ (15–20 nm)	Hot-injection process	FTO/c-TiO_2/m-TiO_2/$MAPbI_3$/CdSe:$CsPbI_3$ QDs/Spiro-OMeTAD/Au	17.10 14.00 (pure)	0.98 0.94	24.60 20.70	0.71 0.72	Improve light harvesting, optimize interfacial energy-level alignment and enhance hole transport of PSCs	[76]
$PbSO_4(PbO)_4$ (2–5 nm)	Hot-injection process	FTO/c-TiO_2/m-TiO_2/$MAPbI_3$/$PbSO_4(PbO)_4$ QDs/Spiro-OMeTAD/Au	20.35 17.20 (pure)	1.10 1.09	24.68 21.62	0.75 0.73	Optimize interfacial energy-level alignment, improve hole extraction and enhance moisture stability of PSCs	[208]

(*continued on next page*)

Table 7 (*continued*)

QDs (diameter)	Synthesis method	Cell structure	Cell performance				QD effect	Ref.
			η (%)	V_{OC} (V)	J_{SC} (mA cm^{-2})	*FF*		
Si (~10 nm)	Chemical etching reaction	FTO/c-TiO_2/m-TiO_2/$CsPbBr_3$/Si QDs/ Spiro-OMeTAD/Ag	8.31 3.07 (pure)	1.42 1.05	7.80 4.80	0.75 0.61	Improve light harvesting, optimize interfacial energy-level alignment and enhance hole transport of PSCs	[210]
Black phosphorus (~5.2 nm)	Solid calcination process	ITO/PEDOT:PSS/Black phosphorus QDs/$MAPbI_3$/PCBM/Ag	16.69 14.10 (pure)	1.01 0.92	20.13 19.17	0.80 0.78	Improve perovskite quality, optimize interfacial energy-level alignment and enhance hole transport of PSCs	[69]
Carbon (~20 nm)	Pyrolysis process	FTO/c-TiO_2/m-TiO_2/$CsPbBr_3$/Carbon QDs/ Spiro-OMeTAD/Ag	8.29 5.25 (pure)	1.06 0.93	11.34 9.25	0.69 0.61	Improve light harvesting, improve hole extraction and enhance humidity stability of PSCs	[185]

homogeneously distribute on the perovskite surface due to strong binding between their S^{2-} and Se^{2-} ions and the Pb^{2+} ions of perovskites (Fig. 20a). DFT calculations revealed that the binding energy between the perovskite and QDs was higher for CdSe@ZnS QDs (Fig. 20c–f), which suggests that it has a stronger interaction with the perovskite than CdS@ZnS QDs. This was attributed to the lower electronegativity of the Se^{2+} ions in CdSe than that of the S^{2-} ions in CdS. The CdSe@ZnS QDs exhibited more efficient passivation of surface defects and grain boundary traps (Fig. 20g–j), leading to PSCs with remarkably improved PCE (19.89% vs. 17.06% of the pristine one), alleviated hysteresis, and long term thermal stability (Fig. 20b) [85].

In another study, $CsPbBrCl_2$ QDs were dispersed in toluene and applied as an anti-solvent to facilitate crystallization in a one-step spin-coating synthesis of $MAPbI_3$ films (Fig. 21a) [203]. Bulk perovskite films made with this strategy showed substantial surface passivation and hydrophobicity, both of which were ascribed to the surface capped with OA ligands and multiple elements in the $CsPbBrCl_2$ QDs (Fig. 21b–f). PSCs made with $CsPbBrCl_2$ QDs demonstrated significantly increased the PCEs (from 18.30% to 20.90%) and enhanced device stability (Fig. 21g and h). Similarly, solutions of chlorobenzene and various halide perovskite QDs (i.e., $CsPbBr_3$, $FAPbBr_3$ and $MAPbBr_3$) were used as an anti-solvent in one-step spin-coating processes in order to rationally modify the morphology, crystallization and electronic structure of perovskite absorbers [183]. The $CsPbBr_3$ QD-based PSCs demonstrated the best PCE (i.e., 21.03% vs. 19.08% for the pristine one), probably because of the optimized size and concentration of $CsPbBr_3$ QDs.

Quantum dots at interfaces between hole transport layers and perovskite films

Significantly, a variety of QD materials (e.g., halide perovskites, metal sulfides, selenides and tellurides, black phosphorus, carbon, graphdiyne and graphene) mentioned above can also be used to effectively engineer the interface between perovskite and HTL by improving perovskite quality, optimizing energy-level alignment, facilitating hole extraction, retarding photocurrent hysteresis, and enhancing device stability of PSCs, as shown in Table 7 [62,69,72,75,76,84,86,87,184–189,192–195,204–211].

$MAPbBr_{3-x}I_x$ QDs were dispersed into chlorobenzene and used as an anti-solvent for the preparation of the $MAPbI_3$ films. It was found that coating $MAPbBr_{3-x}I_x$ QDs onto the perovskite absorber had a negligible effect on light harvesting of PSCs, but when the valence band (VB) edge of $MAPbBr_{0.9}I_{2.1}$ QDs was situated between the VB edge of $MAPbI_3$ and the highest occupied molecular orbital (HOMO) of Spiro-OMeTAD, hole extraction efficiency spiked and the PCE of PSCs increased from 10.34% to 13.32% [184]. Besides, stable Mn-doped $CsPbI_3$ QDs were rationally prepared, stabilized by capping with both long-chain oleic acid/oleylamine and short-chain KSCN, and then post-treated with an FAI solution. The partial substitution of Pb^{2+} with Mn^{2+} ions has been found to stabilize the cubic phase of $CsPbI_3$. The incorporation of short-chain KSCN has been demonstrated to prevent aggregation of $CsPbI_3$ QDs (after the eventual removal of long-chain oleic acid/oleylamine) because of the strong crosslinking between the SCN^- and perovskites, forming Pb—S and N—H bonds (Fig. 22a). Surface modification with the FAI solution has been found to further improve electronic coupling and charge transport of $CsPbI_3$ QDs. These modified $CsPbI_3$ QDs were then spin coated onto the $CsPbI_2Br$ films. Due to their lower band gaps (i.e., 1.77 eV for $CsPbI_3$ vs. 1.91 eV of $CsPbI_2Br$), the $CsPbI_3$ QDs increased the light harvesting of PSCs (Fig. 22b). Ion exchange between $CsPbI_2Br$ and of $CsPbI_3$ also resulted in the formation of a robust heterojunction structure between the two inorganic perovskites. The formation of $CsPbI_{2+x}Br_{1-x}$ ($0 \le x \le 1$) via this ion exchange process resulted in a graded energy-level alignment (Fig. 22c and d), which helped accelerate charge extraction in the PSCs. Consequently,

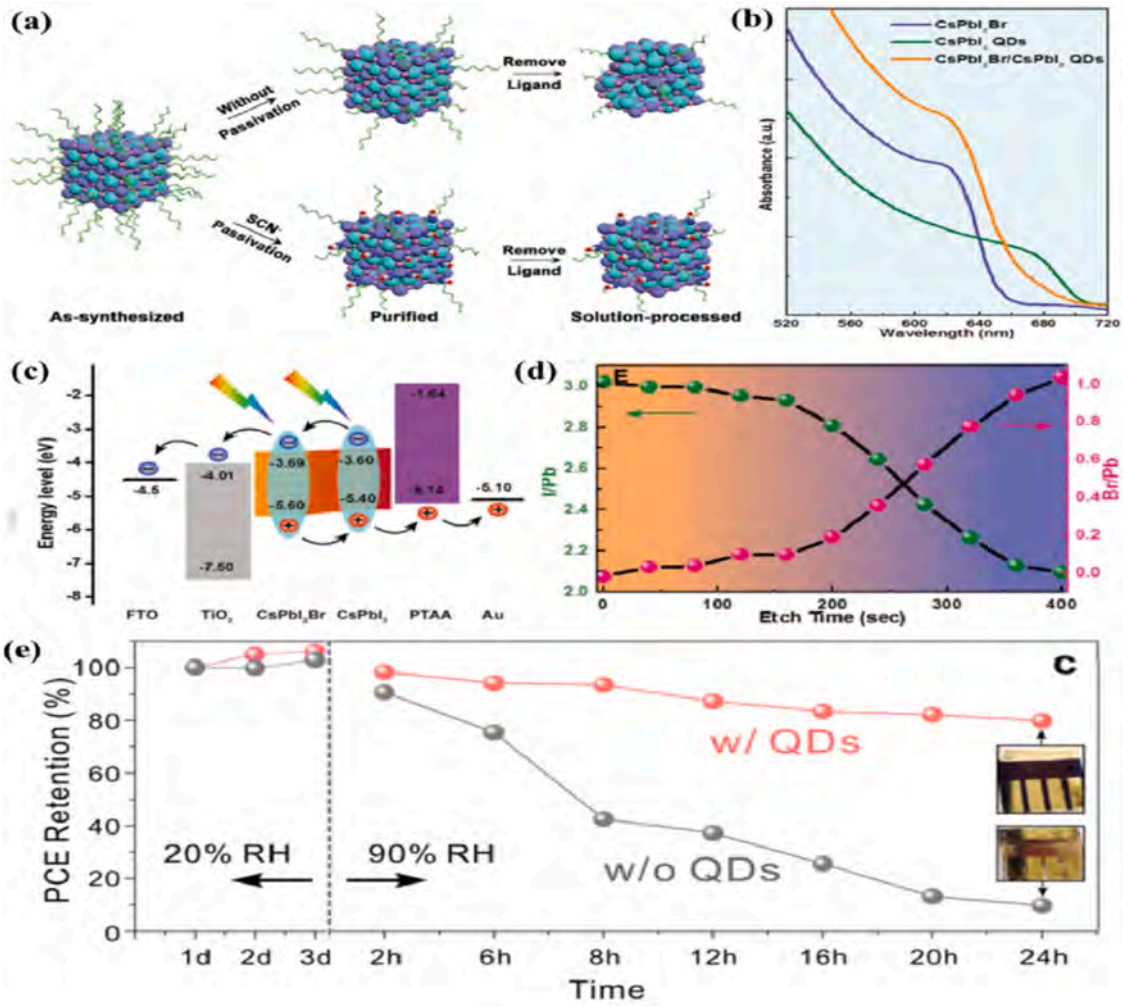

Fig. 22. (a) Schematic diagram of $CsPbI_3$ QDs with/without the SCN^- capping. (b) UV–Vis absorption spectra of different QD perovskites. (c) Schematic illustration of the energy level alignment of the $CsPbI_2Br/CsPbI_3$ PSCs. (d) Vertical composition profile of the surface for $CsPbI_2Br/CsPbI_3$ film [186]. Printed with permission from Elsevier. (e) Moisture stability of the PSCs with/without $Cs_{0.57}FA_{0.43}PbI_3$ QDs in ambient conditions [86]. Printed with permission from American Chemical Society.

$CsPbI_2Br/CsPbI_3$ PSCs displayed an improved PCE of 14.45%, which was superior to that of the pure $CsPbI_2Br$ (13.45%) and $CsPbI_3$ (10.97%) [186]. In addition, $Cs_{0.57}FA_{0.43}PbI_3$ QDs were deposited onto $FAPbI_3$, creating a Cs-rich surface on the perovskite and remarkably enhancing the humidity stability of the resulting PSCs (Fig. 22e) [86].

CdTe QDs were capped with a variety of ligands (e.g. oleic acid, MAI, PbI_2 and $MAPbI_3$) and employed as interfacial modifiers in PSCs [188]. Only the $MAPbI_3$-capped CdTe QD-based device possessed a PCE comparable to that of the pristine cell without QDs. Notably, the $MAPbI_3$-capped CdTe QD-based device showed reduced photocurrent hysteresis. It was indicated that the substitution of long-chain oleic acid with $MAPbI_3$ on the surface of CdTe QDs via a ligand exchange process was able to effectively enhance the charge transport dynamic across the interface between perovskites and HTLs. In addition, MoS_2 QDs were combined with (3-mercaptopropyl)trimethoxysilane-functionalized reduced graphene oxide (RGO) nanosheets and then placed between the perovskite layer and the HTL (Fig. 23a) [62]. The MoS_2 QDs and RGO nanosheets were found to strongly interact via S-S van der Waals physisorption (Fig. 23b). The MoS_2 QDs were observed to efficiently extract holes, but hinder electron transport. The incorporation of RGO facilitated a homogenous coverage of MoS_2 QD films without pinholes onto the $MAPbI_3$ layer (Fig. 23c and d). Notably, the modified PSCs with the MoS_2/RGO composite displayed superior PCEs and stability (Fig. 23e and f) [62].

Additionally, $PbSO_4(PbO)_4$ QDs capped with oleic acid ligands were found to effectively passivate surface defects of perovskite films by forming hydrogen bonds between the H^+ ions of oleic acid and the I^- ions of $MAPbI_3$, and ionic Pb—O bonds between the SO_4^{2-} ions of $PbSO_4(PbO)_4$ and the Pb^{2+} ions of $MAPbI_3$. Meanwhile, the insertion of $PbSO_4(PbO)_4$ QDs was observed to improve hole extraction and facilitate charge transport in PSCs. DFT calculations suggest that the $PbSO_4(PbO)_4$ QDs helped form an interfacial electric field at the interface between perovskite and Spiro-OMeTAD, which was beneficial for hole transfer of PSCs. Moreover, the $PbSO_4(PbO)_4$ QDs boosted the moisture and oxygen resistance for PSCs. PSCs modified with $PbSO_4(PbO)_4$ QDs demonstrated a PCE

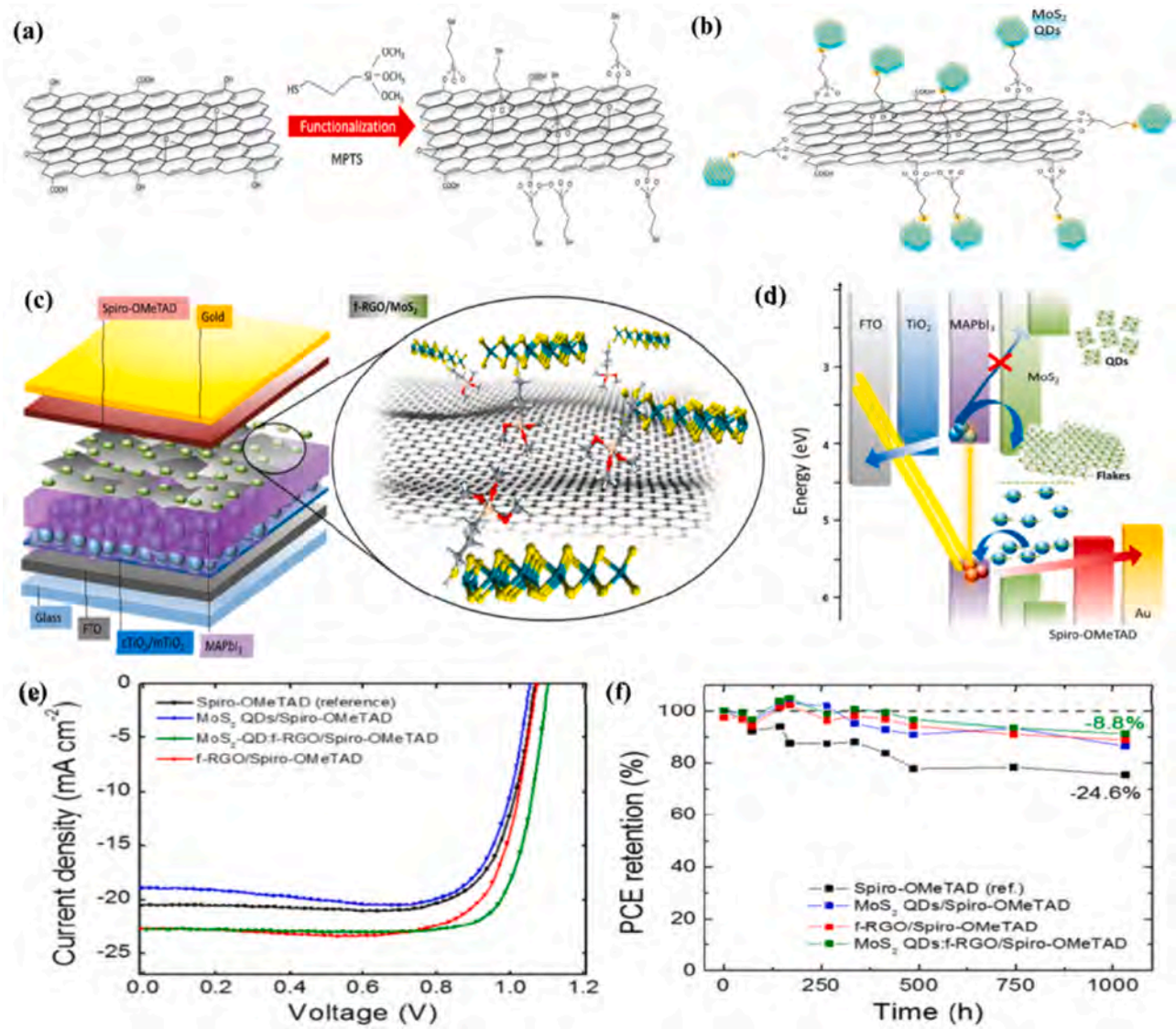

Fig. 23. Schematic diagrams of (a) the functionalization process of the reduced graphene oxide (f-RGO) nanosheets with (3-mercaptopropyl)trimethoxysilane (MPTS), (b) the interaction between MoS_2 QDs and functionalized RGO, (c) device structure and (d) energy level alignment of the PSCs modified with the f-RGO/MoS_2 QDs. (e) J-V curves and (f) long-term stability of the PSCs with/without different interfacial modifiers [62]. Printed with permission from American Chemical Society.

increase from 16.86% to 20.02% and enhanced long-term humidity stability with 90% efficiency retention (vs. 22% retention of the pristine one) after continuously measurement for 280 h in ambient air (humidity: ~65%) [208]. Interestingly, carbon and Si QDs were deposited onto porous three dimensional (3D) inverse opal $CsPbBr_3$ films [185,210]. These carbon and Si QDs were both found to enhance light harvesting and improve charge transport dynamics of the resulting PSCs. Because of their nature as a great fluorescence resonance energy transfer (FRET) donor material, the Si QDs were able to form a donor-acceptor system with $CsPbBr_3$ to excite additional light absorption from the photoluminescence of Si QDs, and then further enhance the solar harvesting efficiency [210].

Quantum dots in the light down converting layers

Many strategies have been proposed to mitigate degradation of organic-inorganic perovskite films from moisture, high-temperature and UV [149,212]. Prolonged exposure to high energy UV photons has been shown to damage organic components in perovskites [213]. In PSCs based on mesoporous or planar sandwich structures, most UV photons are absorbed by the transparent conductive substrates (i.e., FTO or ITO) and charge transport layers (e.g., TiO_2, ZnO, SnO_2 or NiO_x), which have wide band gaps that allow for the harvest of UV light. This parasitic light absorption enhances photostability of PSCs, but also decreases light harvesting efficiency [214]. Moreover, the high photocatalytic activity of TiO_2 films has been found to reduce the stability of TiO_2-based PSCs. Therefore, enhancing UV-photostability of PSCs is of paramount importance.

Coating an additional energy-down-shift (EDS) layer on the illumination side of PSCs has been identified as a promising strategy to improve UV photostability. This EDS layer is intended to directly convert UV-radiation into visible light, which has been demonstrated to enhance both PSC photostability and photocurrent. Various luminescent materials (e.g., QDs, rare earth ions/compounds, and organic dyes) have been utilized in EDS applications

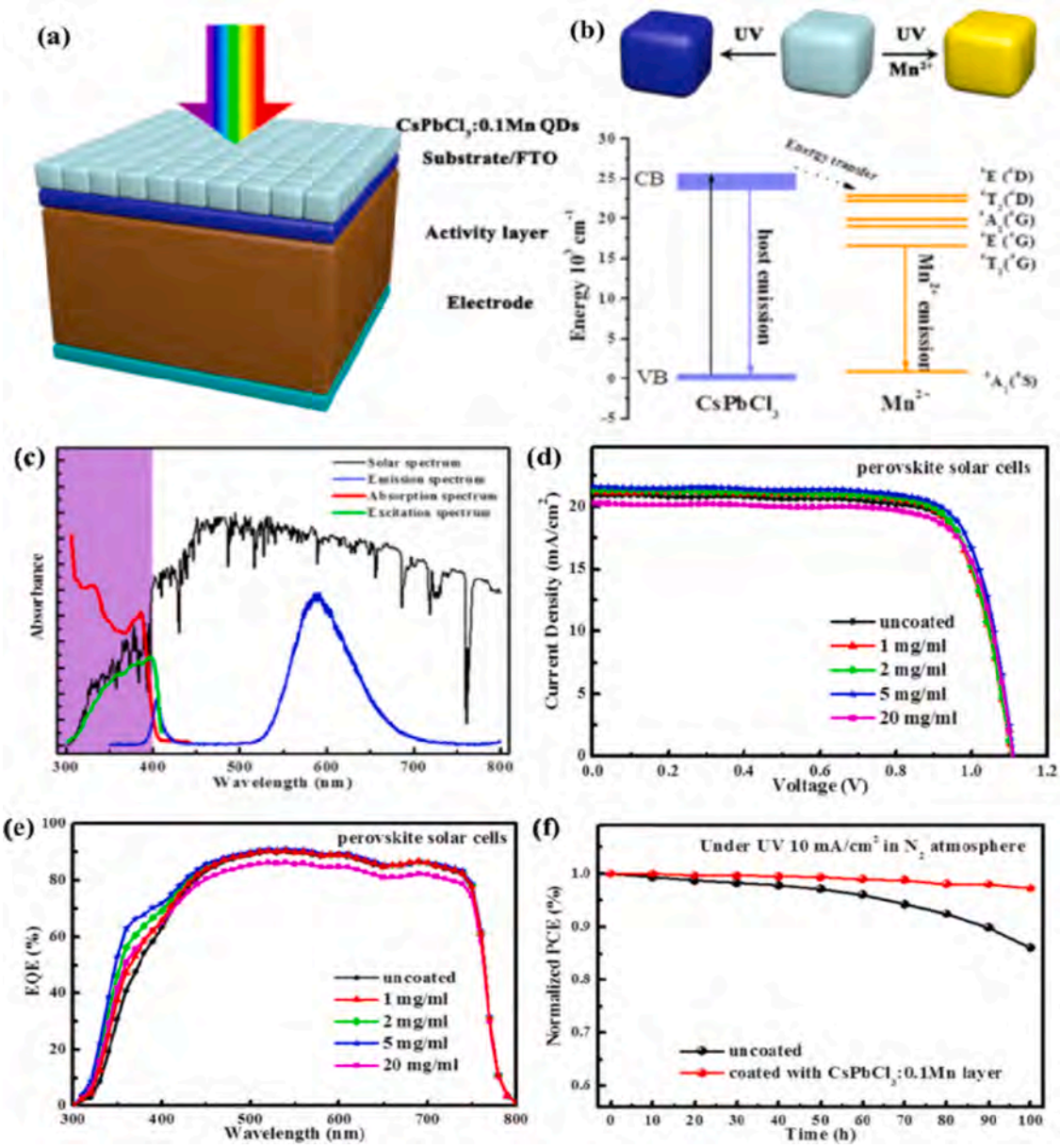

Fig. 24. Schematic diagrams of (a) PSCs coated with an Mn-doped $CsPbCl_3$ QD layer on the illumination side, and (b) the energy level alignment of the Mn-doped $CsPbCl_3$ QDs. (c) Solar spectrum, and absorption/excitation/emission (365 nm excitation) spectra of the Mn-doped $CsPbCl_3$ QDs. (d) J-V curves, (e) external quantum efficiency (EQE) spectra, and (f) UV-photostability of PSCs with/without the Mn-doped $CsPbCl_3$ QDs [217]. Printed with permission from American Chemical Society.

[215,216]. The most relevant to this review are a series of QDs (e.g., graphene, carbon, ZnSe, and Mn-doped $CsPbCl_3$) with attractive properties (e.g., high photoluminescence quantum efficiency, tunable wide band gaps, large absorption coefficient and great photostability) that have been applied as EDS layers to simultaneously enhance cell efficiency and UV-photostability of PSCs [213–215,217–219]. For example, Mn-doped $CsPbCl_3$ QDs have been deposited on the illumination side of PSCs for use as an EDS layer (Fig. 24a). Mn-doped $CsPbCl_3$ QDs were selected because of the intriguing properties owing to the incorporation of Mn^{2+} ions, including a significantly increased Stokes shift and UV-induced light emission at 590 nm (vs. 402 nm for the pure $CsPbCl_3$ QDs) (Fig. 24b and c), producing a photoluminescence quantum yielding of ~60%. PSCs with the Mn-doped $CsPbCl_3$ QD EDS layer demonstrated improved PCEs with increased photocurrents from the additional UV-light absorption, and enhanced photostability (Fig. 24d–f) [217]. N-doped graphene QDs have also been shown to effectively down convert UV light [219]. The QDs can absorb UV light around 255 nm via the π-π* transition of their aromatic sp^2 groups and then emit visible light at 585 nm with a photoluminescence quantum yield up to 80%. When employed as an EDS layer in the $CsPbI_3$-based PSCs, the N-doped graphene QDs were found to improve both cell efficiency (16.02% vs. 15.53% for the pristine one) and photostability [219].

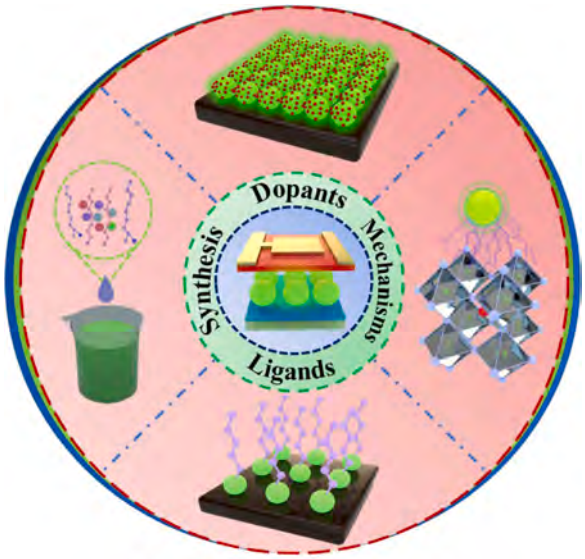

Fig. 25. Schematic diagram of the key aspects for quantum dot materials used in PSCs.

Conclusion and outlook

In this review, recent developments regarding the incorporation of a variety of QD materials in PSCs have been comprehensively summarized. A diverse range of QDs (e.g., carbon, graphene, metal sulfides/selenides/tellurides, black phosphorus, organic/inorganic halide perovskites, etc.) with fantastic optoelectronic properties have been shown to increase the efficiency and stability of PSCs. This review presents a detailed overview of the roles and functions of QDs in PSCs. Many advanced materials in the form of QDs can be exploited as light harvesters (e.g., organic/inorganic halide perovskites), charge carrier transporters (e.g., metal oxides/sulfides/selenides and black phosphorous), film additives and interfacial modifiers (e.g., graphene, carbon, metal sulfides/selenides, and black phosphorous) in PSCs. The incorporation of QDs has been shown to effectively improve perovskite crystallinity, increase grain size, reduce surface defects and grain boundary traps, facilitate charge transport via optimization of energy-level alignment, and enhance the long-term, thermal, moisture and photostability of PSCs. While the incorporation of QDs has produced a multitude of improvements, further modification of QDs is still necessary in order to unlock their full potential in PSCs. These further necessary developments are discussed below (Fig. 25).

First, judicious ligand engineering is particularly essential to effectively use QDs in PSCs [54,55,134,135,143,188,203,220]. QDs (e.g., organic/inorganic halide perovskites) are conventionally stabilized by long-chain ligands (e.g., oleic acid and oleylamine) that are detrimental to fast charge transport in PSCs [137]. Unfortunately, substitution of short-chain ligands, which is beneficial for charge extraction, leads to aggregation of QDs. Thus, it is imperative to balance dispersion and charge transport. Top achieve this, careful purification and ligand exchange of as-synthesized (long ligand) QDs is essential. Crafting QDs with a mixture of short and long chang ligands has been proven to be a promising strategy for the production of stable QDs with satisfactory electronic properties [134]. Additionally, solvent effects on QDs must also be taken into account. As an example, halide perovskite QDs are commonly stabilized with oleylamine and oleic acid ligands. These ligands bind to the surface of halide perovskite QDs via oleylammonium halide and oleylammonium carboxylates [54], which are ionic bonds that are easily destroyed when exposed to highly polar solvents (e.g, methanol, ethanol, isopropanol, acetonitrile and water), leading to aggregation of QDs. The use of highly non-polar solvents (e.g., hexane, toluene, and octane) isn't able to break these ionic bonds and remove the long-chain ligands for the further purify of QDs. Thus, solvent engineering presents a promising strategy to control the ligand density on the surface of QDs. Solvents with moderate polarity (e.g., ethyl acetate, methyl acetate, 2-pentanol, and t-butanol) are capable of properly removing the ligands while keeping QDs stable [55,221]. Meanwhile, a mixture of polar and non-polar solvents (e.g., acetonitrile and toluene) can also be used for surface treatment of QDs [55,186]. Therefore, it is complicated but critical to modify the surface chemistry of QDs via ligand/solvent engineering processes. Moreover, different functional groups (e.g., −OH, −COOH, $-NH_2$, and −SH) can be introduced onto the surface of QDs (e.g., graphene and carbon) via ligand exchange or doping processes [66,73,182,192], which may strongly interact with the ions (e.g., Pb^{2+} or I^-) of perovskites, consequently passivating crystal defects and traps, enhancing the electronic coupling among perovskites, and then promoting carrier extraction of PSCs.

Second, elemental doping (e.g., Mn, Al, Yb, N, S and F) presents an effective strategy to improve the photoelectronic properties of QDs, such as conductivity, carrier mobility, energy band structures, chemical stability and photoluminescence [73,101,137,186,192,222]. Among them, Mn^{2+} doping has been widely applied to modify the photoelectronic properties of metal sulfides/selenides and halide perovskite QDs [217,223,224]. Doping other transition (e.g, Ni^{2+}, Co^{2+}, Cu^{2+}, and Zn^{2+}) and rare earth (e.g., La^{3+}, Eu^{3+}, Sm^{3+}, Ce^{3+}, Er^{3+}, Nd^{3+}, and Tb^{3+}) elements into bulk perovskites has also been extensively reported [225–232], and stands as a promising method to further enhance the chemical stability, photoluminescence quantum yield, and external quantum efficiency of perovskite QDs. In addition, Sn^{2+} cations have been proven to be an effective substitute for toxic Pb^{2+} cations in both bulk and QD halide perovskites structures [30,33,233,234]. Accordingly, other divalent cations like Ca^{2+}, Sr^{2+}, Ba^{2+}, and Ge^{2+} have been doped into the bulk perovskites [26,154,235–237], with the aim to reduce toxicity and improve their quality and stability. Some monovalent (e.g., Li^+, K^+, Na^+, Ag^+ and Rb^+) and trivalent (e.g., Bi^{3+} and Sb^{3+}) cations have also been doped into bulk perovskite films [50,238–242]. Ideally, any dopant successful incorporated into bulk perovskite should also be investigated in QD systems. Thus, there are still many choices for the doping treatment of halide perovskite QDs. Doping impurity ions into the lattice of QDs can, however, induce some challenges such as charge mismatch and low substitution concentration. It may be feasible to adopt a co-doping strategy (e.g., co-doping monovalent/trivalent ions) to alleviate these issues [243]. Impressively, alloyed perovskite QDs (e.g., $Cs_{1-x}FAPbI_3$ [56,57], $(FA_{1-x}Cs_x)Pb(I_{1-x}Br_x)_3$ [138], and $CsPb_{1-x}Sn_xBr_3$ [34,128]) have been found to boost device stability, light harvesting, and V_{OC} values for PSCs. However, the highest certified PCE of 16.6% (J_{SC}: 18.30 mA cm^{-2}; V_{OC}: 1.17 V; *FF*: 0.783) for the PSCs based on the $Cs_{1-x}FA_xPbI_3$ QDs still falls far behind that (25.2%) of the bulk perovskite devices. Additionally, the multiexciton generation effect of QDs to surpass the Shockley-Queisser limit is rarely reported and discussed for PSCs. There is still significant untapped opportunity in improving the photocurrent of perovskite QD-based PSCs.

Third, achieving a fundamental understanding of the possible mechanisms (e.g., surface chemistry, chemical bonding and interaction) and impact of QDs on PSCs is of paramount importance. Such a study could yield insights into how the incorporation of QDs effects properties like perovskite crystallization, defect passivation and electronic transport [81,85,109,132,150,208]. More significantly, it is possible to further guide the experimental procedures via helpful characterization and simulation methods. In recent years, several characterization techniques, such as in-situ Transmission Electron Microscope (TEM) [244], and Atomic Force Microscopy (AFM) [245,246], have been developed and exhibited attractive advantages in the research of energy conversion devices. These in-situ

observation methods may make it feasible to scrutinize the crystal defects of QDs, chemical interaction between QDs and perovskites, and interfacial charge extraction/transport. Furthermore, theoretical simulation (e.g., density functional theory (DFT) and generalized gradient approximation (GGA)) is considered to be a powerful method that can provide significant insights into the electronic and structural nature of materials and interfaces for PSCs [85,109,208]. Therefore, it may be helpful to investigate QDs for PSCs via simulation calculation, for example: (1) describing the electronic structures of QDs, including the energy band gaps, valence band maximum (VBM) and conduction band minimum (CBM) to comprehend the quantum confinement effect on QDs and optimize the energy-level alignment in PSCs [208,223,247,248]; (2) estimating the thermodynamically stable phase and geometry of QDs and perovskites [74,109]; (3) evaluating the trap-state density on the surface of QDs and perovskite films [85,249,250]; (4) calculating the binding, absorption or formation energy of QDs on perovskites [134,141,251]; (5) illustrating the spatial charge distribution near the interfacial regions to find the charge difference before and after the introduction of QDs, and modulate the interfaces between perovskite and charge transport layers for enhanced charge extraction and transport in PSCs [150,252].

Fourth, facile and high-output synthesis strategies of stable QDs are urgently needed. Presently, hot injection is the most popular strategy for synthesizing QD materials (e.g., metal sulfides and organic/inorganic halide perovskites) [34,83,130,136,173,175,203]. Unfortunately, hot injection is usually complex, toxic, and requires the use of unstable organic solvents. In the hot injection process, high temperature and inert atmosphere are unavoidable, leading to high costs and limit yield for QDs. Additionally, it will be hard to obtain uniform QDs with high quality and good dispersity when the reactions are amplified for large-scale production, mainly due to the agent injection procedure with its high localization limitation. Room temperature solution synthesis via ligand and solvent engineering [48], but without inert gas and injected agents is promising for the commercial applications of QDs in PSCs.

CRediT authorship contribution statement

Meidan Ye: Writing – original draft, Writing – review & editing. **Gill M. Biesold:** Writing – review & editing. **Meng Zhang:** Writing – review & editing. **Weiguo Wang:** Writing – review & editing. **Tian Bai:** Writing – review & editing. **Zhiqun Lin:** Writing – review & editing, Supervision.

Declaration of Competing Interest

The authors declare that they have no known competing financial interests or personal relationships that could have appeared to influence the work reported in this paper.

Acknowledgments

The work is supported by the National Natural Science Foundation of China (No. 22075237), the Natural Science Foundation of Fujian Province of China (No. 2020J01007), and the NSF (CMMI 1914713; CBET 1803495; DMR 1903990).

References

[1] L. Quyet Van, K. Hong, H.W. Jang, S.Y. Kim, Halide perovskite quantum dots for light-emitting diodes: properties, synthesis, applications, and outlooks, Adv. Electron. Mater. 4 (2018) 1800335.
[2] Aa.O. El-Ballouli, O.M. Bakr, O.F. Mohammed, Compositional, processing, and interfacial engineering of nanocrystal- and quantum-dot-based perovskite solar cells, Chem. Mater. 31 (2019) 6387–6411.
[3] H. Li, W. Shi, W. Huang, E.-P. Yao, J. Han, Z. Chen, S. Liu, Y. Shen, M. Wang, Y. Yang, Carbon quantum dots/TiO_x electron transport layer boosts efficiency of planar heterojunction perovskite solar cells to 19%, Nano Lett. 17 (2017) 2328–2335.
[4] A. Kojima, K. Teshima, Y. Shirai, T. Miyasaka, Organometal halide perovskites as visible-light sensitizers for photovoltaic cells, J. Am. Chem. Soc. 131 (2009) 6050–6051.
[5] J.-H. Im, C.-R. Lee, J.-W. Lee, S.-W. Park, N.-G. Park, 6.5% Efficient perovskite quantum-dot-sensitized solar cell, Nanoscale 3 (2011) 4088–4093.
[6] M.M. Lee, J. Teuscher, T. Miyasaka, T.N. Murakami, H.J. Snaith, Efficient hybrid solar cells based on meso-superstructured organometal halide perovskites, Science 338 (2012) 643–647.
[7] M. Liu, M.B. Johnston, H.J. Snaith, Efficient planar heterojunction perovskite solar cells by vapour deposition, Nature 501 (2013) 395–398.
[8] N.J. Jeon, H.G. Lee, Y.C. Kim, J. Seo, J.H. Noh, J. Lee, S.I. Seok, o-Methoxy substituents in spiro-OMeTAD for efficient inorganic-organic hybrid perovskite solar cells, J. Am. Chem. Soc. 136 (2014) 7837–7840.
[9] H. Zhou, Q. Chen, G. Li, S. Luo, T.-b Song, H.-S. Duan, Z. Hong, J. You, Y. Liu, Y. Yang, Photovoltaics. Interface engineering of highly efficient perovskite solar cells, Science 345 (2014) 542–546.
[10] M. Saliba, S. Orlandi, T. Matsui, S. Aghazada, M. Cavazzini, J.-P. Correa-Baena, P. Gao, R. Scopelliti, E. Mosconi, K.-H. Dahmen, A molecularly engineered hole-transporting material for efficient perovskite solar cells, Nat. Energy 1 (2016) 1–7.
[11] W.S. Yang, B.-W. Park, E.H. Jung, N.J. Jeon, Y.C. Kim, D.U. Lee, S.S. Shin, J. Seo, E.K. Kim, J.H. Noh, Iodide management in formamidinium-lead-halide-based perovskite layers for efficient solar cells, Science 356 (2017) 1376–1379.
[12] Q. Jiang, Y. Zhao, X. Zhang, X. Yang, Y. Chen, Z. Chu, Q. Ye, X. Li, Z. Yin, J. You, Surface passivation of perovskite film for efficient solar cells, Nat. Photonics 13 (2019) 460–466.
[13] Q. Zeng, X. Zhang, C. Liu, T. Feng, Z. Chen, W. Zhang, W. Zheng, H. Zhang, B. Yang, Inorganic $CsPbI_2Br$ perovskite solar cells: the progress and perspective, Sol. RRL 3 (2019) 1800239.
[14] F. Zhang, K. Zhu, Additive engineering for efficient and stable perovskite solar cells, Adv. Energy Mater. 10 (2020) 1902579.
[15] J. Chen, N.-G. Park, Causes and solutions of recombination in perovskite solar cells, Adv. Mater. 31 (2019) 1803019.
[16] M. Ye, X. Hong, F. Zhang, X. Liu, Recent advancements in perovskite solar cells: flexibility, stability and large scale, J. Mater. Chem. A 4 (2016) 6755–6771.
[17] M. Ye, C. He, J. Iocozzia, X. Liu, X. Cui, X. Meng, M. Rager, X. Hong, X. Liu, Z. Lin, Recent advances in interfacial engineering of perovskite solar cells, J. Phys. D: Appl. Phys. 50 (2017) 373002.
[18] M. Zhang, X. Cui, Y. Wang, B. Wang, M. Ye, W. Wang, C. Ma, Z. Lin, Simple route to interconnected, hierarchically structured, porous Zn2SnO4 nanospheres as electron transport layer for efficient perovskite solar cells, Nano Energy 71 (2020) 104620.
[19] Q. Zeng, X. Zhang, X. Feng, S. Lu, Z. Chen, X. Yong, S.A.T. Redfern, H. Wei, H. Wang, H. Shen, W. Zhang, W. Zheng, H. Zhang, J.S. Tse, B. Yang, Polymer-passivated inorganic cesium lead mixed-halide perovskites for stable and efficient solar cells with high open-circuit voltage over 1.3 V, Adv. Mater. 30 (2018) 1705393.
[20] J. Li, R. Munir, Y. Fan, T. Niu, Y. Liu, Y. Zhong, Z. Yang, Y. Tian, B. Liu, J. Sun, Phase transition control for high-performance blade-coated perovskite solar cells, Joule 2 (2018) 1313–1330.
[21] L. Yang, C. Dall'Agnese, Y. Dall'Agnese, G. Chen, Y. Gao, Y. Sanehira, A.K. Jena, X.F. Wang, Y. Gogotsi, T. Miyasaka, Surface-modified metallic $Ti_3C_2T_x$ MXene as electron transport layer for planar heterojunction perovskite solar cells, Adv. Funct. Mater. 29 (2019) 1905694.
[22] C. Liu, W. Li, C. Zhang, Y. Ma, J. Fan, Y. Mai, All-inorganic $CsPbI_2Br$ perovskite solar cells with high efficiency exceeding 13%, J. Am. Chem. Soc. 140 (2018) 3825–3828.
[23] M. He, B. Li, X. Cui, B. Jiang, Y. He, Y. Chen, D. O'Neil, P. Szymanski, M.A. El-Sayed, J. Huang, Z. Lin, Meniscus-assisted solution printing of large-grained perovskite films for high-efficiency solar cells, Nat. Commun. 8 (2017) 16045.
[24] B. Wang, M. Zhang, X. Cui, Z. Wang, M. Rager, Y. Yang, Z. Zou, Z.L. Wang, Z. Lin, Unconventional route to oxygen-vacancy-enabled highly efficient electron extraction and transport in perovskite solar cells, Angew. Chem. Int. Ed. 59 (2020) 1611–1618.
[25] S.G. Kim, C. Li, A. Guerrero, J.M. Yang, Y. Zhong, J. Bisquert, S. Huettner, N.G. Park, Potassium ions as a kinetic controller in ionic double layers for hysteresis-free perovskite solar cells, J. Mater. Chem. A 7 (2019) 18807–18815.
[26] F. Yang, D. Hirotani, G. Kapil, M.A. Kamarudin, C.H. Ng, Y. Zhang, Q. Shen, S. Hayase, All-inorganic $CsPb_{1-x}$ Ge_x I_2 Br perovskite with enhanced phase stability and photovoltaic performance, Angew. Chem. Int. Ed. 57 (2018) 12745–12749.
[27] A. Agresti, A. Pazniak, S. Pescetelli, A. Di Vito, D. Rossi, A. Pecchia, M.A. der Maur, A. Liedl, R. Larciprete, D.V. Kuznetsov, Titanium-carbide MXenes for work function and interface engineering in perovskite solar cells, Nat. Mater. 18 (2019) 1228–1234.
[28] X. Meng, X. Cui, M. Rager, S. Zhang, Z. Wang, J. Yu, Y.W. Harn, Z. Kang, B.K. Wagner, Y. Liu, C. Yu, J. Qiu, Z. Lin, Cascade charge transfer enabled by incorporating edge-enriched graphene nanoribbons for mesostructured perovskite solar cells with enhanced performance, Nano Energy 52 (2018) 123–133.

[29] Y. Huang, W.-J. Yin, Y. He, Intrinsic point defects in inorganic cesium lead iodide perovskite $CsPbI_3$, J. Phys. Chem. C 122 (2018) 1345–1350.
[30] H. Yao, F. Zhou, Z. Li, Z. Ci, L. Ding, Z. Jin, Strategies for improving the stability of Tin-based perovskite ($ASnX_3$) solar cells, Adv. Sci. 7 (2020) 1903540.
[31] D. Yang, R. Yang, S. Priya, S. Liu, Recent advances in flexible perovskite solar cells: fabrication and applications, Angew. Chem. Int. Ed. 58 (2019) 4466–4483.
[32] N.-G. Park, K. Zhu, Scalable fabrication and coating methods for perovskite solar cells and solar modules, Nat. Rev. Mater. (2020) 1–18.
[33] S. Gu, R. Lin, Q. Han, Y. Gao, H. Tan, J. Zhu, Tin and mixed lead–tin halide perovskite solar cells: progress and their application in tandem solar cells, Adv. Mater. (2020) 1907392.
[34] H.-C. Wang, W. Wang, A.-C. Tang, H.-Y. Tsai, Z. Bao, T. Ihara, N. Yarita, H. Tahara, Y. Kanemitsu, S. Chen, R.-S. Liu, High-performance $CsPb_{1-x}Sn_xBr_3$ perovskite quantum dots for light-emitting diodes, Angew. Chem. Int. Ed. 56 (2017) 13650–13654.
[35] Y. Zhao, J. Li, Y. Dong, J. Song, Synthesis of colloidal halide perovskite quantum dots/nanocrystals: progresses and advances, Isr. J. Chem. 59 (2019) 649–660.
[36] S.Y. Park, M.Y. Baek, Y. Ju, D.H. Kim, C.S. Moon, J.H. Noh, H.S. Jung, Simultaneous ligand exchange fabrication of flexible perovskite solar cells using newly synthesized uniform tin oxide quantum dots, J. Phys. Chem. Lett. 9 (2018) 5460–5467.
[37] M.D. Ye, J.J. Gong, Y.K. Lai, C.J. Lin, Z.Q. Lin, High-efficiency photoelectrocatalytic hydrogen generation enabled by palladium quantum dots-sensitized TiO_2 nanotube arrays, J. Am. Chem. Soc. 134 (2012) 15720–15723.
[38] Y.-F. Xu, M.-Z. Yang, B.-X. Chen, X.-D. Wang, H.-Y. Chen, D.-B. Kuang, C.-Y. Su, A $CsPbBr_3$ perovskite quantum dot/graphene oxide composite for photocatalytic CO_2 reduction, J. Am. Chem. Soc. 139 (2017) 5660–5663.
[39] S. Zhang, X. Liu, C. Liu, S. Luo, L. Wang, T. Cai, Y. Zeng, J. Yuan, W. Dong, Y. Pei, Y. Liu, MoS_2 quantum dot growth induced by S vacancies in a $ZnIn_2S_4$ monolayer: atomic-level heterostructure for photocatalytic hydrogen production, ACS Nano 12 (2018) 751–758.
[40] M. Ye, C. Chen, N. Zhang, X. Wen, W. Guo, C. Lin, Quantum-dot sensitized solar cells employing hierarchical Cu_2S microspheres wrapped by reduced graphene oxide nanosheets as effective counter electrodes, Adv. Energy Mater. 4 (2014) 1301564.
[41] M. Ye, X. Wen, N. Zhang, W. Guo, X. Liu, C. Lin, In situ growth of CuS and $Cu_{1.8}S$ nanosheet arrays as efficient counter electrodes for quantum dot-sensitized solar cells, J. Mater. Chem. A 3 (2015) 9595–9600.
[42] J. Peng, Y. Chen, X. Zhang, A. Dong, Z. Liang, Solid-state ligand-exchange fabrication of $CH_3NH_3PbI_3$ capped PbS quantum dot solar cells, Adv. Sci. 3 (2016) 1500432.
[43] J.-Y. Jung, K. Zhou, J.H. Bang, J.-H. Lee, Improved photovoltaic performance of Si nanowire solar cells integrated with ZnSe quantum dots, J. Phys. Chem. C 116 (2012) 12409–12414.
[44] S. Wang, C. Bi, A. Portniagin, J. Yuan, J. Ning, X. Xiao, X. Zhang, Y.Y. Li, S.V. Kershaw, J. Tian, A.L. Rogach, $CsPbI_3$/PbSe heterostructured nanocrystals for high-efficiency solar cells, ACS Energy Lett. 5 (2020) 2401–2410.
[45] X. Zhang, Q. Zeng, Y. Xiong, T. Ji, C. Wang, X. Shen, M. Lu, H. Wang, S. Wen, Y. Zhang, X. Yang, X. Ge, W. Zhang, A.P. Litvin, A.V. Baranov, D. Yao, H. Zhang, B. Yang, A.L. Rogach, W. Zheng, Energy level modification with carbon dot interlayers enables efficient perovskite solar cells and quantum dot based light-emitting diodes, Adv. Funct. Mater. 30 (2020) 1910530.
[46] Z. Zheng, F. Zhuge, Y. Wang, J. Zhang, L. Gan, X. Zhou, H. Li, T. Zhai, Decorating perovskite quantum dots in TiO_2 nanotubes array for broadband response photodetector, Adv. Funct. Mater. 27 (2017) 1703115.
[47] J. Lu, X. Sheng, G. Tong, Z. Yu, X. Sun, L. Yu, X. Xu, J. Wang, J. Xu, Y. Shi, K. Chen, Ultrafast solar-blind ultraviolet detection by inorganic perovskite $CsPbX_3$ quantum dots radial junction architecture, Adv. Mater. 29 (2017) 1700400.
[48] X. Li, Y. Wu, S. Zhang, B. Cai, Y. Gu, J. Song, H. Zeng, $CsPbX_3$ quantum dots for lighting and displays: room-temperature synthesis, photoluminescence superiorities, underlying origins and white light-emitting diodes, Adv. Funct. Mater. 26 (2016) 2435–2445.
[49] K. Wu, G. Liang, Q. Shang, Y. Ren, D. Kong, T. Lian, Ultrafast interfacial electron and hole transfer from $CsPbBr_3$ perovskite quantum dots, J. Am. Chem. Soc. 137 (2015) 12792–12795.
[50] F. Yuan, T. Yuan, L. Sui, Z. Wang, Z. Xi, Y. Li, X. Li, L. Fan, Za Tan, A. Chen, Engineering triangular carbon quantum dots with unprecedented narrow bandwidth emission for multicolored LEDs, Nat. Commun. 9 (2018) 1–11.
[51] H. Liu, Z. Chen, H. Wang, F. Ye, J. Ma, X. Zheng, P. Gui, L. Xiong, J. Wen, G. Fang, A facile room temperature solution synthesis of SnO_2 quantum dots for perovskite solar cells, J. Mater. Chem. A 7 (2019) 10636–10643.
[52] G. Yang, C. Chen, F. Yao, Z. Chen, Q. Zhang, X. Zheng, J. Ma, H. Lei, P. Qin, L. Xiong, W. Ke, G. Li, Y. Yan, G. Fang, Effective carrier-concentration tuning of SnO_2 quantum dot electron-selective layers for high-performance planar perovskite solar cells, Adv. Mater. 30 (2018) 1706023.
[53] N. Fu, C. Huang, P. Lin, M. Zhu, T. Li, M. Ye, S. Lin, G. Zhang, J. Du, C. Liu, B. Xu, D. Wang, S. Ke, Black phosphorus quantum dots as dual-functional electron-selective materials for efficient plastic perovskite solar cells, J. Mater. Chem. A 6 (2018) 8886–8894.
[54] L.M. Wheeler, E.M. Sanehira, A.R. Marshall, P. Schulz, M. Suri, N.C. Anderson, J.A. Christians, D. Nordlund, D. Sokaras, T. Kroll, S.P. Harvey, J.J. Berry, L.Y. Lin, J.M. Luther, Targeted ligand-exchange chemistry on cesium lead halide perovskite quantum dots for high-efficiency photovoltaics, J. Am. Chem. Soc. 140 (2018) 10504–10513.
[55] J. Xue, J.-W. Lee, Z. Dai, R. Wang, S. Nuryyeva, M.E. Liao, S.-Y. Chang, L. Meng, D. Meng, P. Sun, O. Lin, M.S. Goorsky, Y. Yang, Surface ligand management for stable $FAPbI_3$ perovskite quantum dot solar cells, Joule 2 (2018) 1866–1878.
[56] M. Hao, Y. Bai, S. Zeiske, L. Ren, J. Liu, Y. Yuan, N. Zarrabi, N. Cheng, M. Ghasemi, P. Chen, M. Lyu, D. He, J.-H. Yun, Y. Du, Y. Wang, S. Ding, A. Armin, P. Meredith, G. Liu, H.-M. Cheng, L. Wang, Ligand-assisted cation-exchange engineering for high-efficiency colloidal $Cs_{1-x}FA_xPbI_3$ quantum dot solar cells with reduced phase segregation, Nat. Energy 5 (2020) 79–88.
[57] A. Hazarika, Q. Zhao, E.A. Gaulding, J.A. Christians, B. Dou, A.R. Marshall, T. Moot, J.J. Berry, J.C. Johnson, J.M. Luther, Perovskite quantum dot photovoltaic materials beyond the reach of thin films: full-range tuning of A-site cation composition, ACS Nano 12 (2018) 10327–10337.
[58] J. Yuan, A. Hazarika, Q. Zhao, X. Ling, T. Moot, W. Ma, J.M. Luther, Metal halide perovskites in quantum dot solar cells: progress and prospects, Joule 4 (2020) 1160–1185.
[59] J. Yuan, X. Zhang, J. Sun, R. Patterson, H. Yao, D. Xue, Y. Wang, K. Ji, L. Hu, S. Huang, D. Chu, T. Wu, J. Hou, J. Yuan, Hybrid perovskite quantum dot/non--fullerene molecule solar cells with efficiency over 15%, Adv. Funct. Mater. 31 (2021) 2101272.
[60] C. Liu, X. Zhou, S. Chen, X. Zhao, S. Dai, B. Xu, Hydrophobic Cu_2O quantum dots enabled by surfactant modification as top hole-transport materials for efficient perovskite solar cells, Adv. Sci. 6 (2019) 1801169.
[61] M. Lv, J. Zhu, Y. Huang, Y. Li, Z. Shao, Y. Xu, S. Dai, Colloidal $CuInS_2$ quantum dots as inorganic hole-transporting material in perovskite solar cells, ACS Appl. Mater. Interfaces 7 (2015) 17482–17488.
[62] L. Najafi, B. Taheri, B. Martín-García, S. Bellani, D. Di Girolamo, A. Agresti, R. Oropesa-Nuñez, S. Pescetelli, L. Vesce, E. Calabrò, M. Prato, A.E. Del Rio Castillo, A. Di Carlo, F. Bonaccorso, MoS_2 quantum dot/graphene hybrids for advanced interface engineering of a $CH_3NH_3PbI_3$ perovskite solar cell with an efficiency of over 20%, ACS Nano 12 (2018) 10736–10754.
[63] L. Hu, W. Wang, H. Liu, J. Peng, H. Cao, G. Shao, Z. Xia, W. Ma, J. Tang, PbS colloidal quantum dots as an effective hole transporter for planar heterojunction perovskite solar cells, J. Mater. Chem. A 3 (2015) 515–518.
[64] Y. Li, Z. Wang, D. Ren, Y. Liu, A. Zheng, S.M. Zakeeruddin, X. Dong, A. Hagfeldt, M. Grätzel, P. Wang, SnS Quantum Dots as Hole Transporter of Perovskite Solar Cells, ACS Appl. Energy Mater. 2 (2019) 3822–3829.
[65] J.-Y. Kim, W. Baek, S. Kim, G. Kang, I.K. Han, T. Hyeon, M. Park, Moisture proof hole transport layers based on CISe quantum dots for highly stable and large active area perovskite solar cells, Appl. Surf. Sci. 496 (2019) 143610.
[66] Q. Wang, Z. Jin, D. Chen, D. Bai, H. Bian, J. Sun, G. Zhu, G. Wang, S. Liu, μ-Graphene crosslinked $CsPbI_3$ quantum dots for high efficiency solar cells with much improved stability, Adv. Energy Mater. 8 (2018) 1800007.
[67] J. Xiao, J. Shi, H. Liu, Y. Xu, S. Lv, Y. Luo, D. Li, Q. Meng, Y. Li, Efficient $CH_3NH_3PbI_3$ perovskite solar cells based on graphdiyne (GD)-modified P3HT hole-transporting material, Adv. Energy Mater. 5 (2015) 1401943.
[68] Z. Yang, J. Xie, V. Arivazhagan, K. Xiao, Y. Qiang, K. Huang, M. Hu, C. Cui, X. Yu, D. Yang, Efficient and highly light stable planar perovskite solar cells with graphene quantum dots doped PCBM electron transport layer, Nano Energy 40 (2017) 345–351.
[69] W. Chen, K. Li, Y. Wang, X. Feng, Z. Liao, Q. Su, X. Lin, Z. He, Black phosphorus quantum dots for hole extraction of typical planar hybrid perovskite solar cells, J. Phys. Chem. Lett. 8 (2017) 591–598.
[70] J. Xie, K. Huang, X. Yu, Z. Yang, K. Xiao, Y. Qiang, X. Zhu, L. Xu, P. Wang, C. Cui, D. Yang, Enhanced electronic properties of SnO_2 via electron transfer from graphene quantum dots for efficient perovskite solar cells, ACS Nano 11 (2017) 9176–9182.
[71] J. Ryu, J.W. Lee, H. Yu, J. Yun, K. Lee, J. Lee, D. Hwang, J. Kang, S.K. Kim, J. Jang, Size effects of a graphene quantum dot modified-blocking TiO_2 layer for efficient planar perovskite solar cells, J. Mater. Chem. A 5 (2017) 16834–16842.
[72] X. Zhang, Q. Wang, Z. Jin, Y. Chen, H. Liu, J. Wang, Y. Li, S. Liu, Graphdiyne quantum dots for much improved stability and efficiency of perovskite solar cells, Adv. Mater. Interfaces 5 (2018) 1701117.
[73] Z. Wang, X. Rong, L. Wang, W. Wang, H. Lin, X. Li, Dual role of amino-functionalized graphene quantum dots in NiO_x films for efficient inverted flexible perovskite solar cells, ACS Appl. Mater. Interfaces 12 (2020) 8342–8350.
[74] X. Gong, L. Guan, Q. Li, Y. Li, T. Zhang, H. Pan, Q. Sun, Y. Shen, C. Grätzel, S.M. Zakeeruddin, Black phosphorus quantum dots in inorganic perovskite thin films for efficient photovoltaic application, Sci. Adv. 6 (2020) 5661.
[75] R.S. Sanchez, M.S. de la Fuente, I. Suarez, G. Muñoz-Matutano, J.P. Martinez-Pastor, I. Mora-Sero, Tunable light emission by exciplex state formation between hybrid halide perovskite and core/shell quantum dots: implications in advanced LEDs and photovoltaics, Sci. Adv. 2 (2016) 1501104.
[76] J. Ge, W. Li, X. He, H. Chen, W. Fang, X. Du, Y. Li, L. Zhao, Hybrid CdSe/$CsPbI_3$ quantum dots for interface engineering in perovskite solar cells, Sustain. Energy Fuels 4 (2020) 1837–1843.
[77] H. Chen, Q. Luo, T. Liu, J. Ren, S. Li, M. Tai, H. Lin, H. He, J. Wang, N. Wang, Goethite quantum dots as multifunctional additives for highly efficient and stable perovskite solar cells, Small 15 (2019) 1904372.
[78] J. Zhang, T. Tong, L. Zhang, X. Li, H. Zou, J. Yu, Bandgap engineering of dual acceptor-containing naphthalene diimide polymers for all-polymer solar cells, ACS Sustain. Chem. Eng. 6 (2018) 16005–16010.
[79] Y. Yang, H. Lu, S. Feng, L. Yang, H. Dong, J. Wang, C. Tian, L. Li, H. Lu, J. Jeong, S.M. Zakeeruddin, Y. Liu, M. Grätzel, A. Hagfeldt, Modulation of perovskite crystallization processes towards highly efficient and stable perovskite solar cells with MXene quantum dot-modified SnO_2, Energy Environ. Sci. 14 (2021) 3447–3454.
[80] S.-S. Li, C.-H. Chang, Y.-C. Wang, C.-W. Lin, D.-Y. Wang, J.-C. Lin, C.-C. Chen, H.-S. Sheu, H.-C. Chia, W.-R. Wu, U.S. Jeng, C.-T. Liang, R. Sankar, F.-C. Chou, C.-W. Chen, Intermixing-seeded growth for high-performance planar heterojunction perovskite solar cells assisted by precursor-capped nanoparticles, Energy Environ. Sci. 9 (2016) 1282–1289.

[81] W. Hui, Y. Yang, Q. Xu, H. Gu, S. Feng, Z. Su, M. Zhang, J. Wang, X. Li, J. Fang, F. Xia, Y. Xia, Y. Chen, X. Gao, W. Huang, Red-carbon-quantum-dot-doped SnO_2 composite with enhanced electron mobility for efficient and stable perovskite solar cells, Adv. Mater. 32 (2020) 1906374.

[82] Y. Zhou, S. Yang, X. Yin, J. Han, M. Tai, X. Zhao, H. Chen, Y. Gu, N. Wang, H. Lin, Enhancing electron transport via graphene quantum dot/SnO2 composites for efficient and durable flexible perovskite photovoltaics, J. Mater. Chem. A 7 (2019) 1878–1888.

[83] H. Wang, Y. Song, S. Dang, N. Jiang, J. Feng, W. Tian, Q. Dong, Reducing photovoltage loss in inverted perovskite solar cells by quantum dots alloying modification at cathode contact, Sol. RRL 4 (2020) 1900468.

[84] Q. Li, J. Bai, T. Zhang, C. Nie, J. Duan, Q. Tang, CdZnSe@ZnSe colloidal alloy quantum dots for high-efficiency all-inorganic perovskite solar cells, Chem. Commun. 54 (2018) 9575–9578.

[85] C. Hanmandlu, S. Swamy, A. Singh, C. Hsin-An, C.-C. Liu, C.-S. Lai, A. Mohapatra, C.-W. Pao, P. Chen, C.-W. Chu, Suppression of surface defects to achieve hysteresis-free inverted perovskite solar cellsviaquantum dot passivation, J. Mater. Chem. A 8 (2020) 5263–5274.

[86] M. Que, Z. Dai, H. Yang, H. Zhu, Y. Zong, W. Que, N.P. Padture, Y. Zhou, O. Chen, Quantum-dot-induced cesium-rich surface imparts enhanced stability to formamidinium lead iodide perovskite solar cells, ACS Energy Lett. 4 (2019) 1970–1975.

[87] C. Liu, M. Hu, X. Zhou, J. Wu, L. Zhang, W. Kong, X. Li, X. Zhao, S. Dai, B. Xu, Efficiency and stability enhancement of perovskite solar cells by introducing $CsPbI_3$ quantum dots as an interface engineering layer, NPG Asia Mater. 10 (2018) 552–561.

[88] L. Xie, K. Lin, J. Lu, W. Feng, P. Song, C. Yan, K. Liu, L. Shen, C. Tian, Z. Wei, Efficient and stable low-bandgap perovskite solar cells enabled by a $CsPbBr_3$-cluster assisted bottom-up crystallization approach, J. Am. Chem. Soc. 141 (2019) 20537–20546.

[89] L. Hu, Q. Zhao, S. Huang, J. Zheng, X. Guan, R. Patterson, J. Kim, L. Shi, C.-H. Lin, Q. Lei, D. Chu, W. Tao, S. Cheong, R.D. Tilley, A.W.Y. Ho-Baillie, J.M. Luther, J. Yuan, T. Wu, Flexible and efficient perovskite quantum dot solar cells via hybrid interfacial architecture, Nat. Commun. 12 (2021) 466.

[90] F. Cheng, R. He, S. Nie, C. Zhang, J. Yin, J. Li, N. Zheng, B. Wu, Perovskite quantum dots as multifunctional interlayers in perovskite solar cells with dopant-free organic hole transporting layers, J. Am. Chem. Soc. 143 (2021) 5855–5866.

[91] J. Shi, F. Li, Y. Jin, C. Liu, B. Cohen-Kleinstein, S. Yuan, Y. Li, Z.-K. Wang, J. Yuan, W. Ma, In situ ligand bonding management of $CsPbI_3$ perovskite quantum dots enables high-performance photovoltaics and red light-emitting diodes, Angew. Chem. Int. Ed. Engl. 59 (2020) 22230–22237.

[92] Y. Wang, J. Yuan, X. Zhang, X. Ling, B.W. Larson, Q. Zhao, Y. Yang, Y. Shi, J.M. Luther, W. Ma, Surface ligand management aided by a secondary amine enables increased synthesis yield of $CsPbI_3$ perovskite quantum dots and high photovoltaic performance, Adv. Mater. 32 (2020) 2000449.

[93] H.-C. Wang, Z. Bao, H.-Y. Tsai, A.-C. Tang, R.-S. Liu, Perovskite quantum dots and their application in light-emitting diodes, Small 14 (2018) 1702433.

[94] S. Panigrahi, S. Jana, T. Calmeiro, D. Nunes, R. Martins, E. Fortunato, Imaging the anomalous charge distribution inside $CsPbBr_3$ perovskite quantum dots sensitized solar cells, ACS Nano 11 (2017) 10214–10221.

[95] E.M. Sanehira, A.R. Marshall, J.A. Christians, S.P. Harvey, P.N. Ciesielski, L.M. Wheeler, P. Schulz, L.Y. Lin, M.C. Beard, J.M. Luther, Enhanced mobility $CsPbI_3$ quantum dot arrays for record-efficiency, high-voltage photovoltaic cells, Sci. Adv. 3 (2017) 4204.

[96] A. Swarnkar, A.R. Marshall, E.M. Sanehira, B.D. Chernomordik, D.T. Moore, J.A. Christians, T. Chakrabarti, J.M. Luther, Quantum dot-induced phase stabilization of α-$CsPbI_3$ perovskite for high-efficiency photovoltaics, Science 354 (2016) 92–95.

[97] J. Duan, Y. Zhao, B. He, Q. Tang, High-purity inorganic perovskite films for solar cells with 9.72 % efficiency, Angew. Chem. Int. Ed. 57 (2018) 3787–3791.

[98] J. Jin, C. Chen, H. Li, Y. Cheng, L. Xu, B. Dong, H. Song, Q. Dai, Enhanced performance and photostability of perovskite solar cells by introduction of fluorescent carbon dots, ACS Appl. Mater. Interfaces 9 (2017) 14518–14524.

[99] Z. Xu, Y. Jiang, Z. Li, C. Chen, X. Kong, Y. Chen, G. Zhou, J.-M. Liu, K. Kempa, J. Gao, Rapid Microwave-Assisted Synthesis of SnO_2 Quantum Dots for Efficient Planar Perovskite Solar Cells, ACS Appl. Energy Mater. 4 (2021) 1887–1893.

[100] S.N. Vijayaraghavan, J. Wall, L. Li, G. Xing, Q. Zhang, F. Yan, Low-temperature processed highly efficient hole transport layer free carbon-based planar perovskite solar cells with SnO_2 quantum dot electron transport layer, Mater. Today Phys. 13 (2020) 100204.

[101] E. Wang, P. Chen, X. Yin, Y. Wu, W. Que, Tailoring electronic properties of SnO_2 quantum dots via aluminum addition for high-efficiency perovskite solar cells, Sol. RRL 3 (2019) 1900041.

[102] E. Wang, P. Chen, X. Yin, Y. Wu, W. Que, Novel ethanol vapor annealing treatment of SnO_2 quantum dots film for highly efficient planar heterojunction perovskite solar cells, Org. Electron. 84 (2020) 105751.

[103] Y. Tu, J. Wu, M. Zheng, J. Huo, P. Zhou, Z. Lan, J. Lin, M. Huang, TiO_2 quantum dots as superb compact block layers for high-performance $CH_3NH_3PbI_3$ perovskite solar cells with an efficiency of 16.97%, Nanoscale 7 (2015) 20539–20546.

[104] S. Ameen, M.S. Akhtar, H.-K. Seo, M.K. Nazeeruddin, H.-S. Shin, An insight into atmospheric plasma jet modified ZnO quantum dots thin film for flexible perovskite solar cell: optoelectronic transient and charge trapping studies, J. Phys. Chem. C 119 (2015) 10379–10390.

[105] F. Haque, M. Wright, M.A. Mahmud, H. Yi, D. Wang, L. Duan, C. Xu, M.B. Upama, A. Uddin, Effects of hydroiodic acid concentration on the properties of $CsPbI_3$ perovskite solar cells, ACS Omega 3 (2018) 11937–11944.

[106] M. Zhang, M. Ye, W. Wang, C. Ma, S. Wang, Q. Liu, T. Lian, J. Huang, Z. Lin, Synergistic cascade carrier extraction via dual interfacial positioning of ambipolar black phosphorene for high-efficiency perovskite solar cells, Adv. Mater. 32 (2020) 2000999.

[107] A. Kaewprajak, P. Kumnorkaew, T. Sagawa, Improved photovoltaic performance and device stability of planar heterojunction perovskite solar cells using TiO_2 and TiO_2 mixed with $AgInS_2$ quantum dots as dual electron transport layers, Org. Electron. 69 (2019) 26–33.

[108] A. Kaewprajak, P. Kumnorkaew, T. Sagawa, Silver–indium–sulfide quantum dots in titanium dioxide as electron transport layer for highly efficient and stable perovskite solar cells. J. Mater. Sci. 30 (2019) 4041–4055.

[109] X. Zeng, T. Zhou, C. Leng, Z. Zang, M. Wang, W. Hu, X. Tang, S. Lu, L. Fang, M. Zhou, Performance improvement of perovskite solar cells by employing a CdSe quantum dot/PCBM composite as an electron transport layer, J. Mater. Chem. A 5 (2017) 17499–17505.

[110] S. Pang, C. Zhang, H. Zhang, H. Dong, D. Chen, W. Zhu, H. Xi, J. Chang, Z. Lin, J. Zhang, Y. Hao, Boosting performance of perovskite solar cells with graphene quantum dots decorated SnO_2 electron transport layers, Appl. Surf. Sci. 507 (2020) 145099.

[111] M. Ebrahimi, A. Kermanpur, M. Atapour, S. Adhami, R.H. Heidari, E. Khorshidi, N. Irannejad, B. Rezaie, Performance enhancement of mesoscopic perovskite solar cells with GQDs-doped TiO_2 electron transport layer, Sol. Energy Mater. Sol. Cells 208 (2020) 110407.

[112] X. Zhu, J. Sun, S. Yuan, N. Li, Z. Qiu, J. Jia, Y. Liu, J. Dong, P. Lv, B. Cao, Efficient and stable planar perovskite solar cells with carbon quantum dots-doped PCBM electron transport layer, New J. Chem. 43 (2019) 7130–7135.

[113] Z. Lv, L. He, H. Jiang, X. Ma, F. Wang, L. Fan, M. Wei, J. Yang, L. Yang, N. Yang, Diluted-CdS quantum dot-assisted SnO_2 electron transport layer with excellent conductivity and suitable band alignment for high-performance planar perovskite solar cells, ACS Appl. Mater. Interfaces 13 (2021) 16326–16335.

[114] B. Wang, J. Iocozzia, M. Zhang, M.D. Ye, S.C. Yan, H.L. Jin, S. Wang, Z.G. Zou, Z.Q. Lin, The charge carrier dynamics, efficiency and stability of two-dimensional material-based perovskite solar cells, Chem. Soc. Rev. 48 (2019) 4854–4891.

[115] F. Ke, Y. Liu, H. Xu, Y. Ma, S. Guang, F. Zhang, N. Lin, M. Ye, Y. Lin, X. Liu, Flower-like polyaniline/graphene hybrids for high-performance supercapacitor, Compos. Sci. Technol. 142 (2017) 286–293.

[116] X.R. Wen, M.Q. Zhao, D.X. Zhang, X.D. Ma, Z.Q. Lin, M.D. Ye, An integrated large-scale and vertically aligned $Co(OH)_2$ nanosheet@graphite paper electrode for high performance capacitive deionization of saline water, Desalination 470 (2019) 114117.

[117] Y. Jin, C. Hu, Q. Dai, Y. Xiao, Y. Lin, J.W. Connell, F. Chen, L. Dai, High-performance Li-CO_2 batteries based on metal-free carbon quantum dot/Holey graphene composite catalysts, Adv. Funct. Mater. 28 (2018) 1804630.

[118] X. Zhang, C. Liu, Z. Li, J. Guo, L. Shen, W. Guo, L. Zhang, S. Ruan, Y. Long, An easily prepared carbon quantum dots and employment for inverted organic photovoltaic devices, Chem. Eng. J. 315 (2017) 621–629.

[119] Z.-W. Gao, Y. Wang, H. Liu, J. Sun, J. Kim, Y. Li, B. Xu, W.C.H. Choy, Tailoring the interface in $FAPbI_3$ planar perovskite solar cells by imidazole--graphene-quantum-dots, Adv. Funct. Mater. 31 (2021) 2101438.

[120] G. Haider, P. Roy, C.-W. Chiang, W.-C. Tan, Y.-R. Liou, H.-T. Chang, C.-T. Liang, W.-H. Shih, Y.-F. Chen, Electrical-polarization-induced ultrahigh responsivity photodetectors based on graphene and graphene quantum dots, Adv. Funct. Mater. 26 (2016) 620–628.

[121] P. Tian, L. Tang, K.S. Teng, S.P. Lau, Graphene quantum dots from chemistry to applications, Mater. Today Chem. 10 (2018) 221–258.

[122] T. Yuan, T. Meng, P. He, Y. Shi, Y. Li, X. Li, L. Fan, S. Yang, Carbon quantum dots: an emerging material for optoelectronic applications, J. Mater. Chem. C 7 (2019) 6820–6835.

[123] M.J. Molaei, The optical properties and solar energy conversion applications of carbon quantum dots: a review, Sol. Energy 196 (2020) 549–566.

[124] D.H. Shin, J.M. Kim, S.H. Shin, S.-H. Choi, Highly-flexible graphene transparent conductive electrode/perovskite solar cells with graphene quantum dots-doped PCBM electron transport layer, Dyes Pigment. 170 (2019) 107630.

[125] C. Lu, H. Li, K. Kolodziejski, C. Dun, W. Huang, D. Carroll, S.M. Geyer, Enhanced stabilization of inorganic cesium lead triiodide ($CsPbI_3$) perovskite quantum dots with tri-octylphosphine, Nano Res. 11 (2018) 762–768.

[126] X. Huang, J. Hu, C. Bi, J. Yuan, Y. Lu, M. Sui, J. Tian, B-site doping of $CsPbI_3$ quantum dot to stabilize the cubic structure for high-efficiency solar cells, Chem. Eng. J. 421 (2021) 127822.

[127] S.S. Mali, C.S. Shim, C.K. Hong, Highly stable and efficient solid-state solar cells based on methylammonium lead bromide ($CH_3NH_3PbBr_3$) perovskite quantum dots, NPG Asia Mater. 7 (2015) e208e208-e208.

[128] F. Liu, C. Ding, Y. Zhang, T.S. Ripolles, T. Kamisaka, T. Toyoda, S. Hayase, T. Minemoto, K. Yoshino, S. Dai, Colloidal synthesis of air-stable alloyed $CsSn_{1-x}Pb_xI_3$ perovskite nanocrystals for use in solar cells, J. Am. Chem. Soc. 139 (2017) 16708–16719.

[129] E.M. Sanehira, A.R. Marshall, J.A. Christians, S.P. Harvey, P.N. Ciesielski, L.M. Wheeler, P. Schulz, L.Y. Lin, M.C. Beard, J.M. Luther, Enhanced mobility $CsPbI_3$ quantum dot arrays for record-efficiency, high-voltage photovoltaic cells, Sci. Adv. 3 (2017) 4204.

[130] D. Ghosh, M.Y. Ali, D.K. Chaudhary, S. Bhattacharyya, Dependence of halide composition on the stability of highly efficient all-inorganic cesium lead halide perovskite quantum dot solar cells, Sol. Energy Mater. Sol. Cells 185 (2018) 28–35.
[131] H. Xu, H. Yuan, J. Duan, Y. Zhao, Z. Jiao, Q. Tang, Lead-free $CH_3NH_3SnBr_{3-x}I_x$ perovskite quantum dots for mesoscopic solar cell applications, Electrochim. Acta 282 (2018) 807–812.
[132] J. Yuan, X. Ling, D. Yang, F. Li, S. Zhou, J. Shi, Y. Qian, J. Hu, Y. Sun, Y. Yang, X. Gao, S. Duhm, Q. Zhang, W. Ma, Band-aligned polymeric hole transport materials for extremely low energy loss α-$CsPbI_3$ perovskite nanocrystal solar cells, Joule 2 (2018) 2450–2463.
[133] X. Zhang, Z. Jin, J. Zhang, D. Bai, H. Bian, K. Wang, J. Sun, Q. Wang, S.F. Liu, All-ambient processed binary $CsPbBr_3$-$CsPb_2Br_5$ perovskites with synergistic enhancement for high-efficiency Cs-Pb-Br-based solar cells, ACS Appl. Mater. Interfaces 10 (2018) 7145–7154.
[134] K. Chen, Q. Zhong, W. Chen, B. Sang, Y. Wang, T. Yang, Y. Liu, Y. Zhang, H. Zhang, Short-chain ligand-passivated stable α-$CsPbI_3$ quantum dot for all-inorganic perovskite solar cells, Adv. Funct. Mater. 29 (2019) 1900991.
[135] X. Ling, S. Zhou, J. Yuan, J. Shi, Y. Qian, B.W. Larson, Q. Zhao, C. Qin, F. Li, G. Shi, C. Stewart, J. Hu, X. Zhang, J.M. Luther, S. Duhm, W. Ma, 14.1% $CsPbI_3$ perovskite quantum dot solar cells via cesium cation passivation, Adv. Energy Mater. 9 (2019) 1900721.
[136] F. Liu, C. Ding, Y. Zhang, T. Kamisaka, Q. Zhao, J.M. Luther, T. Toyoda, S. Hayase, T. Minemoto, K. Yoshino, B. Zhang, S. Dai, J. Jiang, S. Tao, Q. Shen, GeI_2 additive for high optoelectronic quality $CsPbI_3$ quantum dots and their application in photovoltaic devices, Chem. Mater. 31 (2019) 798–807.
[137] J. Shi, F. Li, J. Yuan, X. Ling, S. Zhou, Y. Qian, W. Ma, Efficient and stable $CsPbI_3$ perovskite quantum dots enabled by in situ ytterbium doping for photovoltaic applications, J. Mater. Chem. A 7 (2019) 20936–20944.
[138] M. Suri, A. Hazarika, B.W. Larson, Q. Zhao, M. Vallés-Pelarda, T.D. Siegler, M.K. Abney, A.J. Ferguson, B.A. Korgel, J.M. Luther, Enhanced open-circuit voltage of wide-bandgap perovskite photovoltaics by using alloyed $(FA_{1-x}Cs_x)Pb(I_{1-x}Br_x)_3$ quantum dots, ACS Energy Lett. 4 (2019) 1954–1960.
[139] Y. Wang, J. Tu, T. Li, C. Tao, X. Deng, Z. Li, Convenient preparation of $CsSnI_3$ quantum dots, excellent stability, and the highest performance of lead-free inorganic perovskite solar cells so far, J. Mater. Chem. A 7 (2019) 7683–7690.
[140] Z. Zolfaghari, E. Hassanabadi, D. Pitarch-Tena, S.J. Yoon, Z. Shariatinia, J. van de Lagemaat, J.M. Luther, I. Mora-Seró, Operation mechanism of perovskite quantum dot solar cells probed by impedance spectroscopy, ACS Energy Lett. 4 (2019) 251–258.
[141] K. Chen, W. Jin, Y. Zhang, T. Yang, P. Reiss, Q. Zhong, U. Bach, Q. Li, Y. Wang, H. Zhang, Q. Bao, Y. Liu, High efficiency mesoscopic solar cells using $CsPbI_3$ perovskite quantum dots enabled by chemical interface engineering, J. Am. Chem. Soc. 142 (2020) 3775–3783.
[142] C. Ding, F. Liu, Y. Zhang, D. Hirotani, X. Rin, S. Hayase, T. Minemoto, T. Masuda, R. Wang, Q. Shen, Photoexcited hot and cold electron and hole dynamics at $FAPbI_3$ perovskite quantum dots/metal oxide heterojunctions used for stable perovskite quantum dot solar cells, Nano Energy 67 (2020) 104267.
[143] C. Liu, Y. Yang, X. Liu, Y. Ding, Z. Arain, X. Li, Y. Li, Z. Zhou, S. Dai, M.K. Nazeeruddin, Quasi-quantum dot-induced stabilization of α-$CsPbI_3$ perovskite for high-efficiency solar cells, J. Mater. Chem. A 8 (2020) 10226–10232.
[144] S. Lim, J. Kim, J.Y. Park, J. Min, S. Yun, T. Park, Y. Kim, J. Choi, Suppressed degradation and enhanced performance of $CsPbI_3$ perovskite quantum dot solar cells via engineering of electron transport layers, ACS Appl. Mater. Interfaces 13 (2021) 6119–6129.
[145] S. Lim, G. Lee, S. Han, J. Kim, S. Yun, J. Lim, Y.-J. Pu, M.J. Ko, T. Park, J. Choi, Y. Kim, Monodisperse perovskite colloidal quantum dots enable high-efficiency photovoltaics, ACS Energy Lett. 6 (2021) 2229–2237.
[146] E. Yassitepe, Z. Yang, O. Voznyy, Y. Kim, G. Walters, J.A. Castañeda, P. Kanjanaboos, M. Yuan, X. Gong, F. Fan, J. Pan, S. Hoogland, R. Comin, O.M. Bakr, L.A. Padilha, A.F. Nogueira, E.H. Sargent, Amine-free synthesis of cesium lead halide perovskite quantum dots for efficient light-emitting diodes, Adv. Funct. Mater. 26 (2016) 8757–8763.
[147] Q. Fan, G.V. Biesold-McGee, J. Ma, Q. Xu, S. Pan, J. Peng, Z. Lin, Lead-free halide perovskite nanocrystals: crystal structures, synthesis, stabilities, and optical properties, Angew. Chem. Int. Ed. 59 (2020) 1030–1046.
[148] L.K. Ono, S. Liu, Y. Qi, Reducing detrimental defects for high-performance metal halide perovskite solar cells, Angew. Chem. Int. Ed. 59 (2020) 6676–6698.
[149] M. Grätzel, The rise of highly efficient and stable perovskite solar cells, Acc. Chem. Res. 50 (2017) 487–491.
[150] S. Masi, C. Echeverría-Arrondo, K.M.M. Salim, T.T. Ngo, P.F. Mendez, E. López-Fraguas, D.F. Macias-Pinilla, J. Planelles, J.I. Climente, I. Mora-Seró, Chemi-structural stabilization of formamidinium lead iodide perovskite by using embedded quantum dots, ACS Energy Lett. 5 (2020) 418–427.
[151] T.T. Ngo, S. Masi, P.F. Mendez, M. Kazes, D. Oron, I.M. Seró, PbS quantum dots as additives in methylammonium halide perovskite solar cells: the effect of quantum dot capping, Nanoscale Adv. 1 (2019) 4109–4118.
[152] J. Han, S. Luo, X. Yin, Y. Zhou, H. Nan, J. Li, X. Li, D. Oron, H. Shen, H. Lin, Hybrid PbS quantum-dot-in-perovskite for high-efficiency perovskite solar cell, Small 14 (2018) 1801016.
[153] J. Han, X. Yin, H. Nan, Y. Zhou, Z. Yao, J. Li, D. Oron, H. Lin, Enhancing the performance of perovskite solar cells by hybridizing SnS quantum dots with $CH_3NH_3PbI_3$, Small 13 (2017) 1700953.
[154] Y.Y. Zhao, Y.D. Wang, J.L. Duan, X.Y. Yang, Q.W. Tang, Divalent hard Lewis acid doped $CsPbBr_3$ films for 9.63%-efficiency and ultra-stable all-inorganic perovskite solar cells, J. Mater. Chem. A 7 (2019) 6877–6882.
[155] L. Yang, Y. Li, L. Wang, Y. Pei, Z. Wang, Y. Zhang, H. Lin, X. Li, Exfoliated fluorographene quantum dots as outstanding passivants for improved flexible perovskite solar cells, ACS Appl. Mater. Interfaces 12 (2020) 22992–23001.
[156] X. Gan, S. Yang, J. Zhang, G. Wang, P. He, H. Sun, H. Yuan, L. Yu, G. Ding, Y. Zhu, Graphite-N doped graphene quantum dots as semiconductor additive in perovskite solar cells, ACS Appl. Mater. Interfaces 11 (2019) 37796–37803.
[157] X. Fang, J. Ding, N. Yuan, P. Sun, M. Lv, G. Ding, C. Zhu, Graphene quantum dot incorporated perovskite films: passivating grain boundaries and facilitating electron extraction, Phys. Chem. Chem. Phys. 19 (2017) 6057–6063.
[158] Y. Wen, G. Zhu, Y. Shao, Improving the power conversion efficiency of perovskite solar cells by adding carbon quantum dots, J. Mater. Sci. 55 (2020) 2937–2946.
[159] H. Zou, D. Guo, B. He, J. Yu, K. Fan, Enhanced photocurrent density of HTM-free perovskite solar cells by carbon quantum dots, Appl. Surf. Sci. 430 (2018) 625–631.
[160] Ç. Kırbıyık, A. Toprak, C. Başlak, M. Kuş, M. Ersöz, Nitrogen-doped CQDs to enhance the power conversion efficiency of perovskite solar cells via surface passivation, J. Alloy. Compd. 832 (2020) 154897.
[161] Y. Ma, H. Zhang, Y. Zhang, R. Hu, M. Jiang, R. Zhang, H. Lv, J. Tian, L. Chu, J. Zhang, Q. Xue, H.-L. Yip, R. Xia, Xa Li, W. Huang, Enhancing the performance of inverted perovskite solar cells via grain boundary passivation with carbon quantum dots, ACS Appl. Mater. Interfaces 11 (2019) 3044–3052.
[162] Q. Guo, F. Yuan, B. Zhang, S. Zhou, J. Zhang, Y. Bai, L. Fan, T. Hayat, A. Alsaedi, Za Tan, Passivation of the grain boundaries of $CH_3NH_3PbI_3$ using carbon quantum dots for highly efficient perovskite solar cells with excellent environmental stability, Nanoscale 11 (2019) 115–124.
[163] G. Seo, J. Seo, S. Ryu, W. Yin, T.K. Ahn, S.I. Seok, Enhancing the performance of sensitized solar cells with PbS/$CH_3NH_3PbI_3$ core/shell quantum dots, J. Phys. Chem. Lett. 5 (2014) 2015–2020.
[164] L. Hu, Z. Zhang, R.J. Patterson, S.B. Shivarudraiah, Z. Zhou, M. Ng, S. Huang, J.E. Halpert, PbSe quantum dot passivated via mixed halide perovskite nanocrystals for solar cells with over 9% efficiency, Sol. RRL 2 (2018) 1800234.
[165] L. Etgar, P. Gao, P. Qin, M. Graetzel, M.K. Nazeeruddin, A hybrid lead iodide perovskite and lead sulfide QD heterojunction solar cell to obtain a panchromatic response, J. Mater. Chem. A 2 (2014) 11586–11590.
[166] X. Zhang, J. Zhang, D. Phuyal, J. Du, L. Tian, V.A. Öberg, M.B. Johansson, U.B. Cappel, O. Karis, J. Liu, H. Rensmo, G. Boschloo, E.M.J. Johansson, Inorganic $CsPbI_3$ perovskite coating on PbS quantum dot for highly efficient and stable infrared light converting solar cells, Adv. Energy Mater. 8 (2018) 1702049.
[167] Y. Yang, W. Wang, Effects of incorporating PbS quantum dots in perovskite solar cells based on $CH_3NH_3PbI_3$, J. Power Sources 293 (2015) 577–584.
[168] L. Pan, C. Liu, H. Zhu, M. Wan, Y. Li, Y. Mai, Fine modification of reactively sputtered NiO_x hole transport layer for application in all-inorganic $CsPbI_2Br$ perovskite solar cells, Sol. Energy 196 (2020) 521–529.
[169] N. Arora, M.I. Dar, A. Hinderhofer, N. Pellet, F. Schreiber, S.M. Zakeeruddin, M. Grätzel, Perovskite solar cells with CuSCN hole extraction layers yield stabilized efficiencies greater than 20%, Science 358 (2017) 768–771.
[170] J.A. Christians, R.C. Fung, P.V. Kamat, An inorganic hole conductor for organo-lead halide perovskite solar cells. Improved hole conductivity with copper iodide, J. Am. Chem. Soc. 136 (2014) 758–764.
[171] Y. Li, J. Zhu, Y. Huang, J. Wei, F. Liu, Z. Shao, L. Hu, S. Chen, S. Yang, J. Tang, J. Yao, S. Dai, Efficient inorganic solid solar cells composed of perovskite and PbS quantum dots, Nanoscale 7 (2015) 9902–9907.
[172] F. Li, J. Wei, G. Liao, C. Guo, Y. Huang, Q. Zhang, X. Jin, S. Jiang, Q. Tang, Q. Li, Quaternary quantum dots with gradient valence band for all-inorganic perovskite solar cells, J. Colloid Interface Sci. 549 (2019) 33–41.
[173] Y. Liu, X. Zhao, Z. Yang, Q. Li, W. Wei, B. Hu, W. Chen, Understanding the defect properties of Quasi-2D halide perovskites for photovoltaic applications, J. Phys. Chem. Lett. 11 (2020) 3521–3528.
[174] Y. Liu, Q. Chen, A. Mei, B. Hu, Z. Yang, W. Chen, Bandgap aligned $Cu_{12}Sb_4S_{13}$ quantum dots as efficient inorganic hole transport materials in planar perovskite solar cells with enhanced stability, Sustain. Energy Fuels 3 (2019) 831–840.
[175] Z.-J. Zhou, Y.-Q. Deng, P.-P. Zhang, D.-X. Kou, W.-H. Zhou, Y.-N. Meng, S.-J. Yuan, S.-X. Wu, Cu_2ZnSnS_4 quantum dots as hole transport material for enhanced charge extraction and stability in all-inorganic $CsPbBr_3$ perovskite solar cells, Sol. RRL 3 (2019) 1800354.
[176] J.L. Duan, D.W. Dou, Y.Y. Zhao, Y.D. Wang, X.Y. Yang, H.W. Yuan, B.L. He, Q.W. Tang, Spray-assisted deposition of $CsPbBr_3$ films in ambient air for large-area inorganic perovskite solar cells, Mater. Today Energy 10 (2018) 146–152.
[177] Y. Zhang, Z. Zhang, Y. Liu, Y. Liu, H. Gao, Y. Mao, An inorganic hole-transport material of $CuInSe_2$ for stable and efficient perovskite solar cells, Org. Electron. 67 (2019) 168–174.
[178] C. Jiang, J. Yao, P. Huang, R. Tang, X. Wang, X. Lei, H. Zeng, S. Chang, H. Zhong, H. Yao, C. Zhu, T. Chen, Perovskite quantum dots exhibiting strong hole extraction capability for efficient inorganic thin film solar cells, Cell Rep. Phys. Sci. 1 (2020) 100001.
[179] W. Li, N. Cheng, Y. Cao, Z. Zhao, Z. Xiao, W. Zi, Z. Sun, Boost the performance of inverted perovskite solar cells with PEDOT:PSS/graphene quantum dots composite hole transporting layer, Org. Electron. 78 (2020) 105575.
[180] Z. Jin, M. Yuan, H. Li, H. Yang, Q. Zhou, H. Liu, X. Lan, M. Liu, J. Wang, E.H. Sargent, Y. Li, Graphdiyne: an efficient hole transporter for stable high-performance colloidal quantum dot solar cells, Adv. Funct. Mater. 26 (2016) 5284–5289.
[181] C. He, F. Zhang, X. Zhao, C. Lin, M. Ye, Interface engineering of BCP buffer layers in planar heterojunction perovskite solar cells with NiO_x hole transporting layers, Front. Phys. 6 (2018) 99.

[182] Z. Zhu, J. Ma, Z. Wang, C. Mu, Z. Fan, L. Du, Y. Bai, L. Fan, H. Yan, D.L. Phillips, S. Yang, Efficiency enhancement of perovskite solar cells through fast electron extraction: the role of graphene quantum dots, J. Am. Chem. Soc. 136 (2014) 3760–3763.
[183] W. Yang, R. Su, D. Luo, Q. Hu, F. Zhang, Z. Xu, Z. Wang, J. Tang, Z. Lv, X. Yang, Y. Tu, W. Zhang, H. Zhong, Q. Gong, T.P. Russell, R. Zhu, Surface modification induced by perovskite quantum dots for triple-cation perovskite solar cells, Nano Energy 67 (2020) 104189.
[184] M. Cha, P. Da, J. Wang, W. Wang, Z. Chen, F. Xiu, G. Zheng, Z.-S. Wang, Enhancing perovskite solar cell performance by interface engineering using $CH_3NH_3PbBr_{0.9}I_{2.1}$ quantum dots, J. Am. Chem. Soc. 138 (2016) 8581–8587.
[185] S. Zhou, R. Tang, L. Yin, Slow-photon-effect-induced photoelectrical-conversion efficiency enhancement for carbon-quantum-dot-sensitized inorganic $CsPbBr_3$ inverse opal perovskite solar cells, Adv. Mater. 29 (2017) 1703682.
[186] H. Bian, D. Bai, Z. Jin, K. Wang, L. Liang, H. Wang, J. Zhang, Q. Wang, S. Liu, Graded bandgap $CsPbI_{2+x}Br_{1-x}$ perovskite solar cells with a stabilized efficiency of 14.4%, Joule 2 (2018) 1500–1510.
[187] J. Duan, T. Hu, Y. Zhao, B. He, Q. Tang, Carbon-electrode-tailored all-inorganic perovskite solar cells to harvest solar and water-vapor energy, Angew. Chem. Int. Ed. 57 (2018) 5746–5749.
[188] J.-W. Xiao, S. Ma, S. Yu, C. Zhou, P. Liu, Y. Chen, H. Zhou, Y. Li, Q. Chen, Ligand engineering on CdTe quantum dots in perovskite solar cells for suppressed hysteresis, Nano Energy 46 (2018) 45–53.
[189] J. Zhang, Z. Jin, L. Liang, H. Wang, D. Bai, H. Bian, K. Wang, Q. Wang, N. Yuan, J. Ding, Iodine-optimized interface for inorganic $CsPbI_2Br$ perovskite solar cell to attain high stabilized efficiency exceeding 14%, Adv. Sci. 5 (2018) 1801123.
[190] D. Shen, W. Zhang, F. Xie, Y. Li, A. Abate, M. Wei, Graphene quantum dots decorated TiO_2 mesoporous film as an efficient electron transport layer for high-performance perovskite solar cells, J. Power Sources 402 (2018) 320–326.
[191] H. Xia, Z. Ma, Z. Xiao, W. Zhou, H. Zhang, C. Du, J. Zhuang, X. Cheng, X. Liu, Y. Huang, Interfacial modification using ultrasonic atomized graphene quantum dots for efficient perovskite solar cells, Org. Electron. 75 (2019) 105415.
[192] H. Chen, Q. Luo, T. Liu, M. Tai, J. Lin, V. Murugadoss, H. Lin, J. Wang, Z. Guo, N. Wang, Boosting multiple interfaces by Co-doped graphene quantum dots for high efficiency and durability perovskite solar cells, ACS Appl. Mater. Interfaces 12 (2020) 13941–13949.
[193] Y.A. Li, J.L. Duan, Y.Y. Zhao, Q.W. Tang, All-inorganic bifacial $CsPbBr_3$ perovskite solar cells with a 98.5%-bifacial factor, Chem. Commun. 54 (2018) 8237–8240.
[194] G. Liao, J. Duan, Y. Zhao, Q. Tang, Toward fast charge extraction in all-inorganic $CsPbBr_3$ perovskite solar cells by setting intermediate energy levels, Sol. Energy 171 (2018) 279–285.
[195] H.W. Yuan, Y.Y. Zhao, J.L. Duan, B.L. He, Z.B. Jiao, Q.W. Tang, Enhanced charge extraction by setting intermediate energy levels in all-inorganic $CsPbBr_3$ perovskite solar cells, Electrochim. Acta 279 (2018) 84–90.
[196] P. Liu, Y. Sun, S. Wang, H. Zhang, Y. Gong, F. Li, Y. Shi, Y. Du, X. Li, S.-s. Guo, Q. Tai, C. Wang, X.-Z. Zhao, Two dimensional graphitic carbon nitride quantum dots modified perovskite solar cells and photodetectors with high performances, J. Power Sources 451 (2020) 227825.
[197] S.M. Ali, S.M. Ramay, M.H. Aziz, N. ur-Rehman, M.S. AlGarawi, S.S. AlGhamd, A. Mahmood, T.S. Alkhuraiji, S. Atiq, Efficiency enhancement of perovskite solar cells by incorporation of CdS quantum dot through fast electron injection, Org. Electron. 62 (2018) 21–25.
[198] J. Lei, F. Gao, H. Wang, J. Li, J. Jiang, X. Wu, R. Gao, Z. Yang, S.F. Liu, Efficient planar $CsPbBr_3$ perovskite solar cells by dual-source vacuum evaporation, Sol. Energy Mater. Sol. Cells 187 (2018) 1–8.
[199] F. Gao, Q. Zheng, Y. Zhang, Stability improvement of perovskite solar cells for application of $CuInS_2$ quantum dot-modified TiO_2 nanoarrays, ACS Omega 4 (2019) 3432–3438.
[200] S. Zou, F. Li, Efficient all-inorganic $CsPbBr_3$ perovskite solar cells by using CdS/CdSe/CdS quantum dots as intermediate layers, J. Nanomater. 2020 (2020) 1–11.
[201] T. Wu, C. Zhen, J. Wu, C. Jia, M. Haider, L. Wang, G. Liu, H.-M. Cheng, Chlorine capped SnO_2 quantum-dots modified TiO_2 electron selective layer to enhance the performance of planar perovskite solar cells, Sci. Bull. 64 (2019) 547–552.
[202] L.-C. Chen, C.-H. Tien, Z.-L. Tseng, J.-H. Ruan, Enhanced efficiency of $MAPbI_3$ perovskite solar cells with $FAPbX_3$ perovskite quantum dots, Nanomaterials 9 (2019) 121.
[203] X. Zheng, J. Troughton, N. Gasparini, Y. Lin, M. Wei, Y. Hou, J. Liu, K. Song, Z. Chen, C. Yang, B. Turedi, A.Y. Alsalloum, J. Pan, J. Chen, A.A. Zhumekenov, T.D. Anthopoulos, Y. Han, D. Baran, O.F. Mohammed, E.H. Sargent, O.M. Bakr, Quantum Dots Supply Bulk- and Surface-Passivation Agents for Efficient and Stable Perovskite Solar Cells, Joule 3 (2019) 1963–1976.
[204] Y. Yao, P. Hang, P. Wang, L. Xu, C. Cui, J. Xie, K. Xiao, G. Li, P. Lin, S. Liu, D. Xie, S. Che, D. Yang, X. Yu, $CsPbBr_3$ quantum dots assisted crystallization of solution-processed perovskite films with preferential orientation for high performance perovskite solar cells, Nanotechnology 31 (2019) 085401.
[205] S. Akin, Y. Altintas, E. Mutlugun, S. Sonmezoglu, Cesium lead based inorganic perovskite quantum-dots as interfacial layer for highly stable perovskite solar cells with exceeding 21% efficiency, Nano Energy 60 (2019) 557–566.
[206] H. Xu, J. Duan, Y. Zhao, Z. Jiao, B. He, Q. Tang, 9.13%-Efficiency and stable inorganic $CsPbBr_3$ solar cells. Lead-free $CsSnBr_{3-x}I_x$ quantum dots promote charge extraction, J. Power Sources 399 (2018) 76–82.
[207] J. Ding, J.L. Duan, C.Y. Guo, Q.W. Tang, Toward charge extraction in all-inorganic perovskite solar cells by interfacial engineering, J. Mater. Chem. A 6 (2018) 21999–22004.
[208] C. Chen, F. Li, L. Zhu, Z. Shen, Y. Weng, Q. Lou, F. Tan, G. Yue, Q. Huang, M. Wang, Efficient and stable perovskite solar cells thanks to dual functions of oleyl amine-coated $PbSO_4(PbO)_4$ quantum dots: defect passivation and moisture/oxygen blocking, Nano Energy 68 (2020) 104313.
[209] X. Zhu, B. Cheng, X. Li, J. Zhang, L. Zhang, Enhanced efficiency of perovskite solar cells by PbS quantum dot modification, Appl. Surf. Sci. 487 (2019) 32–40.
[210] S. Zhou, R. Tang, H. Li, L. Fu, B. Li, L. Yin, Fluorescence resonance energy transfer effect enhanced high performance of Si quantum Dots/$CsPbBr_3$ inverse opal heterostructure perovskite solar cells, J. Power Sources 439 (2019) 227065.
[211] L.-C. Chen, C.-H. Tien, K.-L. Lee, Y.-T. Kao, Efficiency improvement of $MAPbI_3$ perovskite solar cells based on a $CsPbBr_3$ quantum dot/Au nanoparticle composite plasmonic light-harvesting layer, Energies 13 (2020) 1471.
[212] Z. Zhao, F. Gu, H. Rao, S. Ye, Z. Liu, Z. Bian, C. Huang, Metal halide perovskite materials for solar cells with long-term stability, Adv. Energy Mater. 9 (2019) 1802671.
[213] M.M. Tavakoli, H.T. Dastjerdi, D. Prochowicz, P. Yadav, R. Tavakoli, M. Saliba, Z. Fan, Highly efficient and stable inverted perovskite solar cells using down-shifting quantum dots as a light management layer and moisture-assisted film growth, J. Mater. Chem. A 7 (2019) 14753–14760.
[214] A.A. Maxim, S.N. Sadyk, D. Aidarkhanov, C. Surya, A. Ng, Y.-H. Hwang, T.S. Atabaev, A.N. Jumabekov, PMMA thin film with embedded carbon quantum dots for post-fabrication improvement of light harvesting in perovskite solar cells, Nanomaterials 10 (2020) 291.
[215] B. Wang, B. Li, T. Shen, M. Li, J. Tian, ZnSe quantum dots downshifting layer for perovskite solar cells, J. Energy Chem. 27 (2018) 736–741.
[216] M. He, X. Pang, X. Liu, B. Jiang, Y. He, H. Snaith, Z. Lin, Monodisperse dual-functional upconversion nanoparticles enabled near-infrared organolead halide perovskite solar cells, Angew. Chem. Int. Ed. 55 (2016) 4280–4284.
[217] Q. Wang, X. Zhang, Z. Jin, J. Zhang, Z. Gao, Y. Li, S.F. Liu, Energy-down-shift $CsPbCl_3$:Mn quantum dots for boosting the efficiency and stability of perovskite solar cells, ACS Energy Lett. 2 (2017) 1479–1486.
[218] Z. Hosseini, T. Ghanbari, Designing an efficient graphene quantum dot-filled luminescent down shifting layer to improve the stability and efficiency of perovskite solar cells by simple optical modeling, RSC Adv. 8 (2018) 31502–31509.
[219] H. Bian, Q. Wang, S. Yang, C. Yan, H. Wang, L. Liang, Z. Jin, G. Wang, S. Liu, Nitrogen-doped graphene quantum dots for 80% photoluminescence quantum yield for inorganic γ-$CsPbI_3$ perovskite solar cells with efficiency beyond 16%, J. Mater. Chem. A 7 (2019) 5740–5747.
[220] Y. He, Y.J. Yoon, Y.W. Harn, G.V. Biesold-McGee, S. Liang, C.H. Lin, V.V. Tsukruk, N. Thadhani, Z. Kang, Z. Lin, Unconventional route to dual-shelled organolead halide perovskite nanocrystals with controlled dimensions, surface chemistry, and stabilities, Sci. Adv. 5 (2019) 4424.
[221] F. Zhang, S. Huang, P. Wang, X. Chen, S. Zhao, Y. Dong, H. Zhong, Colloidal Synthesis of Air-Stable $CH_3NH_3PbI_3$ Quantum Dots by Gaining Chemical Insight into the Solvent Effects, Chem. Mater. 29 (2017) 3793–3799.
[222] D. Zhou, D. Liu, G. Pan, X. Chen, D. Li, W. Xu, X. Bai, H. Song, Cerium and ytterbium codoped halide perovskite quantum dots: a novel and efficient downconverter for improving the performance of silicon solar cells, Adv. Mater. 29 (2017) 1704149.
[223] J. Zhu, X. Yang, Y. Zhu, Y. Wang, J. Cai, J. Shen, L. Sun, C. Li, Room-temperature synthesis of Mn-doped cesium lead halide quantum dots with high Mn substitution ratio, J. Phys. Chem. Lett. 8 (2017) 4167–4171.
[224] P.K. Santra, P.V. Kamat, Mn-doped quantum dot sensitized solar cells: a strategy to boost efficiency over 5%, J. Am. Chem. Soc. 134 (2012) 2508–2511.
[225] M. Tang, B. He, D. Dou, Y. Liu, J. Duan, Y. Zhao, H. Chen, Q. Tang, Ternary $BiVO_4$/NiS/Au nanocomposites with efficient charge separations for enhanced visible light photocatalytic performance, Chem. Eng. J. 375 (2019) 122093.
[226] J. Duan, Y. Zhao, X. Yang, Y. Wang, B. He, Q. Tang, Lanthanide ions doped $CsPbBr_3$ halides for HTM-free 10.14%-efficiency inorganic perovskite solar cell with an ultrahigh open-circuit voltage of 1.594 V, Adv. Energy Mater. 8 (2018) 1802346.
[227] Y. Liu, W. Chen, J. Zhong, D. Chen, Upconversion luminescence in Yb/Ln (Ln = Er, Tm) doped oxyhalide glasses containing $CsPbBr_3$ perovskite nanocrystals, J. Eur. Ceram. Soc. 39 (2019) 4275–4282.
[228] P. Liu, X. Yang, Y. Chen, H. Xiang, W. Wang, R. Ran, W. Zhou, Z. Shao, Promoting the efficiency and stability of $CsPbIBr_2$-based all-inorganic perovskite solar cells through a functional Cu^{2+} doping strategy, ACS Appl. Mater. Interfaces 12 (2020) 23984–23994.
[229] H. Sun, L. Yu, H. Yuan, J. Zhang, X. Gan, Z. Hu, Y. Zhu, $CoCl_2$ as film morphology controller for efficient planar $CsPbIBr_2$ perovskite solar cells, Electrochim. Acta 349 (2020) 136162.
[230] W. Xiang, Z. Wang, D.J. Kubicki, W. Tress, J. Luo, D. Prochowicz, S. Akin, L. Emsley, J. Zhou, G. Dietler, Europium-doped $CsPbI_2Br$ for stable and highly efficient inorganic perovskite solar cells, Joule 3 (2019) 205–214.
[231] A. Meng, X. Yuan, T. Shen, Z. Li, Q. Jiang, H. Xue, Y. Lin, J. Zhao, One-step synthesis of flower-like Bi_2O_3/Bi_2Se_3 nanoarchitectures and $NiCoSe_2/Ni_{0.85}Se$ nanoparticles with appealing rate capability for the construction of high-energy and long-cycle-life asymmetric aqueous batteries, J. Mater. Chem. A 7 (2019) 17613–17625.
[232] Y. Guo, F. Zhao, Z. Li, J. Tao, D. Zheng, J. Jiang, Growth control and defect passivation toward efficient and low-temperature processed carbon based $CsPbIBr_2$ solar cell, Org. Electron. 83 (2020) 105731.
[233] M. Hu, M. Chen, P. Guo, H. Zhou, J. Deng, Y. Yao, Y. Jiang, J. Gong, Z. Dai, Y. Zhou, Sub-1.4 eV bandgap inorganic perovskite solar cells with long-term stability, Nat. Commun. 11 (2020) 1–10.

[234] S. Shao, J. Liu, G. Portale, H.H. Fang, G.R. Blake, G.H. ten Brink, L.J.A. Koster, M.A. Loi, Highly reproducible Sn-based hybrid perovskite solar cells with 9% efficiency, Adv. Energy Mater. 8 (2018) 1702019.
[235] W.S. Subhani, K. Wang, M. Du, S.F. Liu, Goldschmidt-rule-deviated perovskite $CsPbIBr_2$ by barium substitution for efficient solar cells, Nano Energy 61 (2019) 165–172.
[236] Y. Han, H. Zhao, C. Duan, S. Yang, Z. Yang, Z. Liu, S. Liu, Controlled n-doping in air-stable $CsPbI_2Br$ perovskite solar cells with a record efficiency of 16.79%, Adv. Funct. Mater. 30 (2020) 1909972.
[237] C.F.J. Lau, M. Zhang, X. Deng, J. Zheng, J. Bing, Q. Ma, J. Kim, L. Hu, M.A. Green, S. Huang, Strontium-doped low-temperature-processed $CsPbI_2Br$ perovskite solar cells, ACS Energy Lett. 2 (2017) 2319–2325.
[238] G. Shao, S. Liu, L. Ding, Z. Zhang, W. Xiang, X. Liang, $K_xCs_{1-x}PbBr_3$ NCs glasses possessing super optical properties and stability for white light emitting diodes, Chem. Eng. J. 375 (2019) 122031.
[239] X. Tan, X. Liu, Z. Liu, B. Sun, J. Li, S. Xi, T. Shi, Z. Tang, G. Liao, Enhancing the optical, morphological and electronic properties of the solution-processed $CsPbIBr_2$ films by Li doping for efficient carbon-based perovskite solar cells, Appl. Surf. Sci. (2019) 143990.
[240] J.K. Nam, S.U. Chai, W. Cha, Y.J. Choi, W. Kim, M.S. Jung, J. Kwon, D. Kim, J.H. Park, Potassium incorporation for enhanced performance and stability of fully inorganic cesium lead halide perovskite solar cells, Nano Lett. 17 (2017) 2028–2033.
[241] Y. Hu, F. Bai, X. Liu, Q. Ji, X. Miao, T. Qiu, S. Zhang, Bismuth incorporation stabilized α-$CsPbI_3$ for fully inorganic perovskite solar cells, ACS Energy Lett. 2 (2017) 2219–2227.
[242] Q. Chen, L. Chen, F. Ye, T. Zhao, F. Tang, A. Rajagopal, Z. Jiang, S. Jiang, A.K.-Y. Jen, Y. Xie, Ag-incorporated organic-inorganic perovskite films and planar heterojunction solar cells, Nano Lett. 17 (2017) 3231–3237.
[243] G. Longo, S. Mahesh, L.R.V. Buizza, A.D. Wright, A.J. Ramadan, M. Abdi-Jalebi, P.K. Nayak, L.M. Herz, H.J. Snaith, Understanding the performance-limiting factors of $Cs_2AgBiBr_6$ double-perovskite solar cells, ACS Energy Lett. 5 (2020) 2200–2207.
[244] P. Abellan, B.L. Mehdi, L.R. Parent, M. Gu, C. Park, W. Xu, Y. Zhang, I. Arslan, J.-G. Zhang, C.-M. Wang, J.E. Evans, N.D. Browning, Probing the degradation mechanisms in electrolyte solutions for Li-ion batteries by in situ transmission electron microscopy, Nano Lett. 14 (2014) 1293–1299.
[245] S. Ramdon, B. Bhushan, S.C. Nagpure, In situ electrochemical studies of lithium-ion battery cathodes using atomic force microscopy, J. Power Sources 249 (2014) 373–384.
[246] C.R. Becker, K.E. Strawhecker, Q.P. McAllister, C.A. Lundgren, In situ atomic force microscopy of lithiation and delithiation of silicon nanostructures for lithium ion batteries, ACS Nano 7 (2013) 9173–9182.
[247] J. Qi, H. Xiong, G. Wang, H. Xie, W. Jia, Q. Zhang, Y. Li, H. Wang, High-performance solar cells with induced crystallization of perovskite by an evenly distributed CdSe quantum dots seed-mediated underlayer, J. Power Sources 376 (2018) 46–54.
[248] C.-X. Qian, Z.-Y. Deng, K. Yang, J. Feng, M.-Z. Wang, Z. Yang, S. Liu, H.-J. Feng, Interface engineering of $CsPbBr_3/TiO_2$ heterostructure with enhanced optoelectronic properties for all-inorganic perovskite solar cells, Appl. Phys. Lett. 112 (2018) 093901.
[249] X. Zheng, Y. Hou, C. Bao, J. Yin, F. Yuan, Z. Huang, K. Song, J. Liu, J. Troughton, N. Gasparini, Managing grains and interfaces via ligand anchoring enables 22.3%-efficiency inverted perovskite solar cells, Nat. Energy 5 (2020) 131–140.
[250] D. Jia, J. Chen, M. Yu, J. Liu, E.M.J. Johansson, A. Hagfeldt, X. Zhang, Dual passivation of $CsPbI_3$ perovskite nanocrystals with amino acid ligands for efficient quantum dot solar cells, Small 16 (2020) 2001772.
[251] W. Yang, Y. Tang, Q. Zhang, L. Wang, B. Song, C. Wong, Reducing Pb concentration in α-$CsPbI_3$ based perovskite solar cell materials via alkaline-earth metal doping: a DFT computational study, Ceram. Int. 43 (2017) 13101–13112.
[252] X.-D. Wang, Y.-H. Huang, J.-F. Liao, Y. Jiang, L. Zhou, X.-Y. Zhang, H.-Y. Chen, D.-B. Kuang, In situ construction of a Cs_2SnI_6 perovskite nanocrystal/SnS_2 nanosheet heterojunction with boosted interfacial charge transfer, J. Am. Chem. Soc. 141 (2019) 13434–13441.

Dr. Meidan Ye received her Ph.D. in College of Chemistry and Chemical Engineering at Xiamen University in 2014. She then joined Research Institute for Soft Matter and Biomimetics, Department of Physics, College of Physical Science and Technology at Xiamen University as an associate Professor in 2014. Her research interests focus on nanostructured inorganic materials for flexible devices, such as perovskite solar cells, electrochemical energy storage devices and wearable sensors.

Gill M. Biesold is a Ph.D. student in the Materials Science and Engineering department at Georgia Institute of Technology. He received his B.S. in Materials Science and Engineering from Clemson University in 2017. His current research is focused on the synthesis of colloidal semiconductor nanocrystals and their optoelectronic properties.

Dr. Meng Zhang is a research scientist fellow in Dr. Zhiqun Lin's group in the School of Materials Science and Engineering at Georgia Institute of Technology. She received her Ph.D. degree in Engineering Thermophysics from Zhejiang University, China in 2016. Her research interests are centered on solar energy conversion and storage, including perovskite solar cells, CO_2 conversion and utilization, and advanced energy materials.

Weiguo Wang is a graduate student in Department of Physics, College of Physical Science and Technology, Xiamen University, China. He received his B.S. from Fujian Agriculture and Forestry University, China in 2019. His research focuses on perovskite solar cells.

Tian Bai is a graduate student in Department of Physics, College of Physical Science and Technology, Xiamen University, China. He received his B.S. from Shaanxi University of Science & Technology, China in 2018. His research focuses on 2D MXene-based devices.

Dr. Zhiqun Lin is a Professor in the School of Materials Science and Engineering at the Georgia Institute of Technology. His research interests include solar cells, batteries, electrocatalysis, photocatalysis, organic-inorganic nanocomposites, multifunctional nanocrystals, and Janus nanostructures, conjugated polymers, block copolymers, hierarchical structure formation and assembly, and surface and interfacial properties.